

# **Modelling the Effect of Bubble Dynamics on Motion and Mass transfer**

## **Dissertation**

zur Erlangung des akademischen Grades

**Doktoringenieur  
(Dr.-Ing.)**

von **M.Sc. Marcelo Muniz**

geboren am 26.01.1990, in Lages – SC (Brasilien)

genehmigt durch die Fakultät für Verfahrens- und Systemtechnik  
der Otto-von-Guericke-Universität Magdeburg

Promotionskommission: Prof. Dr.-Ing. Ulrich Krause (Vorsitz)  
Prof. Dr.-Ing. Martin Sommerfeld (Gutachter)  
Prof. Dr.-Ing. Matthias Kraume (Gutachter)  
Prof. Dr.-Ing. Ulrich Niekens (Gutachter)

eingereicht am: 02.05.2019

Promotionskolloquium am: 22.07.2019



## **Schriftliche Erklärung**

Ich erkläre hiermit, dass ich die vorliegende Arbeit ohne unzulässige Hilfe Dritter und ohne Benutzung anderer als der angegebenen Hilfsmittel angefertigt habe. Die aus fremden Quellen direkt oder indirekt übernommenen Gedanken sind als solche kenntlich gemacht.

Insbesondere habe ich nicht die Hilfe einer kommerziellen Promotionsberatung in Anspruch genommen. Dritte haben von mir weder unmittelbar noch mittelbar geldwerte Leistungen für Arbeiten erhalten, die im Zusammenhang mit dem Inhalt der vorgelegten Dissertation stehen.

Die Arbeit wurde bisher weder im Inland noch im Ausland in gleicher oder ähnlicher Form als Dissertation eingereicht und ist als Ganzes auch noch nicht veröffentlicht.

## **Declaration**

I hereby declare that I prepared the work submitted without inadmissible assistance and without the use of any aids other than those indicated. Facts or ideas taken from other sources, either directly or indirectly have been marked as such.

In particular, I did not use the services of a commercial graduation consultation. Further I have not made payments to third parties either directly or indirectly for any work connected with the contents of the submitted dissertation.

The work has not been submitted as a dissertation either in Germany or abroad in the same or similar form and has also not been published as a whole.

07.11.2019, Halle (Saale)

*Marcelo Muniz*



# Preface

This document represents the work developed during my PhD from May 2015 until July 2019 at the Workgroup of Multiphase Flows (MPS) at the Faculty of Process- and Systems-Engineering (IVT) of the Otto-von-Guericke-Universität Magdeburg. The main objective of the present work is to highlight the importance of modelling bubble dynamics on motion and mass transfer. Bubble dynamics plays an important role on the elementary processes in bubble columns, but is still often neglected. Thus, a CFD model designed for predicting the flow and mass transfer within the frame of LES-Euler/Lagrange point-particle approach is proposed and was implemented in the platform OpenFOAM (v4.1). The preference for this open-source software is that a community has been growing worldwide and supports the continuous development of research in this area, differently than commercial codes consistent of “black-boxes”, where the user cannot be really assured what has been calculating behind.

I gratefully acknowledge the financial support through the scholarship from CNPq (National Council for Scientific and Technological Development – Brazil), DAAD (German Academic Exchange Service). Moreover, I would like to thank the DFG SPP-1740 (Priority Program 1740 – Reactive Bubbly Flows), despite not being official member from the program, it contributed in the development of this work.



# Zusammenfassung

Die numerische Strömungsmechanik wird in technischen Anwendungen als potentes Werkzeug zur Vorhersage von Strömungen, Umsetzungsraten und Effizienz in vielen Geräten eingesetzt. Euler/Lagrange ist einer der verfügbaren Ansätze zur Darstellung von Mehrphasensystemen, beispielsweise Blasensäulen. Bei diesem Ansatz werden die flüssige Phase als Kontinuum und die Blasen als diskrete "Punktpartikel" behandelt. Um die Blasenbewegung so gut wie möglich vorherzusagen zu können, müssen bei der Berechnung alle relevanten wirkenden Kräfte berücksichtigt werden, und zwar Schwerkraft/Auftrieb, Widerstand, virtuelle Masse, transversaler Auftrieb, Flüssigkeitsträgheit, Wand- und Basset-Kraft (Geschichte-Term). Im Gegensatz zu festen Partikeln zeigen Blasen während ihres Aufstiegs eine kontinuierliche Formschwingung, gekoppelt mit einer Taumelbewegung. Ungeachtet der Verwendung der Punktpartikel-Näherung wurde in dieser Arbeit die Blasendynamik in das Modell einbezogen, indem zunächst eine momentane Blasenexzentrizität angenommen und in den Kräften berücksichtigt wurde. Anschließend wird die Taumelbewegung vom Modell induziert, indem die Richtung der Blasenbewegung von einem geraden Pfad aus geändert wird. Um Rechenzeit zu sparen, wird die lokale Berechnung der Blasenexzentrizität und des Bewegungswinkels stochastisch durchgeführt, jedoch zeitlich korreliert, wobei experimentelle Beobachtungen hinsichtlich der Schwingungsfrequenzen und -amplituden verwendet werden. Dieser Prozess stellt effizient die Blasendynamik durch eine Ein-Schritt-Langevin-Gleichung dar, sodass auch die Einfachheit des Modells erhalten bleibt. Darüber hinaus wird eine Bewertung des Kräftewettbewerbs in einer Laborblasensäule in Bezug auf den Durchmesser der Blasenäquivalente und die räumlichen Koordinaten, und zwar radiale und axiale Positionen, durchgeführt. Schließlich zeigte die Modellierung von Form- und Pfadschwingungen eine größere Wichtigkeit der virtuellen Massen- und Basset-Kräfte als bei dem Basismodell. Es wurde auch festgestellt, dass der Geschichte-Term als Widerstand gegen die Bewegungsänderung wirkt, da die Schwankungen der Blasengeschwindigkeit schwächer werden. Nichtsdestotrotz verstärkt diese Kraft die gesamte Dispersion der Blasen. Schließlich wird die Formulierung für Fälle mit Stoffübertragung erweitert, bei denen eine dynamische Sherwood-Zahl mit dem Blasendynamikmodell kombiniert wird. Zusammenfassend ist das hier implementierte CFD-Modell (Plattform OpenFOAM) dafür geeignet, Strömungen und Stoffübertragung in Blasensäulen vorherzusagen und die Blasendynamik im Rahmen des Euler/Lagrange Ansatzes zu berücksichtigen.





# Abstract

Computational Fluid Dynamics have been widely used in engineering applications as a potential tool for prediction of flows, conversion rates and efficiency in many apparatuses. The Euler/Lagrange is one of the available approaches for representing multiphase systems, for example bubble columns. With this approach the liquid phase is treated as a continuum and the bubbles as discrete “point-particles”. In order to predict the bubble motion as well as possible, all relevant acting forces need to be taken into account in the calculations, namely gravity/buoyancy, drag, added (virtual) mass, transversal lift, fluid inertia, wall-lubrication and Basset (history term) forces. Contrastively to solid particles, bubbles present a constant shape oscillation during their rise, coupled with a tumbling motion. In this work, despite use of “point-particle” approximation, such dynamics was included in the model by first assuming an instantaneous bubble eccentricity and considering it in the forces. Subsequently, the tumbling motion is induced by changing the direction of bubble motion from a straight path. In order to save computational time, the local prediction of bubble eccentricity and motion angle is performed stochastically, yet correlated in time making use of experimental observations with regard to oscillations frequencies and amplitudes. This process mimics the bubble dynamics efficiently through a single-step Langevin equation, maintaining also certain simplicity on the model. Moreover, an evaluation of forces competition in a laboratory bubble column is realized in terms of bubble equivalent diameter and spatial coordinates, namely, radial and axial positions. After all, the modelling of shape and trajectories oscillations revealed a greater importance of added mass and Basset forces than observed with the base model. It was also noticed, that the history term acts as a resistance to the motion change, inasmuch as the bubble velocity fluctuations are weakened. Nonetheless, this force enhances an overall bubble lateral dispersion. Finally, the formulation is extended for cases with mass transfer, in which a dynamic Sherwood number is combined with the bubble dynamics model. Conclusively, the CFD model implemented here (platform OpenFOAM) is suitable for predicting flows and mass transfer in bubble columns and accounts for bubble dynamics in the frame of Euler/Lagrange approach.

# Summary

<b>1</b>	<b>INTRODUCTION.....</b>	<b>1</b>
<b>1.1</b>	<b>Objectives of the Thesis .....</b>	<b>5</b>
<b>2</b>	<b>MATHEMATICAL MODELLING.....</b>	<b>9</b>
<b>2.1</b>	<b>Continuous phase .....</b>	<b>9</b>
<b>2.2</b>	<b>Discrete phase.....</b>	<b>12</b>
<b>2.3</b>	<b>SGS Dispersion Model.....</b>	<b>21</b>
<b>2.4</b>	<b>Solution algorithm.....</b>	<b>22</b>
<b>2.5</b>	<b>Oscillation Model .....</b>	<b>23</b>
<b>3</b>	<b>RESULTS – BUBBLE MOTION .....</b>	<b>27</b>
<b>3.1</b>	<b>Bubble Trajectories.....</b>	<b>27</b>
3.1.1	Test Cases descriptions and setup.....	27
3.1.2	Results and discussion .....	29
<b>3.2</b>	<b>Bubble Swarms – Study Case I.....</b>	<b>33</b>
3.2.1	Cases descriptions and setup.....	33
3.2.2	Results and discussion .....	38
<b>3.3</b>	<b>On the Forces Competition .....</b>	<b>62</b>
3.3.1	Cases descriptions and setup.....	62
3.3.2	Magnitude ratio .....	63
3.3.3	Overall radial contribution .....	69
<b>3.4</b>	<b>Basset Force and Dispersion .....</b>	<b>73</b>
3.4.1	Cases descriptions and setup.....	73
3.4.2	Results and discussion .....	75
<b>3.5</b>	<b>Bubble Swarms – Study Case II .....</b>	<b>80</b>
3.5.1	Cases descriptions and setup.....	80
3.5.2	Prior results and further model adaptations .....	83
3.5.3	Final results and discussion.....	88
<b>3.6</b>	<b>Conclusions of the chapter .....</b>	<b>93</b>
<b>4</b>	<b>ON THE MASS TRANSFER.....</b>	<b>97</b>
<b>4.1</b>	<b>Modelling the mass transfer.....</b>	<b>99</b>
4.1.1	Continuous phase .....	99

4.1.2	Discrete phase.....	100
4.1.3	Mass transfer model .....	101
4.1.4	Thermodynamic properties.....	104
<b>5</b>	<b>RESULTS – MASS TRANSFER .....</b>	<b>107</b>
<b>5.1</b>	<b>Single Bubbles .....</b>	<b>107</b>
5.1.1	Case descriptions and setup.....	107
5.1.2	Results and discussion .....	109
<b>5.2</b>	<b>Bubble Swarms .....</b>	<b>115</b>
5.2.1	Case description and setup .....	115
5.2.2	Results and discussion .....	117
<b>5.3</b>	<b>Conclusions of the chapter .....</b>	<b>124</b>
	<b>CONCLUSIONS AND OUTLOOK .....</b>	<b>125</b>
	<b>NOMENCLATURE .....</b>	<b>129</b>
	<b>REFERENCES .....</b>	<b>133</b>



# 1 Introduction

Bubble columns are often used as chemical reactors, where large contact area between gas and liquid phases has to be achieved. Either in the oil refineries, chemical or pharmaceutical industries, high efficiency in terms of mass or heat transfer is desired. Computational Fluid Dynamics (CFD) can be a very useful tool to predict the flow and transfer rates in such apparatus. However, its modelling is still a challenge, since the flow structure is highly influenced by the bubbles. During their ascension, bubbles are constantly changing their size, due to mass transfer, or even to difference in hydrostatic pressure, not mentioning shape and motion oscillations. These complex phenomena demand sophisticated mathematical models, in order to be well represented.

The Euler/Lagrange approach for numerical calculations of dispersed multiphase flows is a powerful method for analysing and optimising industrial scale processes. The main reasons for that are the easy consideration of particle size distributions and the descriptive modelling of transport phenomena occurring on the scale of the particles [1]. This method has been applied very often for bubble columns [2,3,4,5]. Hence, although the particles are considered as point-masses their discrete nature is maintained in the simulations in contrary to an Euler/Euler modelling, where the particle phase properties appear only as averages in a control volume used for numerically discretizing the apparatus. Here not only the liquid phase is treated as a continuum, but also the dispersed phase [6,7].

In both of these approaches, the interaction between the phases is modelled accounting for the relevant interfacial and field forces. Lucas et al. [8] and Rzehak et al. [9] describe the importance of the interfacial forces to be considered for the two-fluid approach (Euler/Euler), and proposed the developed model as a baseline for simulations of bubbly flows. Naturally, force correlations used in simulations have empiric precedence, in which the correspondent

coefficients are commonly elaborated with characteristic dimensionless numbers. At last, the most important role in the estimation of these forces is played by the bubble size. This property can be handled in the Euler/Lagrange approach without additional numerical complexity, though, even when mass transfer, bubble breakage and coalescence phenomena are involved [10,11,12,13].

Once the gas and liquid phases are directly coupled, the proper solving of the liquid flow and turbulence in bubble columns is also essential. In Euler/Lagrange applications for dispersed bubbly flows, the most preferred method is the Large Eddy Simulation (LES). This method has some advantage over Reynold-Average Navier-Stokes (RANS) by resolving directly large structures in the core of bubble columns, which carry most the flow energy [14]. The smaller and weaker eddies, on the other hand, can be modelled using a sub-grid-scale (SGS) turbulence model, e.g., the well-known Smagorinsky [15]. Furthermore, the presence and motion of bubbles can promote and dissipate turbulence in the liquid phase, the so-called Bubble-Induced Turbulence (BIT). The BIT modelling is frequently discussed in the literature and various models are available [16,17,18]. Lain et al. [3] introduced a consistent turbulence model in the frame of k-epsilon turbulence model by using the bubble interface velocity in deriving the k-equation source term. Later, this model was adapted for LES applications [19] by a considering an additional contribution to the SGS viscosity.

In order to calculate the particle motion, especially if they are larger and hence their Reynolds number is well above unity, resistance coefficients are needed for all relevant forces [20]. Depending on the density ratio (i.e. material components and particle to fluid density) and their size a number of forces are important as presented by Maxey and Riley [21] for Stokes flow. These are for example the drag force, gravity and buoyancy, fluid inertia (part of the pressure term), added mass (also called as virtual mass) and Basset term.

The drag coefficient of single bubbles has been extensively studied in the literature, consider for example the works from Ishii and Zuber [22], Mei et al. [23], Tomiyama et al. [24] and Yan et al. [25]. Based on the bubble equivalent diameter and fluid properties, these models are suitable for a large range of Reynolds and Eötvös dimensionless numbers. Nevertheless, some correlations which account for bubble eccentricity are also available in the literature, e.g., works from Moore [26] and Rastello et al. [27]. This last one was evaluated recently by Aoyama et al. [28] for various Morton numbers and agreed very well with experimental data.

In most simulations of bubbles found in the literature, the virtual mass coefficient is assumed to be 0.5, which corresponds to a sphere. However, since the added mass is related to

---

the volume of fluid displaced by the particle, Lamb [29] provided an analytical solution for an unbounded oblate-ellipsoid as function of its eccentricity, showing that the coefficient can be much different to the solution for a sphere. Direct Numerical Simulations performed by Simcik et al. [30] are in agreement with the results obtained analytically by Lamb [29] and the authors extended the correlation for a bounded situation, namely in the vicinity of parallel and perpendicular walls.

In addition the transverse lift force is of immense importance in bubbly flows. In most numerical calculations of bubbly flows the well-established correlation for the lift coefficient proposed by Tomiyama et al. [31] is applied. Recent studies highlighted that this correlation is strictly speaking only valid for systems with higher viscosity [32,33]. In the low bubble Reynolds number regime, the lift coefficient may be described with the correlation proposed by Legendre and Magnaudet [34] for spherical particles. For higher bubble Reynolds numbers, the lift coefficient changes its sign from positive (towards the wall) to negative (towards the core). This point was defined as the critical Reynolds number. According to Aoyama et al. [33], this value is highly dependent on the Morton number and a correlation for it was proposed. When applied for water-air systems, the resulting critical Reynolds number is completely different than the one predicted by Tomiyama et al. [31]. Ziegenhein et al. [35] proposed recently a new experimental method for evaluating the lift coefficient in low viscosity systems, in which a linear shear is produced by a bubble plume instead of rotating belts. The resulting new findings also reveal a sooner reversal of lift coefficient, but invalidate an extrapolation of Aoyama's correlation to water-system. According to them, the reasonable choice is so far to use a correlation based on the modified Eötvös number, depending on the major axis of the bubble instead on the volume equivalent diameter. In this manner, the bubble eccentricity is included in the formulation, either.

Not only the added mass, but also the drag and transversal lift forces can be influenced by the presence of a wall. Such effects have been evaluated by Takemura and Magnaudet [36] for low and moderate bubble Reynolds numbers. In their approach, a correlation for modelling wall effects is provided by modifying drag and lift coefficients directly. A different approach is applied by Antal et al. [37] and Tomiyama et al. [38], where an extra force is used to account for such effects, while drag and lift correlations remain unchanged. Later, Hosokawa et al. [39] improved their model not only by considering two regimes, one correlated by Reynolds and the other by Eötvös numbers, but also by reducing the number of resistance coefficients. In the recent past, Jeong and Park [40] conducted experiments with deformable bubbles with high Reynolds number. As expected, the bubbles presented strong

path oscillations, but due to this fact they could not quantify directly the wall effect, unfortunately. However, it was observed that the bubble velocity and oscillations frequencies were significantly influenced in a bounded flow.

Irrespective of particle size and particle Stokes number (i.e. defined as the particle response time scale with respect to the relevant fluid time scale) the Basset term is mostly neglected with the argument that this integral force (or history force) to be determined along the entire particle trajectory is numerically very expensive. This assumption is probably not valid when considering bubbly flows as for example found in industrial bubble column reactors (see also Sommerfeld et al. [20]). According to Takemura and Magnaudet [36], the frequency of bubble motion oscillations is too high, so that the bubble wake cannot be always perfectly aligned with its velocity. In this manner, considerable values of the Basset force were obtained in their experimental work and this term should not be neglected in any Lagrangian computation of bubble motion. In order to reduce the numerical effort in evaluating the Basset term, approximations of the history term are available in the literature, e.g., works from Michaelides [41] and Hinsberg et al. [42]. In the last one, an exponential function is applied to approximate the tail of the force kernel. The method is second order in time and reduces the computational effort by more than one order of magnitude. Furthermore, Michaelides and Roig [43] suggested a reinterpretation of the data provided by Odar and Hamilton [44] and subsequently an improved correlation for the Basset coefficient, needed for higher particle Reynolds numbers.

From experimental observations it is known that bubbles perform oscillations during their ascent, coupled with a tumbling motion [45,46,47,48,49,50,51]. Such dynamics cannot be attained by only assuming a stationary drag coefficient, as the ones mentioned above. Recently, Sommerfeld et al. [52] included in Euler/Lagrange simulations the bubble eccentricity and an oscillation model, in order to mimic bubble dynamics. The stochastic generation of eccentricity and motion angle improved substantially the velocity fluctuations in bubbly flows. The Basset force was by then neglected, and bubble eccentricity was considered only in the lift force.

Although plenty of numerical studies on bubble columns have been conducted with “point-mass” approximations, the effect of bubble dynamics and oscillation has been rarely considered. The influence of bubble eccentricity is mostly only accounted in the lift force, making use of a modified Eötvös number [31]. Even with the two-fluid approach, Leon-Becerril et al. [53] demonstrate that the stability of a bubble column is largely influenced by accounting bubble eccentricity on drag and added mass forces. Mohd Akbar et al. [54] use a



---

fictitious lateral force acting on bubbles for predicting lateral oscillations, in which frequencies and amplitudes are input parameters for the model. In this same paper, the authors provide an extensive experimental and numerical evaluation in a rectangular bubble column. However, the results shown for only one cross-section, were focused mostly on the liquid phase and no information about bubble fluctuations is available. A physical based bubble dynamics model was introduced by Bourloutski and Sommerfeld [55], making use of experimental information about oscillation frequencies and eccentricity in dependence of bubble size.

Sommerfeld and Bröder [56] conducted several experiments in a laboratory bubble column, varying gas flow rate and bubble size distribution. In their work, velocities and fluctuations of both liquid as well as gas phase were measured along the whole column, giving full support for the validation of CFD models. Additionally, information about bubble eccentricity, orientation and motion angle are also available. To the best of the authors knowledge such detailed experimental data from bubble swarms is not found anywhere else. Due to this fact, this experimental work was the greatest motivation of the present thesis.

## 1.1 Objectives of the Thesis

The main goal of the present work is to highlight the importance of modelling bubble dynamics on motion and mass transfer within the frame of Euler/Lagrange point-particle approach. In order to do so, several particular steps were required, which will be described in the following.

From the numerical point of view, the CFD model developed here should be able to predict the flow and mass transfer in bubble columns, taking into account effects of bubble dynamics, such as shape oscillations and tumbling motion. The solution of conservation and governing equations are performed in the open-source platform OpenFOAM (v4.1). Apart from being non-commercial, other advantage in using this code is the possibility of modifications and new implementations by the user. Additionally, the OpenFOAM has a large community worldwide, which is constantly growing and contributing to new libraries and solvers. However, at the beginning of this doctoral study, all the standard solvers in OpenFOAM with Euler/Lagrange approach were designed for parcels heavier than the Eulerian phase, such as solid particles or droplets, but not for bubbles. The only force already implemented which is related to bubbles was the well-known Tomiyama et al. [31] lift correlation. In this manner, some implementation tasks in OpenFOAM 4.1 were established in the present work:

- to adapt the standard Lagrangian tracking for buoyant parcels (bubbles);
- state of art of relevant forces acting on bubbles;
- an improved SGS turbulent dispersion model through Langevin equation;
- to include BIT modelling on SGS turbulence;
- hybrid solution of the Euler/Lagrange approach with Volume of Fluid (VoF) for resolving the free surface at the column top (bubbles remain discrete);
- mapping function of parcels variables to the numerical mesh for proper statistical assessment of the discrete phase (avg. velocities, fluctuations, diameter, volume fraction);
- stochastic prediction of bubble eccentricity and tumbling motion (bubble dynamics);
- improved bubble tracking accounting for relevant time-scales, such as response-time, oscillation period, SGS turbulence integral time;
- equation of state (ideal gas) for dynamic modification of bubble density and equivalent diameter;
- dynamic mass transfer model which accounts for oscillation amplitude.

Although all the aspects described above were not available in OpenFOAM, the platform satisfied all the requisites for a basic structure of CFD coding.

From the validation point of view, different study cases were chosen for support a solid comparison with experimental data. Since the CFD model consists of many peculiarities, the validation process must be conducted step-by-step with growing complexity, as follows:

- verify the uncoupled solution from a single rising bubble using a very basic model, considering only drag and added mass forces;
- verify the coupling between liquid and dispersed phases;
- extend the solution for bubble swarms;
- include all relevant forces;
- first comparison with experimental data;
- further model development by including bubble dynamics;
- validate the model for different geometries, superficial velocities and bubble size distributions by comparison with other experimental data;
- extend the model for mass transfer for one or more chemical species;

- 
- validate the mass transfer model for single bubbles by comparison with experimental data;
  - validate the mass transfer model for bubble swarms.

In the end, the actual interest of developing CFD models for bubble columns is the capability of predicting chemical reactions, conversion rates and product selectivity. However, before reaching this goal, the proper solution of motion and mass transfer is fundamental. Bubble dynamics, the main focus of the present work, is of a great importance but rarely considered in bubble column simulations. Although the model developed here ends at mass transfer, it may be used as a basis for future implementations with chemical reactions.



# 2 Mathematical Modelling

The following CFD model was developed and implemented in the open source platform OpenFOAM®. Designed for simulation of discrete bubbles rising in a continuous liquid phase, this model was based on the Euler/Lagrange approach. Besides “point-mass” approximations for the dispersed phase, a model extension which accounts for bubble dynamics is suggested.

## 2.1 Continuous phase

In the present work the Large Eddy Simulation (LES) approach was used for solving the flow field and modelling SGS turbulence of the continuous phase. A Volume of Fluid (VoF) model is used in the calculations, in order to solve a second continuous phase (air) above the water level. Thus, an additional equation for the volume fraction is required and a simple compression method for the free surface was applied, i.e., a surface reconstruction is not performed. The governing equations are showed in the Table 2-1.

Table 2-1: Continuous phase governing equations.

Continuity	$\frac{\partial(\alpha_c \rho_c)}{\partial t} + \nabla \cdot (\alpha_c \rho_c \mathbf{u}_c) = 0$	(2-1)
Momentum	$\frac{\partial(\delta_c \mathbf{u}_c)}{\partial t} + \nabla \cdot (\delta_c \mathbf{u}_c \mathbf{u}_c) = -\nabla p - \nabla \cdot (\delta_c \boldsymbol{\tau}_c) + \delta_c \mathbf{g} - \mathbf{F}_\sigma + \overline{\mathbf{S}_{u,p}}$	(2-2)
	$\boldsymbol{\tau}_c = -\mu_{eff} \left\{ (\nabla \mathbf{u}_c + (\nabla \mathbf{u}_c)^T) - \frac{2}{3} I(\nabla \cdot \mathbf{u}_c) \right\}$	
Volume Fraction	$\frac{\partial(\alpha_B \alpha_L)}{\partial t} + \nabla \cdot (\alpha_B \alpha_L \mathbf{u}_c) + \nabla \cdot [\alpha_B \alpha_L (1 - \alpha_L) \mathbf{u}_R] = 0$	(2-3)
Continuity	with: $\begin{cases} \text{mixture density} & \delta_c = \alpha_L \rho_L + \alpha_G \rho_G + \alpha_B \rho_B \\ \text{within the bubbly liquid} & \alpha_c = 1 - \alpha_B \end{cases}$	(2-4)

in which,  $\delta_c$  is the effective mixture density of for the entire system including the column part and the free space above the liquid surface,  $\alpha_G$  is the volume fraction of the gas above the surface (this property is needed since the interface will be resolved only over several grid cells),  $\alpha_c$  and  $\alpha_L$  are both the liquid volume fractions corresponding also to the volume fraction of the carrier phase within liquid column due to the presence of bubbles with the volume fraction  $\alpha_B$ . The relevant densities are the continuous phase density  $\rho_c$  either being the liquid density  $\rho_L$  within the column, or the gas density above the interface  $\rho_G$ , and the bubble internal density  $\rho_B$ . The velocity vector of the carrier phase is  $\mathbf{u}_c$ , the shear stress is  $\boldsymbol{\tau}_c$ , the pressure  $p$  and  $\mathbf{g}$  is the gravitational field. The surface tension force resulting from the free surface is  $\mathbf{F}_\sigma$ , which follows from:

$$\mathbf{F}_\sigma = \sigma \kappa \mathbf{n} \delta_\Gamma \quad (2-5)$$

$$\kappa = \nabla \cdot \mathbf{n} \quad (2-6)$$

$$\mathbf{n} = \frac{\nabla \alpha_L}{|\nabla \alpha_L|} \quad (2-7)$$

in which  $\sigma$  is the surface tension,  $\kappa$  the surface curvature term obtained from the normal vector  $\mathbf{n}$ , and a delta of Dirac function  $\delta_\Gamma$ , which acts only at the surface  $\Gamma$ . The cell-based momentum source-term  $\overline{\mathbf{S}_{u,p}}$  regarding to the phases interactions is expressed by the Equation (2-8), by summing over all traversing parcels  $k$  and the number of Lagrangian time steps  $n$  as follows:

$$\overline{\mathbf{s}}_{u,p} = -\frac{1}{V_{cv}\Delta t_E} \sum_k m_k N_k \sum_n \left[ (\mathbf{u}_k^{n+1} - \mathbf{u}_k^n) - \mathbf{g} \left( 1 - \frac{\rho_L}{\rho_B} \right) \Delta t_L \right] \quad (2-8)$$

in which,  $V_{cv}$  is the cell volume,  $\Delta t_E$  and  $\Delta t_L$  are the Eulerian and Lagrangian time-steps, respectively and  $m_k$  is the mass of an individual bubble.  $N_k$  is the number of real bubbles in the parcel  $k$ , which was fixed to one real bubble in all the present cases.  $\mathbf{u}_k^n$  and  $\mathbf{u}_k^{n+1}$  are the bubble velocities at the beginning and the end of a Lagrangian time step,  $\rho_c$  and  $\rho_B$  are the density of the liquid and gas phase, respectively. More details about the coupling will be described further in this work.

The effective viscosity  $\mu_{eff} = \mu_c + \mu_{t,c}$  for the continuous phase is composed of two contributions: the molecular viscosity  $\mu_c$  and the turbulent viscosity  $\mu_{t,c}$ . The turbulent viscosity accounts for the contribution of the sub-grid scales and it was described by the Smagorinsky model [15]. Additionally, a bubble contribution to the turbulent viscosity  $\mu_{t,p}$ , also called as bubble-induced turbulence (BIT), is also considered [3], as follows:

$$\mu_{t,c} = \rho_c (\Delta C_s)^2 \sqrt{2 \overline{S_{i,j}} \overline{S_{i,j}}} + \mu_{t,p} \quad (2-9)$$

$$\overline{S_{i,j}} = \frac{1}{2} (\nabla \mathbf{u}_c + (\nabla \mathbf{u}_c)^T) \quad (2-10)$$

$$\mu_{t,p} = \rho_c (C_s \Delta) \sqrt{\frac{\Delta t_E}{\rho_c} S_{k,p}} \quad (2-11)$$

$$S_{k,p} = \sum_{i=1}^3 (\overline{u_{B,i} S_{u,p,i}} - u_c \overline{S_{u,p,i}}) \quad (2-12)$$

Here, the SGS length scale is giving by  $\Delta$ , based on the volume of the computational cell and  $C_s$  is a model constant with a standard value of  $C_s = 0.094$  used in many simulations. Moreover,  $\overline{S_{i,j}}$  is the symmetric deviatoric part of strain tensor of the resolved scales.

In order to improve the solution of LES equations in the vicinity of the wall, a wall function was used. This method avoids the integration of model equations, economizing computational resources by making use of the universal behaviour of flows near to a wall [57]. In this framework, a SGS turbulent viscosity is calculated based on the local turbulent kinematic energy.

## 2.2 Discrete phase

In this work all relevant forces such as drag, gravity/buoyancy, transverse lift, fluid inertia, added mass, wall-lubrication and Basset (history-term) were considered. Thus, the bubble tracking is described by the Equations (2-13) and (2-14), as follows:

$$\frac{d\mathbf{x}_B}{dt} = \mathbf{u}_B \quad (2-13)$$

$$\begin{aligned} m_B \frac{d\mathbf{u}_B}{dt} = & \frac{3}{4} \frac{\rho_L}{\rho_B d_B} m_B C_D (\mathbf{u}_L - \mathbf{u}_B) |\mathbf{u}_L - \mathbf{u}_B| + C_{AM} m_B \frac{\rho_c}{\rho_B} \left( \frac{D\mathbf{u}_L}{Dt} - \frac{d\mathbf{u}_B}{dt} \right) \\ & + C_L m_B \frac{\rho_L}{\rho_B} [(\mathbf{u}_L - \mathbf{u}_B) \times (\nabla \times \mathbf{u}_L)] + m_B \frac{\rho_L}{\rho_B} \frac{D\mathbf{u}_L}{Dt} + m_B \mathbf{g} \left( 1 - \frac{\rho_L}{\rho_B} \right) + \\ & + m_B \frac{2}{d_B} C_{BW} \left( \frac{d_B}{2x} \right)^2 \rho_c |(\mathbf{u}_L - \mathbf{u}_B) \cdot \mathbf{k}|^2 \mathbf{n} + C_B \int_{-\infty}^t K_B(t - \tau) \mathbf{f}(\tau) d\tau \end{aligned} \quad (2-14)$$

in which,  $\mathbf{x}_B$ ,  $\mathbf{u}_B$ ,  $m_B$  are the bubble position vector, velocity and mass, respectively,  $C_D$  is the drag coefficient,  $C_{AM}$  the added mass coefficient,  $C_L$  the transversal lift coefficient,  $C_{BW}$  the wall-force coefficient,  $C_B$  the Basset-force coefficient,  $K_B$  the Basset integration kernel,  $\mathbf{f}(\tau)$  the derivative of the relative velocity between the bubble and the liquid phase,  $\mathbf{k}$  and  $\mathbf{n}$  are unit vectors parallel and normal to the wall, respectively, and  $x$  is the distance between the wall and bubble centre.

The model still requires a closure for the forces taken into account. The drag coefficient was evaluated at first by the well-known Tomiyama et al. model for fluid bubbles [24], dependent on bubble Reynolds and Eötvös dimensionless numbers, as follows:

$$C_D = \max \left\{ \min \left[ \frac{16}{Re_B} (1 + 0.15 Re_B^{0.687}), \frac{48}{Re_B} \right], \frac{8}{3} \frac{Eo}{Eo + 4} \right\} \quad (2-15)$$

$$Re_B = \frac{\rho_c d_B |\mathbf{u}_B - \mathbf{u}_L|}{\mu_L} \quad Eo = \frac{|\mathbf{g}| |\rho_L - \rho_B| d_B^2}{\sigma} \quad (2-16)$$

This correlation will be referred further in this work as “D1” (drag model 1). Here, the drag dependency on bubble size comes from the equivalent diameter. Nevertheless, the range of application of Eq. (2-15) extends also for the wobbling regime, where the bubbles are not



spherical. This means that an expected bubble eccentricity is somehow considered, but the information is implicit in the fitting parameters.

In order to explicitly account for instantaneous bubble eccentricity  $\chi$  on the drag coefficient, the model proposed by Rastello et al. [27] was also evaluated. This model makes use of a modified correlation based on Mei et al. [23] and the geometric factors  $G_\chi$  and  $H_\chi$  calculated by Moore [26] and approximated by Loth [58], as follows:

$$C_{D,Re,\chi} = \frac{16}{Re_B} \left\{ \frac{1 + \frac{8}{15}(\chi - 1) + 0.015(3G_\chi - 2)Re_B}{1 + 0.015Re_B} + \left[ \frac{8}{Re_B} + \frac{1}{2} \left( 1 + \frac{3.315H_\chi G_\chi}{\sqrt{Re_B}} \right) \right]^{-1} \right\} \quad (2-17)$$

$$G_\chi \cong 0.1287 + 0.4256\chi + 0.4466\chi^2$$

$$H_\chi \cong 0.8886 + 0.5693\chi - 0.4563\chi^2 \quad (2-18)$$

where  $\chi$  is the ratio between the bubble major axis and the minor one, i.e.,  $\chi \geq 1$ . Naturally, correlations for the estimation of bubble eccentricity are needed in the simulations. Such details will be shown later in this work.

The Eq. (2-17) was evaluated by Aoyama et al. [28] for various Morton numbers and predicted bubble terminal velocities very well when a proper correlation for the eccentricity is combined. However, the data presented by Rastello et al. [27] extend until Reynolds numbers around  $Re_B \sim 300$ . The drag coefficient for higher values of  $Re_B$  using Eq. (2-17) may be underestimated and are better represented in the literature in function of Eötvös number. In this manner, the same approach from Tomiyama et al. [24] can be used for elaborating a function that is valid for the whole range of bubble size, as follows:

$$C_D = \max(C_{D,Re,\chi}, C_{D,Eo}) \quad (2-19)$$

$$C_{D,Eo} = \frac{8}{3} \frac{Eo}{Eo + 4} \quad (2-20)$$

In order to take account for fluctuations of drag due to bubble eccentricity also in the Eq. (2-20), a modification is proposed assuming a deviation of instantaneous bubble eccentricity to the correspondent mean value, making use of the modified bubble Eötvös number  $Eo_h$ , as follows:

$$C_{D,\chi} = \max(C_{D,Re,\chi}, C_{D,Eo,\chi}) \quad (2-21)$$

$$C_{D,Eo,\chi} = C_{D,Eo} + (C_{D,Eoh} - C_{D,\overline{Eoh}}) \quad (2-22)$$

$$C_{D,Eoh} = \frac{8}{3} \frac{Eo_h}{Eo_h + 4} \quad (2-23)$$

$$Eo_h = \frac{|g| |\rho_L - \rho_B| d_h^2}{\sigma} \quad (2-24)$$

$$d_h = d_B \sqrt[3]{\chi} \quad (2-25)$$

where  $d_h$  is the bubble major axis. Note that the term inside the parenthesis of Eq. (2-22) is null when  $d_h = \overline{d_h}$ , retrieving the Eq. (2-20). Hence, this approach does not affect the resulting time-averaged drag coefficient, after all, but accounts for instantaneous modifications when the bubble eccentricity is not considered constant. The Eq. (2-21) will be referred in this work as “D2” (drag model 2).

The added mass coefficient was also evaluated with dependency of bubble eccentricity, according to analytical solutions of Lamb [29]. Additionally, an increase is noticed at the vicinity of a wall [30], as follows:

$$C_{AM} = A \cos(2\theta) + B \quad (2-26)$$

$$A = \frac{C_{pe} - C_{pa}}{2} \quad B = \frac{C_{pe} + C_{pa}}{2} \quad (2-27)$$

$$C_{pe} = C_e \left[ 1 + \frac{3}{8} \left( \frac{d_h}{2x} \right)^3 \right] \quad C_{pa} = C_e \left[ 1 + \frac{3}{16} \left( \frac{d_h}{2x} \right)^3 \right] \quad (2-28)$$

$$C_{e(\text{oblate})} = \frac{E \cos^{-1} E - \sqrt{1 - E^2}}{E^2 \sqrt{1 - E^2} - E \cos^{-1} E} \quad (2-29)$$

$$E = \frac{1}{\chi} \quad d_h = d_B \sqrt[3]{\chi} \quad (2-30)$$

where  $d_h$  is the major axis of the non-spherical bubble,  $\theta$  is the angle between the bubble motion direction and the wall,  $x$  is the wall distance to the bubble centre ( $x \geq 0.5d_h$ ), and  $C_{pe}$  and  $C_{pa}$  are the coefficients with regard to perpendicular and parallel walls, respectively. At this point, the model combines the wall influence with the coefficient  $C_e$  in function of bubble axis ratio  $E$ , i.e. the inverse of the eccentricity  $\chi$ .

In the present work the most recent data for the lift coefficient were evaluated. Until nowadays, the probably most used lift correlation for bubbles, proposed by Tomiyama et al. [31], is considered in many simulations. This model predicts the lift coefficient with dependency on Eötvös and Reynolds numbers, as follows:

$$C_L = \begin{cases} \min[0.288 \tanh(0.121 Re_B), f(Eo_h)] & Eo_h \leq 4 \\ f(Eo_h) & 4 < Eo_h \leq 10 \\ -0.288 & 10 < Eo_h \end{cases} \quad (2-31)$$

$$f(Eo_h) = 0.00105 Eo_h^3 - 0.0159 Eo_h^2 - 0.0204 Eo_h + 0.474 \quad (2-32)$$

$$Eo_h = \frac{|\mathbf{g}| |\rho_L - \rho_B| d_h^2}{\sigma} \quad (2-33)$$

The Eq. (2-31) will be referred in this work as “L1” (lift model 1).

In order to proper account for fluid viscosity, a different approach needs to be considered. In a recent past, Aoyama et al. [33] observed experimentally that for low bubble Reynolds numbers, the lift coefficient can be modelled making use of Legendre and Magnaudet [34] correlation (Eq. (2-34)) for spherical particles, since the bubbles are small enough and behave as particles. The resulting coefficient increases with Re until a certain limit around 0.4-0.5. After a certain bubble size, the results reveal a critical Reynolds number, where the lift coefficient changes the sign from positive to negative. The authors noticed a clear dependency of this value with the Morton number and proposed a correlation for it (Eq. (2-36)), as follows:

$$C_{L0} = \sqrt{\left(\frac{6}{\pi^2} \frac{2.255}{\sqrt{Sr} Re [1 + 0.2 Re/Sr]^{3/2}}\right)^2 + \left(\frac{1 Re + 16}{2 Re + 29}\right)^2} \quad (2-34)$$

$$Sr = \frac{d_B |\nabla \times \mathbf{u}_L|}{|\mathbf{u}_B - \mathbf{u}_L|} \quad (2-35)$$

$$Re_c = 9M^{-0.173} (1 + 14M^{0.29})^{-0.89} \quad (2-36)$$

$$M = \frac{\mu_c^4 |\rho_L - \rho_B| |\mathbf{g}|}{\rho_L^2 \sigma^3} \quad (2-37)$$

Applying the Eq. (2-36) for air-water systems ( $\log_{10} M = -10.6$ ), a critical Reynolds number  $Re_c \approx 607$  is obtained. However, such a system is out of range of their experiments ( $\log_{10} M > -6.6$  and  $Re_B < 120$ ) and such extrapolation may be unreliable. This lack of data

for low viscosity fluids was filled very recently by Ziegenhein et al. [35]. The authors proposed a new method to determine the lift coefficient in the oscillating regime, in which a bubble plume is used to produce a linear shear inside the column. The results for the transition from positive to negative lift coefficients are similar to those predicted by Dijkhuizen et al. [59] with Direct Numerical Simulations (DNS), however, a slightly softer slope was obtained, as follows:

$$C_{L,Eoh} = 0.002Eo_h^2 - 0.1Eo_h + 0.5 \quad (2-38)$$

The measured critical Reynolds number for the air/water system was around  $Re_c \approx 976$ , which is much higher than the value predicted by Eq. (2-36), i.e., its extrapolation for such lower Morton numbers is not valid. According to Ziegenhein et al. [35], the most reasonable choice would be a formulation based on the modified Eötvös number together with a proper bubble shape correlation. In this manner, the complete lift model used in the present work combines the Eqs. (2-34) and (2-38), as follows:

$$C_L = \max[\min(C_{L0}, C_{L,Eoh}), -0.25] \quad (2-39)$$

The data provided by Ziegenhein et al. [35] extends up to  $Eo_h \approx 10.5$  and the lift coefficient for greater bubbles is so far unknown. Hence, an under limit of  $C_L = -0.25$  was arbitrary chosen. The Eq. (2-39) will be referred in this work as “L2” (lift model 2).

Finally, a summary of all these lift models is shown in the Figure 2-1. Although the most of correlations in evaluation here are function of modified Eötvös number, a conversion to Reynolds number was also performed based on the terminal velocity of a single bubble with the correspondent equivalent diameter and mean eccentricity.

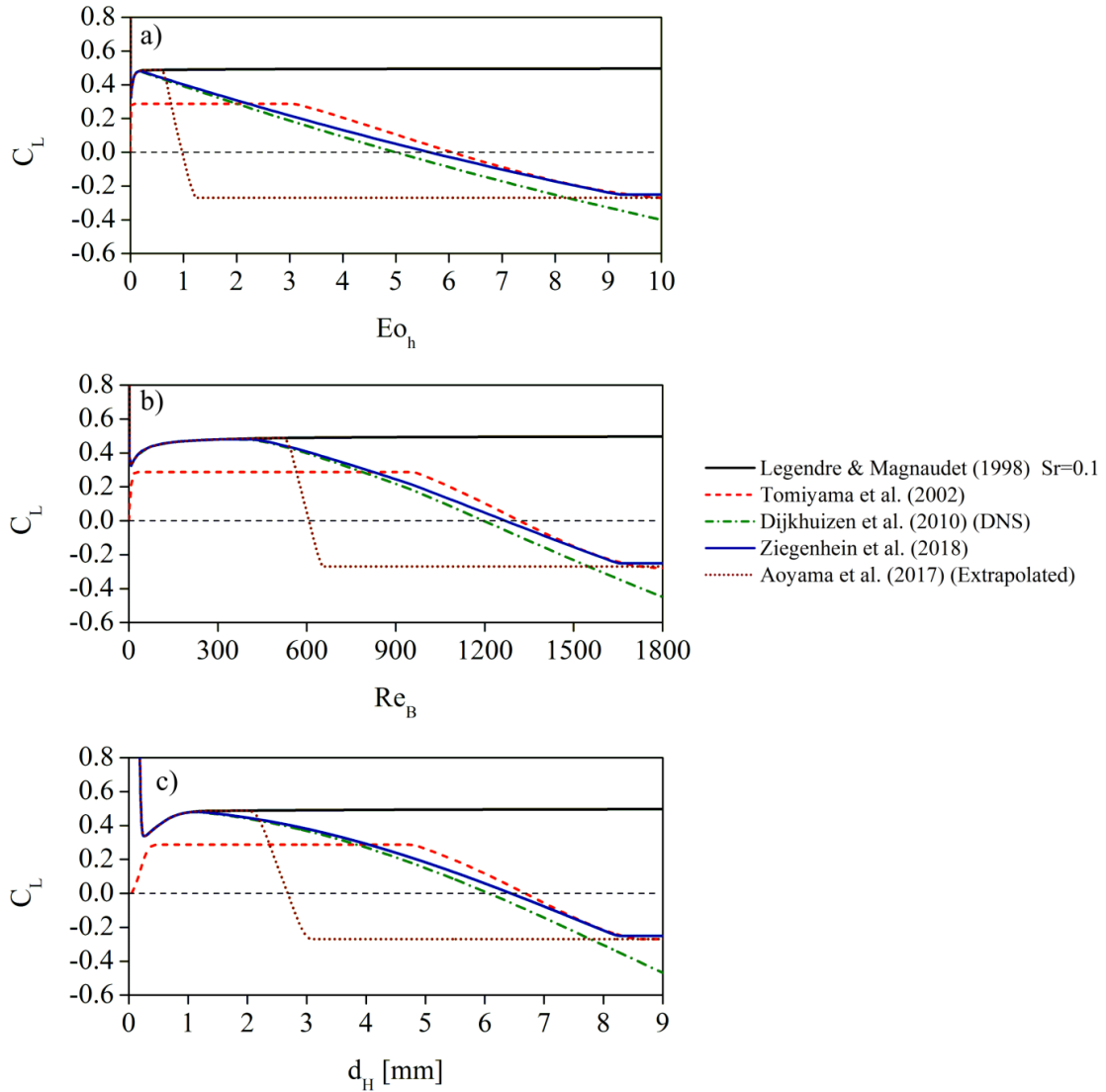


Figure 2-1: Comparison of lift models in function of: a) modified Eötvös number; b) Reynolds number; c) bubble major axis.

It is noticed in the Figure 2-1c that the lift models proposed by Tomiyama et al. [31] and Ziegenhein et al. [35] do not differ strongly for bubble horizontal diameters between 4 and 8 mm. On the other hand, discrepancies more than 50% are found for smaller bubbles ( $d_h < 3$  mm), which can impact significantly on further bubble dispersion and local size distribution.

The wall lubrication force coefficient was estimated with the model proposed by Hosokawa et al. [39], which is dependent on Reynolds and Eötvös numbers, as follows:

$$C_{BW} = \max \left\{ \frac{7}{Re_B^{1.9}}, 0.0217Eo \right\} \quad (2-40)$$

The Basset coefficient was calculated using the model from Michaelides and Roig [43], which is dependent on the Reynolds and Strouhal dimensionless numbers, as follows:

$$C_B = \left(\frac{d_B}{2}\right)^2 \sqrt{\pi\rho_L\mu_L} \{6.00 - 3.16[1 - \exp(-0.14Re_B Sl^{0.82})^{2.5}]\} \quad (2-41)$$

$$Sl = \frac{2.25T_L\mu_L}{\pi\rho_L d_B^2} \quad (2-42)$$

in which  $T_L$  is the integral time scale of SGS turbulence. The integral part from the Basset force was solved with the method from van Hinsberg et al. [42]. This method separates the integral in two parts. The first one is the time-window term  $\mathbf{F}_{B-win}$ , in which the properties necessary to calculate the force, such as  $\Delta t_L$ ,  $\mathbf{u}_B$ ,  $\mathbf{u}_L$  and  $C_B$  are stored in a finite list (history) with arbitrary N-size and a time-resolution from  $\Delta t_L$ . The second one is the called “tail”  $\mathbf{F}_{B-tail}$ , which represents the remaining part from the integral, as follows:

$$\mathbf{F}_B = \mathbf{F}_{B-win} + \mathbf{F}_{B-tail} \quad (2-43)$$

$$\mathbf{F}_{B-win} = C_B \int_{t-t_{win}}^t K_B(t-\tau) \mathbf{f}(\tau) d\tau \quad (2-44)$$

$$\mathbf{F}_{B-tail} = C_B \int_{-\infty}^{t-t_{win}} K_{tail}(t-\tau) \mathbf{f}(\tau) d\tau$$

The Basset Kernels  $K_B$  and  $K_{tail}$  will quantify the importance of each history term. As closer to the present time, higher will be its influence, as seen in the Figure 2-2.

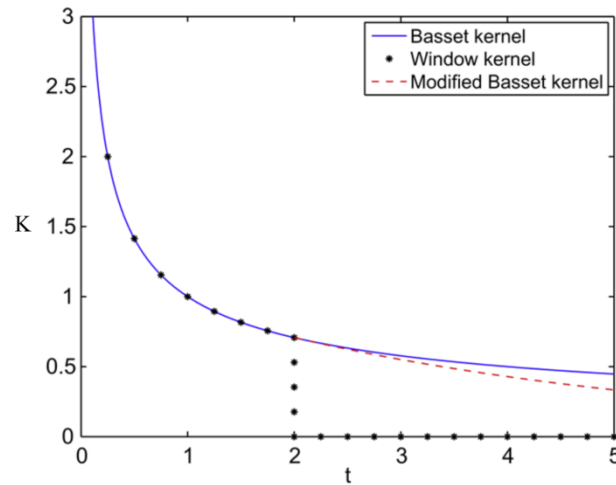


Figure 2-2: Illustration from the Basset kernel (solid line), window kernel (dots) and the modified Basset kernel (dashed line) for  $t_{win} = 2$ . Source: Hinsberg et al. [42].

The authors proposed a method to approximate these integrals in an effective way and with low computational efforts. The window term can be approximated with the following equation:

$$\begin{aligned} \mathbf{F}_{B-win} \approx & \frac{4}{3} C_B \mathbf{f}_0 \sqrt{\Delta t_L} + C_B \mathbf{f}_N \frac{\sqrt{\Delta t_L} \left( N - \frac{4}{3} \right)}{(N-1)\sqrt{N-1} + \left( N - \frac{3}{2} \right) \sqrt{N}} + \\ & + C_B \sqrt{\Delta t_L} \sum_{n=1}^{N-1} \mathbf{f}_n \left( \frac{n + \frac{4}{3}}{(n+1)\sqrt{n+1} + \left( n - \frac{3}{2} \right) \sqrt{n}} + \frac{n - \frac{4}{3}}{(n-1)\sqrt{n-1} + \left( n - \frac{3}{2} \right) \sqrt{n}} \right) \end{aligned} \quad (2-45)$$

in which N represents the size of the stored list. In the cases presented in this work a list of 10 were stored. On the other hand, the tail term is approximated by the authors with a finite sum as follows:

$$\mathbf{F}_{B-tail} = \sum_{i=1}^m a_i \mathbf{F}_i(t) \quad (2-46)$$

where  $m=10$  [42] and  $\mathbf{F}_i(t)$  is split into two parts either, a directly and a recursively computed ones, as follows:

$$\begin{aligned} \mathbf{F}_i(t) &= \mathbf{F}_{i-di}(t) + \mathbf{F}_{i-re}(t) \\ \mathbf{F}_i(t) &= C_B \int_{t-t_{win}-\Delta t_L}^{t-t_{win}} K_i(t-\tau) \mathbf{f}(\tau) d\tau + C_B \int_{-\infty}^{t-t_{win}-\Delta t_L} K_i(t-\tau) \mathbf{f}(\tau) d\tau \quad (2-47) \\ \mathbf{F}_{i-di}(t) &\approx 2C_B \sqrt{e t_i} \exp\left(-\frac{t_{win}}{2t_i}\right) \left\{ \mathbf{f}_N \left[ 1 - \varphi\left(-\frac{\Delta t_L}{2t_i}\right) \right] + \right. \\ &\quad \left. + \mathbf{f}_{N+1} \exp\left(-\frac{\Delta t_L}{2t_i}\right) \left[ \varphi\left(\frac{\Delta t_L}{2t_i}\right) - 1 \right] \right\} \quad (2-48) \end{aligned}$$

$$\mathbf{F}_{i-re}(t) \approx \exp\left(-\frac{\Delta t_L}{2t_i}\right) \mathbf{F}_i(t - \Delta t_L) \quad (2-49)$$

where:

$$\varphi(z) = \frac{(e^z - 1)}{z} = 1 + \frac{1}{2}z + \frac{1}{6}z^2 + \mathcal{O}(z^3) \quad (2-50)$$

$$t_i = t_{win} \tilde{t}_i \quad (2-51)$$

More details about the derivation of the model and its parameters can be found in the reference [42] and will not be discussed here.

The direct interaction of bubbles with the wall (collisions) was modelled with a correlation for the coefficient of restitution  $\epsilon$ , based on the capillary number  $Ca$  and a modified Stokes number  $St^*$  [60], as follows:

$$\epsilon = \exp\left(-30.0 \sqrt{\frac{Ca}{St^*}}\right) \quad (2-52)$$

$$Ca = \frac{\mathbf{u}_B \mu_L}{\sigma} \quad St^* = \frac{\mathbf{u}_B d_B (\rho_B + C_{AM} \rho_L)}{9 \mu_c} \quad (2-53)$$

In order to save computational time without losing temporal resolution, the Lagrangian time-step was not assumed as fixed. A first-order Euler integration of equations for bubbles position and velocities was used with a time step independently adjusted for each tracked bubble. This time step was dynamically adapted with respect to the relevant time-scales, such as from the drag response-time  $\tau_B$ , the SGS turbulence time-scale  $T_L$ , and the bubble oscillation period  $\tau_{osc}$ , this one according to Lunde and Perkins [45]. This means that a new value is calculated for every Lagrangian time-step choosing the minimum of these time-scales and making it one order of magnitude lower, as seen in the Eq. (2-54):

$$\Delta t_L = 0.1 \min(\tau_B, T_L, \tau_{osc}) \quad (2-54)$$

$$\tau_B = \frac{4 (\rho_B + 0.5 \rho_L) d_B^2}{3 \mu_L C_D Re_B} \quad (2-55)$$

$$\tau_{osc} = 2 \pi \left( \frac{16 \sqrt{2} \sigma \bar{\chi}^2}{\rho_L \left(\frac{d_B}{2}\right)^3 (1 + \bar{\chi}^2)^{3/2}} \right)^{-1/2} \quad (2-56)$$



## 2.3 SGS Dispersion Model

The sub-grid-scale (SGS) fluctuation of the fluid velocity seen by the bubbles was modelled through a single-step Langevin equation [19]. The model makes use of a single-step Langevin equation [20], dependent on Lagrangian and Eulerian correlation functions adapted for LES applications, as follows:

$$\dot{u}_i^{n+1} = R_{P,i}(\Delta t_L, \Delta r) \dot{u}_i^n + \sigma_c \sqrt{1 - R_{P,i}^2(\Delta t_L, \Delta r)} \xi_i \quad (2-57)$$

in which the superscripts denote the time step and the subscripts the spatial component.  $\Delta t_L$  is the aforementioned Lagrangian time step and  $\Delta r$  is the spatial separation between the fluid element and the bubble during the time  $\Delta t_L$ . The SGS turbulence may be considered to be isotropic so that  $\sigma_c$  represents the rms value of the fluid velocity fluctuation and  $\xi_i$  denote independent Wiener processes with zero mean and unit variance. The correlation functions  $R_{P,i}(\Delta t_L, \Delta r)$  have Lagrangian and Eulerian components, as follows:

$$R_{P,i}(\Delta t_L, \Delta r) = R_L(\Delta t_L) R_{E,ij}(\Delta r) \quad (2-58)$$

$$R_L(\Delta t_L) = \exp\left(-\frac{\Delta t_L}{T_L}\right) \quad (2-59)$$

$$R_{E,ij}(\Delta r) = \{f(\Delta r) - g(\Delta r)\} \frac{\Delta r_i \Delta r_j}{|\Delta \mathbf{r}|^2} + g(\Delta r) \delta_{ij} \quad (2-60)$$

where  $f(\Delta r)$  and  $g(\Delta r)$  are the longitudinal and transverse two-point correlation functions [61] and  $\delta_{ij}$  the Kronecker Delta. The required integral time  $T_L$  and the turbulent length scale of the SGS turbulence  $L_E$  were estimated with the turbulent kinetic energy and the dissipation rate, making use of approximations introduced by Lilly [62]:

$$T_L = 0.16 \frac{k_{SGS}}{\epsilon_{SGS}} \quad L_E = 3.0 \sigma_c T_L \quad (2-61)$$

$$k_{SGS} = \frac{\mu_{t,c}^2}{\rho_c^2 (0.094 \Delta)^2} \quad \epsilon_{SGS} = \frac{C_\epsilon k_{SGS}^{3/2}}{\Delta} \quad (2-62)$$

$$\sigma_c = \sqrt{\frac{2}{3} k_{SGS}} \quad (2-63)$$

in which the dissipation constant was selected as  $C_\epsilon = 0.7$  [63] and the SGS length scale is  $\Delta = (V_{CV})^{1/3}$  based on the volume of the local computational cell.

## 2.4 Solution algorithm

The numerical solution of the equations described above naturally need to be performed for both continuous and dispersed phases. The two-way coupling between them is given by the correspondent source terms, which can be momentum, SGS turbulence, chemical species or other appropriate variables. Once the relevant time-scales from the continuous (Eulerian) phase are usually much larger than the dispersed (Lagrangian) phase, the temporal solution of each individual phase can be conducted in a semi-unsteady approach [64]. This implies that the Eulerian time-step  $\Delta t_E$  can be different than the Lagrangian one  $\Delta t_L$ , applying the so-called coupling in key-times, so that a substantial computational effort can be spared. In this framework, the solution algorithm is divided in two parts or phases, as illustrated in the Figure 2-3. The first part consists of the Eulerian phase, by solving the governing equations for one time-step. This resulting flow information is “frozen” and used for the Lagrangian phase tracking. In the second part, all the present bubbles advance in time individually until they reach the Eulerian time. At this point, the resulting source terms from the dispersed phase are transferred back to the Eulerian phase, so that the solution loop starts again and the simulation continues, as seen in the Figure 2-3.

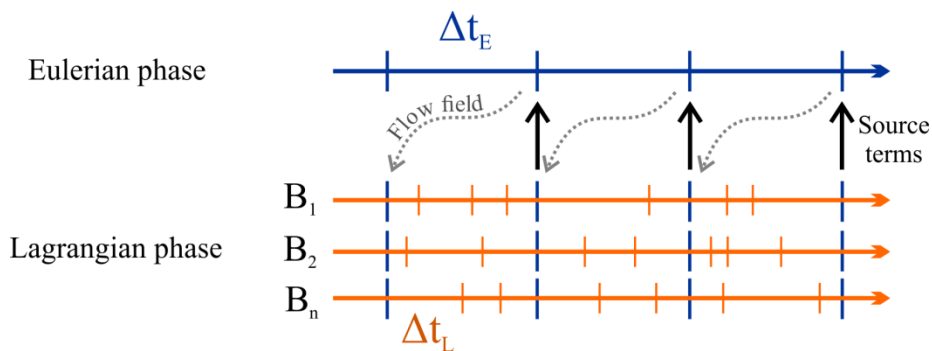


Figure 2-3: Schematic illustration from the two-way coupling algorithm.

The used pressure-velocity coupling method in the Eulerian inner loop was the PIMPLE [65], which is a combination from the well-known PISO and the SIMPLE/SIMPLEC algorithms. One advantage in using this method is to achieve a more stable solution in larger time-steps, when compared to PISO. In the cases presented in this work, three iterations of inner loops (PISO part) with non-orthogonal correction for each momentum prediction (SIMPLE part) were performed. The volume fraction equation (Eq.

(2-2)) was solved in three sub-cycles for each Eulerian time-step, in order to get a stable solution. The absolute tolerance for numerical convergence was set as  $10^{-7}$  and achieved around nine PIMPLE outer loops.

## 2.5 Oscillation Model

As concluded by Sommerfeld et al. [52], even with the consideration of SGS turbulent dispersion and bubble-induced turbulence is not possible to capture the oscillatory motion of bubbles with the point-particle Euler/Lagrange approach. In order to do so, an additional model which mimics bubble oscillations is required. This model extends the classical Lagrangian tracking approach for bubbles in a liquid, considering additional properties for bubbles, such as eccentricity and motion angle, and predicting them stochastically over time, yet based on experimental observations and statistical results. The objective here is not to resolve asymmetric shape deformations from bubble or liquid flow around the bubbles boundaries for capturing their oscillatory motion, but to mimic somehow the outcomes from these asymmetries through simple models designed for that purpose, avoiding high computational efforts. In this framework, a Langevin model is also used describing the development of the instantaneous bubble eccentricity through a combination of a correlated and a random part:

$$\chi^{n+1} = \bar{\chi} + (\chi^n - \bar{\chi}) R_\chi + \sigma_\chi \xi \sqrt{1 - R_\chi^2} \quad (2-64)$$

$$R_\chi = \exp\left(-\frac{\Delta t_L}{\tau_{osc}}\right) \quad (2-65)$$

where  $\bar{\chi}$  and  $\sigma_\chi$  are the mean bubble eccentricity and its correspondent RMS value, respectively, which require empirical correlations. In this study  $\bar{\chi}$  and  $\sigma_\chi$  were estimated in dependence of bubble size from measurements in a bubble column and a loop reactor [56], through the following fitting functions:

$$\bar{\chi}(d_B[m]) = \begin{cases} 1.0 & d_B < 0.001 \\ 1000d_B & 0.001 \leq d_B < 0.00175 \\ 133.333d_B + 1.51667 & 0.00175 \leq d_B < 0.0025 \\ -166.667d_B + 2.2667 & 0.0025 \leq d_B < 0.004 \\ 1.6 & 0.004 \leq d_B \end{cases} \quad (2-66)$$

$$\sigma_{\chi}(d_B[m]) = \begin{cases} 0.0 & d_B < 0.001 \\ 400d_B - 0.4 & 0.001 \leq d_B < 0.0015 \\ 141.6667d_B - 0.0125 & 0.0015 \leq d_B < 0.0027 \\ 0.37 & 0.0027 \leq d_B < 0.0031 \\ -44.4444d_B + 0.5077 & 0.0031 \leq d_B < 0.004 \\ 0.33 & 0.004 \leq d_B \end{cases} \quad (2-67)$$

There are many correlations in the Literature for the mean eccentricity (see Sommerfeld and Bröder [56]), but for the best of the authors knowledge, the correlation for standard deviation (Eq. (2-68)) is so far the only one. This equation was validated for mobile bubbles in flow with volume fraction up to 1.5%.

The bubbles were considered to be always oblate. Thus, for mathematical consistencies and model stability, an under limit function was applied to the eccentricity, making sure that the final value will be always greater than the unity, as follows:

$$\chi = \begin{cases} \chi & \text{for } \chi \geq 1 \\ 1 + |1 - \chi| & \text{for } \chi < 1 \end{cases} \quad (2-68)$$

Furthermore, a stochastic deviation of bubble from its path is also considered, similar to the eccentricity, in order to mimic the bubble dynamic motion. The deviation angle  $\delta$  is then applied to the instantaneous bubble velocity, as presented in the Figure 2-4 at the beginning of each tracking time step.

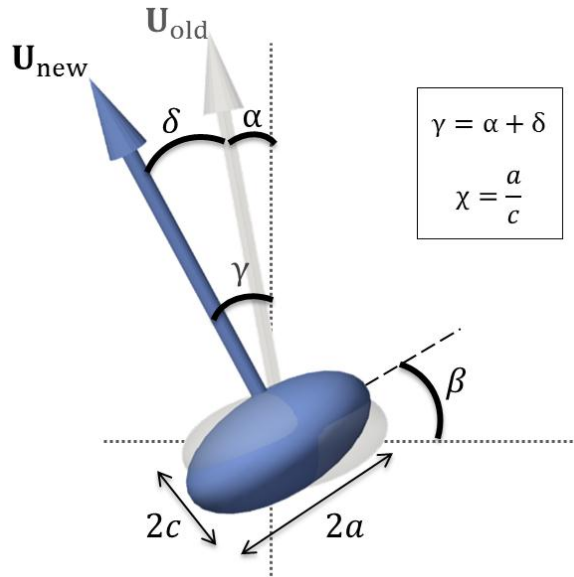


Figure 2-4: Schematic illustration of parameters and angles used for the bubble dynamics model.

Since the bubble moves in a three-dimensional way, the bubble motion angle is modified for each of the two horizontal Cartesian coordinates with respect to the vertical one, as follows:

$$\gamma_i^{n+1} = \alpha_i^n [1 + K_c (R_\gamma - 1)] + \sigma_\gamma \xi_i \sqrt{1 - R_\gamma^2} \quad (2-69)$$

$$R_\gamma = \exp\left(-\frac{\Delta t_L}{\tau_{osc}}\right) \quad (2-70)$$

where  $K_c$  is a correlation factor. In this manner, the bubble oscillatory motion would be purely random when  $K_c \rightarrow 0$ , or totally correlated in time when  $K_c \rightarrow 1$ . A full correlation in time ( $K_c = 1$ ) may prescribe the bubble paths too much and constraint the response to the acting forces. A pure stochastic modification ( $K_c = 0$ ), as proposed by Sommerfeld et al. [52], would overestimate bubble dispersion for long bubble residence times, though. In this framework, a successful balance between these two scenarios is achieved considering  $K_c = 0.5$ .



# 3 Results – Bubble motion

The contents of this section is focused on the hydrodynamics of bubble columns. Here, the model validation was then performed step-by-step, starting from single bubbles trajectories as basic tests and going further to bubble swarms. In order to explore the range of applicability from the proposed CFD model, a comparison with experimental data from the literature is conducted in different scenarios, varying bubble size distribution and column geometry.

## 3.1 Bubble Trajectories

In the following, with the purpose to verify the need and applicability of the oscillation model discussed in the previous section of this work, some test cases will be shown with regard to bubble trajectories, velocities and oscillation parameters.

### 3.1.1 Test Cases descriptions and setup

The physical situation consists of a laboratory bubble column, based on experiments conducted by Sommerfeld and Brüder [56]. The cylinder is filled to 650 mm with water and has a diameter of 140 mm, as seen in the Figure 3-1. The gas is inflated into the column within 50 capillaries at 20 mm above the bottom in a volumetric flow rate of 160L/h. The resulting mean bubble diameter is 2.55 mm within a range from 0.5 mm up to 5.0 mm. The numerical grid used for this domain consists of 23,040 control volumes in total, in which 18,944 of them remain under the initial water level, as seen in the Figure 3-1. A set of 9 individual bubble trajectories were tracked during 3s in the quasi-steady state from the resulting flow. In order to emphasize the relevance and the parameters of the oscillation

model proposed in this work, four simulation setups were evaluated, whose descriptions are given in the Table 3-1. In all these cases, all the relevant forces described before were considered as well a two-way coupling, SGS turbulent dispersion model and bubble-induced turbulence.

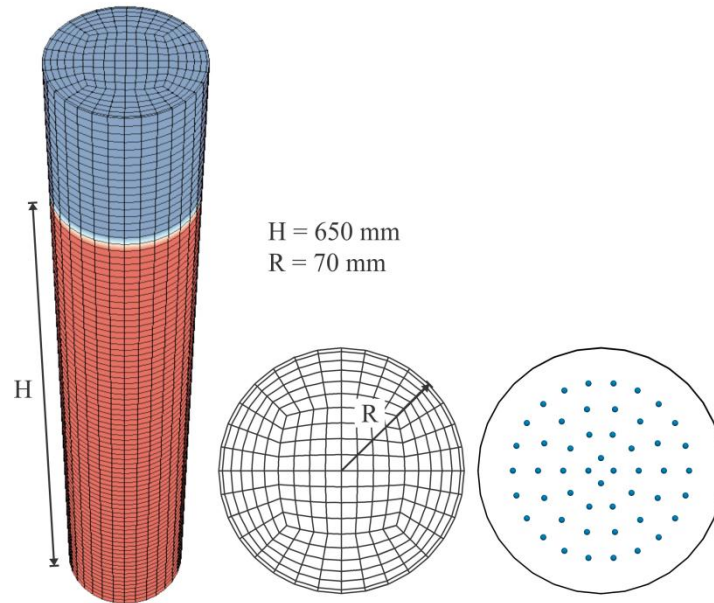


Figure 3-1: Numerical grid used in the simulations. 23,040 volumes in total (18,944 for the liquid part), 256 volumes per cross section and 90 along the height.

Table 3-1: Cases description for bubble trajectories tests.  $Q_g=160$  L/h

	All Forces	2-way coupling	TDM	BIT	$d_B$ [mm]	$\frac{d_B}{\Delta x}$	Oscillation Model
Test 1	x	x	x	x	[2.0, 4.0]	[0.24, 0.48]	
Test 2	x	x	x	x	[2.0, 4.0]	[0.24, 0.48]	$K_c = 0.0$
Test 3	x	x	x	x	[2.0, 4.0]	[0.24, 0.48]	$K_c = 0.5$
Test 4	x	x	x	x	[2.0, 4.0]	[0.24, 0.48]	$K_c = 1.0$

The 9 bubbles with equal diameters were tracked in the quasi-steady flow from the bottom until they escape the domain by “touching” the free surface ( $\alpha_c = 0.5$ ). The initial vertical bubble velocity was assumed to be 0.01 m/s without any random component. The lateral injection velocities were assumed to be zero. Since the bubbles physically start from rest at the needle outlet, the Basset force contribution was assumed to be zero upon injection. All boundaries were set as non-slip wall condition for the continuous phase and as rebound



for the bubbles (Eq. (2-52)), except the top boundary, which is open to the atmospheric pressure. The used Eulerian time-step was constant and equal to 5 ms.

### 3.1.2 Results and discussion

The resulting trajectories of each test are shown in the Figure 3-2. Note in the Test 1 that, even with the consideration of all forces, present effects of SGS turbulent dispersion and bubble-induced turbulence, the bubbles trajectories are very smooth. However, it is known that such behaviour is not observed experimentally for this range of bubble size, e.g., works from Lunde and Perkins [45], Jeong and Park [40] and Sommerfeld et al. [52]. The inclusion of oscillation model (Tests 2, 3 and 4), in which a stochastic deviation of bubble motion is applied, produced a higher lateral dispersion, notably in the Test 2. However, these trajectories do not form a clear “zig-zag” or helical form, since the model is not based in sinusoidal functions. Nevertheless, such details are not of a great importance in a bubble swarm, and in essence, the input parameters for frequencies and amplitudes are supported by experimental data.

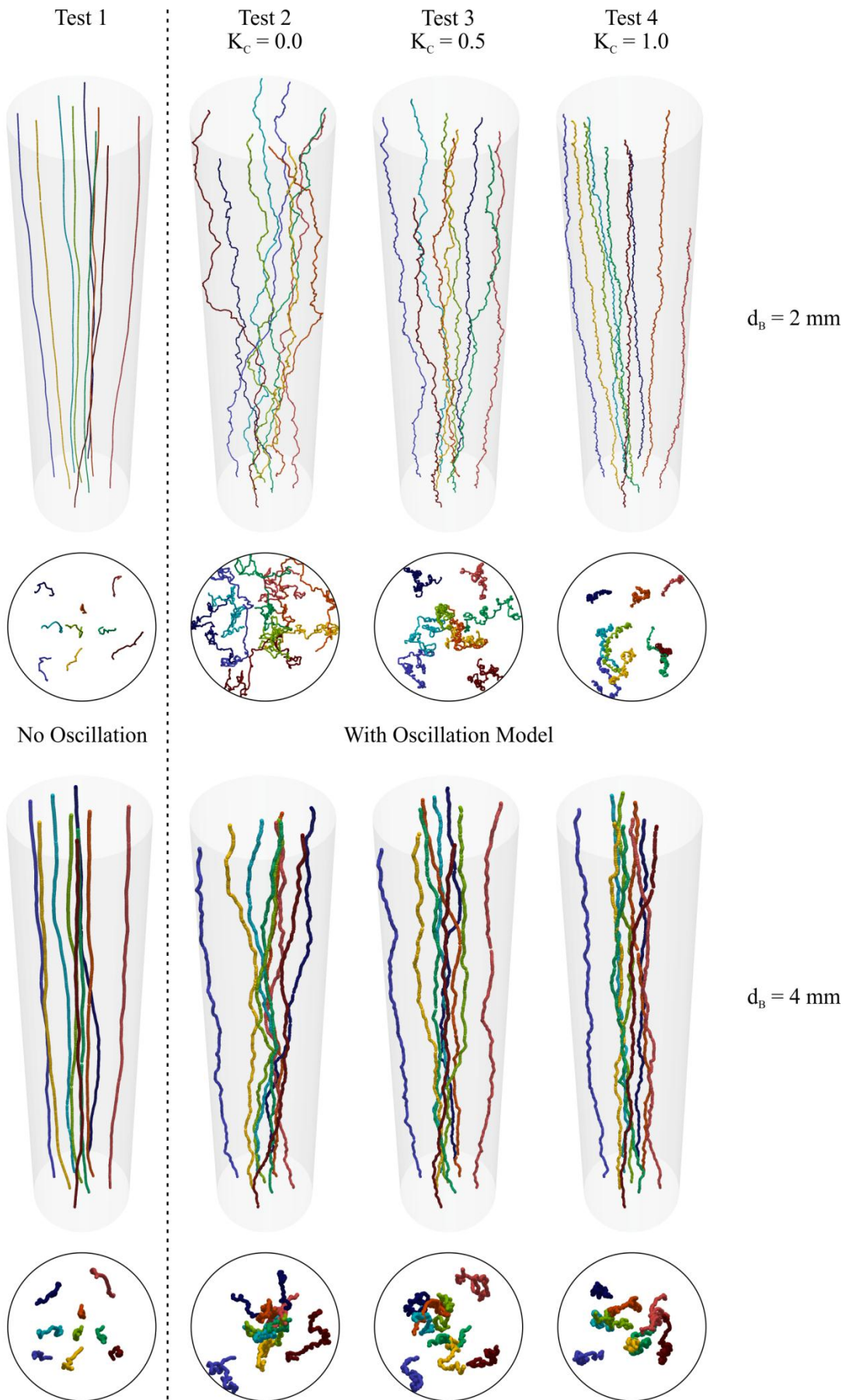


Figure 3-2: Nine bubble trajectories extracted from the Tests 1 to 4, tracked during 3s after 500s of simulation; All forces, TDM and BIT models included;  $Q_g=160 \text{ L/h}$ ,  $\alpha_{g,\text{mean}} \cong 1.2\%$ .

The resulting PDFs of bubble motion angle imposed by the oscillation model in Cases 2-4 are compared with experimental data in the Figure 3-3a. Note that using any values of the correlation constant  $K_c$ , the same distribution of  $\gamma$  is achieved. However, the average angle deviation  $\delta^{i+1}$  resulting from these same cases is correlated with the current motion angle  $\gamma^i$  in the Figure 3-3b. Note that the uncorrelated form of Eq. (2-69) ( $K_c=0.0$ ) produce equal probabilities of a positive or negative deviation. On the other hand, the full correlated form ( $K_c=1.0$ ) yield a mostly positive deviation when the current motion angle is negative and vice-versa. Beside this fact, high deviations are predicted for motion angles higher than  $45^\circ$ , constraining the bubble trajectories too much. In this framework, a better choice is to use  $K_c=0.5$ , where the motion deviation remains correlated, but smoother values are achieved.

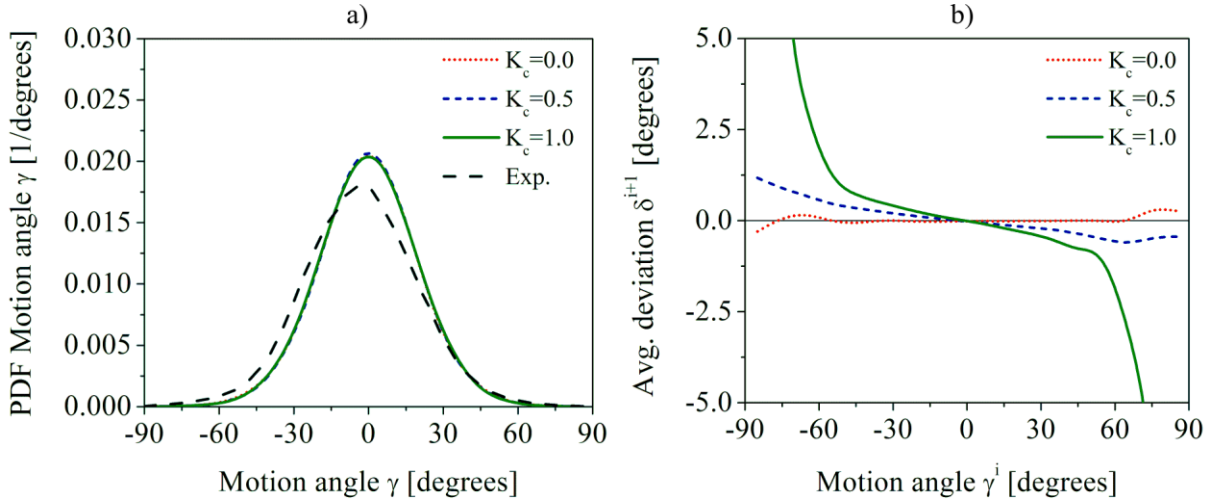


Figure 3-3: a) Resulting PDF of motion angle from cases 2-4,  $d_B = 2\text{mm}$ .

Experiments: Sommerfeld and Bröder [56],  $d_B = 0.5\sim 5\text{mm}$ .

b) Average angle deviation versus current motion angle from cases 2-4,  $d_B = 2\text{mm}$ .

The effect of the correlation constant is also noticed by applying a Fast-Fourier-Transform (FFT) in the temporal series from the resulting motion angle, as seen in the Figure 3-4. Note when  $K_c=1.0$  that although a stochastic prediction of motion deviation, a clear oscillation frequency around 13Hz is obtained, which agrees with values observed by Lunde and Perkins [45] for the vortex shedding. However, when the correlation constant is below the unity, the FFT does not produce anymore a distinct peak, and the values become more random as  $K_c$  approximates to null. The weak point on using  $K_c=1.0$  is that the strong angle deviations are imposed by the model, as seen in the Figure 3-3b. In this manner, in all the following simulations from this work, the correlation constant was assumed  $K_c=0.5$ , in which a balance between correlation and lateral dispersion is achieved.

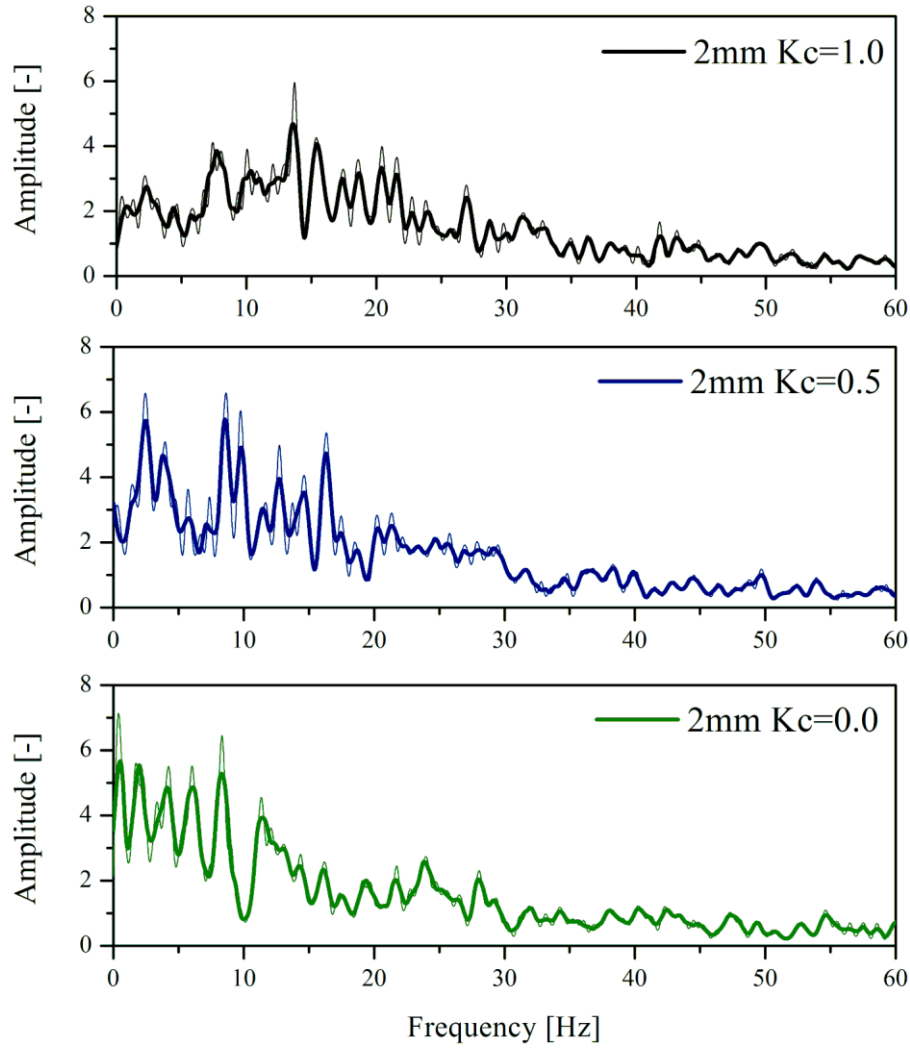


Figure 3-4: FFT of bubble motion angle from test cases 2-4.  $d_B = 2$  mm.  
Thin line: original FFT. Thick line: smoothed results.

## 3.2 Bubble Swarms – Study Case I

After testing the model for single bubbles, the experimental results from Sommerfeld and Bröder [56] were taken as study case for bubble swarms. Their data offer a good opportunity for model validation, not only with regard to bubble and liquid averaged velocities but also to their Root Mean Square (RMS) values. Additionally, probability density functions (PDF) for bubble motion angle and eccentricity are also available, which fully supports the input parameters required in the oscillation model proposed in this work. In the following, the setup for the cases and description of geometry, numerical mesh and operational conditions will be shown.

### 3.2.1 Cases descriptions and setup

The physical situation consists in the circular bubble column ( $\varnothing 140\text{mm}$ ) used in the single bubble cases (Figure 3-1). In their experiments, the same air flow rate ( $Q_g = 160 \text{ L/h}$ ) was introduced in the system through two different sets of 50 needles, reaching different bubble size distributions (namely the cases “A2” and “B1” from the reference). These needles for the bubble injection extend for 20 mm above the column bottom and are distributed in an area equivalent to a circle with 100mm of diameter. The velocity profiles from the liquid and gas phases were measured in five cross-sections along the column height (75, 200, 325, 450 and 575mm). As well as for the single bubbles, a set of cases with different model configurations were conducted, in order to assess step-by-step the effect and influence of each consideration. The case descriptions and the bubble size distribution are shown in the Table 3-2 and in the Figure 3-10, respectively.

Table 3-2: Cases description for different simulations.  $Q_g=160$  L/h.

	Ref.	All Forces*	Drag	Lift	2-way coupling	TDM	BIT	OM	$\overline{d_B}$ [mm]	$\frac{\overline{d_B}}{\Delta x}$	$\frac{d_{B,max}}{\Delta x}$
Case 1	A2	x	D1	L1	x				2.55	0.31	0.54
Case 2	A2	x	D1	L1	x	x			2.55	0.31	0.54
Case 3	A2	x	D1	L1	x	x	x		2.55	0.31	0.54
Case 4	A2	x	D1	L2	x	x	x		2.55	0.31	0.54
Case 5	A2	x	D2	L1	x	x	x	x	2.55	0.31	0.54
Case 6	A2	x	D2	L2	x	x	x	x	2.55	0.31	0.54
Case 7	A2	no Basset	D2	L2	x	x	x	x	2.55	0.31	0.54
Case 8	B1	x	D1	L2	x	x	x		3.31	0.40	0.60
Case 9	B1	x	D2	L2	x	x	x	x	3.31	0.40	0.60

D1  $\equiv C_D$  – Eq. (2-15); D2  $\equiv C_{D,\chi}$  – Eq. (2-21); L1  $\equiv$  Eq. (2-31); L2  $\equiv$  Eq. (2-39)

\*Drag, lift, added mass, fluid inertia, wall, Basset, gravity and buoyancy.

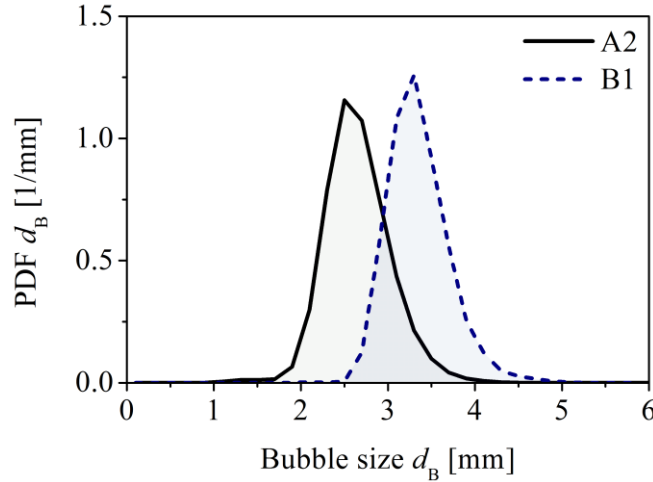


Figure 3-5: Bubble size distribution from reference cases A2 and B1.

Source: adapted from Sommerfeld and Bröder [56].

Note that, in all cases, the resulting ratio between the mean bubble diameter and element length is below the limit proposed by Milleli [66] ( $d_B/\Delta x \leq 0.67$ ) for LES-Euler/Lagrange calculations. All boundaries were set as non-slip wall condition for the continuous phase and as rebound for the bubbles (Eq. (2-52)), except the top boundary, which

is open to the atmospheric pressure. The bubbles escape the domain when they touch the free surface at  $\alpha_g=0.5$ . The Eulerian time-step was constant and equal to  $\Delta t_E = 5$  ms. The air flow rate for reference cases A2 and B1 is the same, however, the different size distributions result in bubble injection frequencies of 4,352 and 2,180 bubbles per second, respectively.

### *Statistics Sampling*

Since the comparison with the experimental data is made in terms of average and RMS values, a proper statistics procedure should be executed. First of all, the simulation is conducted for a while for flow stabilization, inasmuch as a *pseudo*-steady state is achieved. After that, statistics is numerically acquired until the average value reaches a stagnant value. Since the liquid is a continuum phase, a simple time-averaging can be performed in the proper frequency of calculations ( $f_{a,liq} = 1/\Delta t_E = 200$  Hz). For the dispersed/discrete phase, on the other hand, the bubble properties need to be mapped and imported to the cell level. Once the number of available samples per cell per time-step is not constant in this case, the averaged values derive from the total number of accumulated samples in each individual cell during the whole time of simulation, e.g.,  $\overline{u_{B,m}} = \sum u_{B,m} / N_m$ , where  $m$  represents the local mesh cell and  $N_m$  the number of samples in the cell  $m$ . In this case, slower bubbles have a larger residence time, producing more samples in a certain evaluation time than the faster ones. In order to avoid this issue of sampling bias or self-correlated data, the time-interval between two samples should be large enough, guaranteeing that a bubble is not counted twice in a same mesh cell. In this manner, the acquisition frequency was arbitrary chosen as  $f_{a,bub} = f_{a,liq}/10 = 20$  Hz.

For a first analysis, the integral volume fraction of bubbles (gas hold-up) over time is showed in the Figure 3-6. Note that close to 17s of simulation, the flow seems to reach a quasi-steady state, in which the statistics sampling could be apparently started.

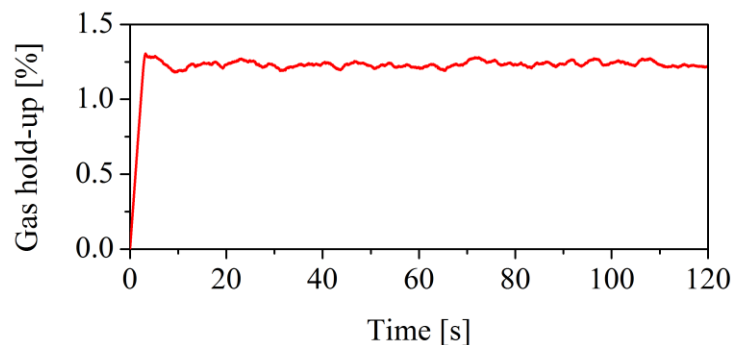


Figure 3-6: Example of integral volume fraction of bubbles over time.  
Case 5 (full model – L1),  $Q_g=160$  L/h,  $\overline{d_b} = 2.55$  mm.

Nevertheless, local variables, such as instantaneous fluid vertical and horizontal velocities, were also sampled over time and in different heights on the central axis of the column, as seen in the Figure 3-7a and c. Moreover, the evolution of the average values based on these same data is exposed in the Figure 3-7b and d.

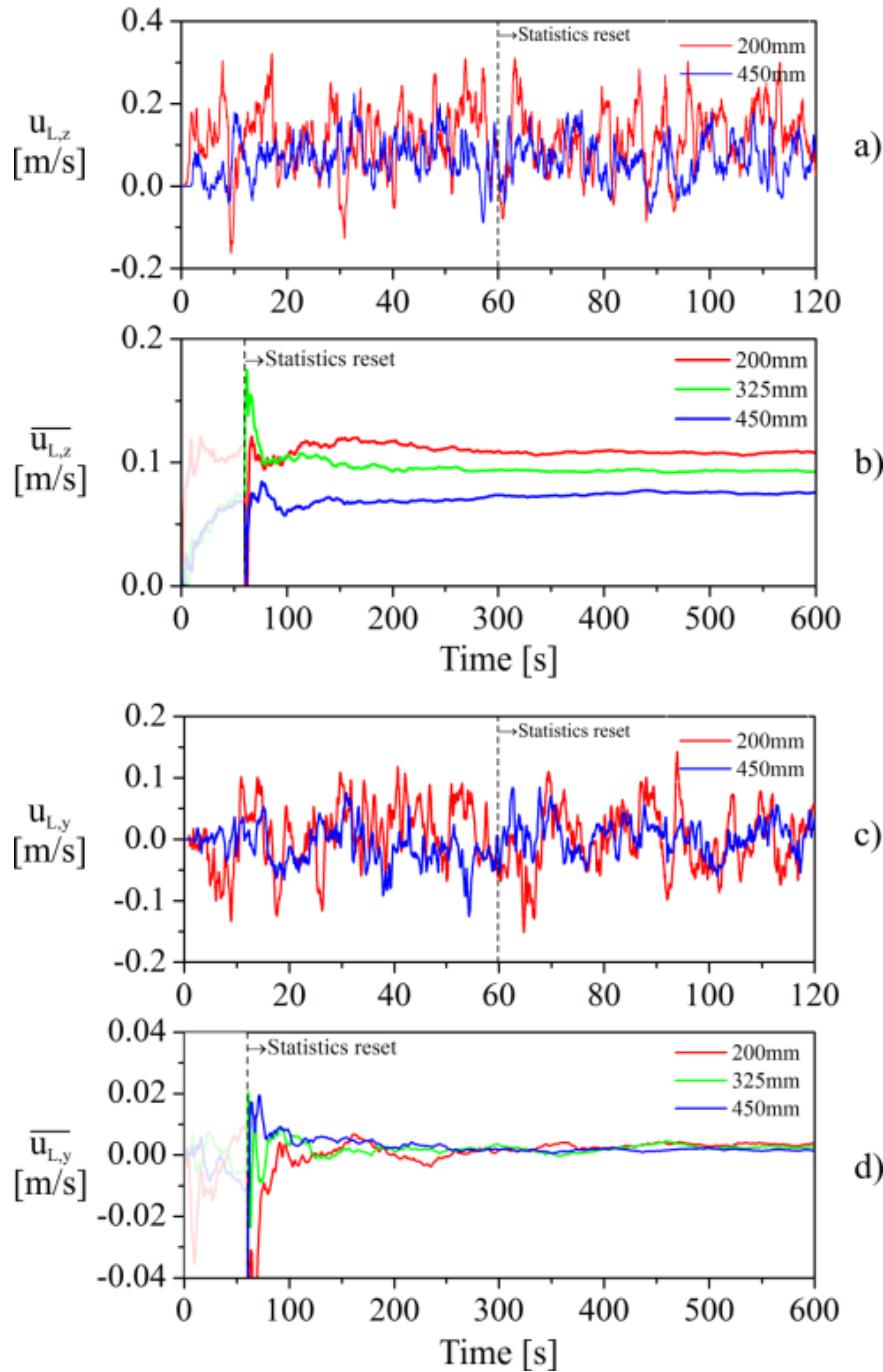


Figure 3-7: Liquid velocities along time in different heights from the bubble column:  
a) instantaneous in vertical direction; b) evolution of mean value (vertical);  
c) instantaneous in horizontal direction; d) evolution of mean value (horizontal).  
Case 5 (full model – L1),  $Q_g=160$  L/h,  $\overline{d}_b = 2.55$  mm.



Note in the Figure 3-7c that the horizontal liquid velocity for the axial position 200mm reaches a quasi-steady state at 20s, similar to the total gas hold-up. However, the flow at a higher position (450mm) in this time is still in development. Based on these results it can be assumed, that a stable flow is reached for sure at 60s of simulation and after this time, the statistics is reset. Note in the Figure 3-7b and d, that at the beginning of the statistics sampling, the average values strongly change due to the low number of samples. As larger evaluation times are reached, these averages tend to an almost constant value, since enough samples are available. For the axial position and vertical direction (Figure 3-7b), the average velocities are expected to be positive (core flow). For the horizontal direction (Figure 3-7d), on the other hand, the average velocities tend to a null value (symmetry).

For a better visualization of this matter, instantaneous colour fields in terms of vertical and horizontal velocities are shown in the Figure 3-8. Note that a core flow originated from the bubble plume remains stable until 15s. After this point, asymmetries close to the aerator start to grow and large flow structures move from the bottom to the top of the column. Moreover, changes in the lateral velocity magnitude (Figure 3-8b) in the upper part of the column are remarkable up to 40s. This denotes that following only the gas hold-up is not trustworthy and local variables should be also highlighted. The thin white line over the core flow represent the free surface, where  $\alpha_L = 0.5$ , thus, the domain above this line is the continuous gas phase and has initially a height of 650mm.

Finally, the statistics sampling is restarted at 60s of simulation, being sure that a pseudo-steady state has been reached. Afterwards, the averaged values seem to change until reach an almost constant value around 400s, as seen in the Figure 3-7. From this time up to 600s, the averaged values still present small oscillations, yet not of great importance ( $\mathcal{O}(10^{-2})$ ). Since a very similar behaviour was observed in all the other cases, a standard procedure was conducted by sampling statistics from 60 to 500 seconds of simulation. The numerical solution for each case was made in parallel (8 cores – 3.0 GHz) and completed in less than two days.

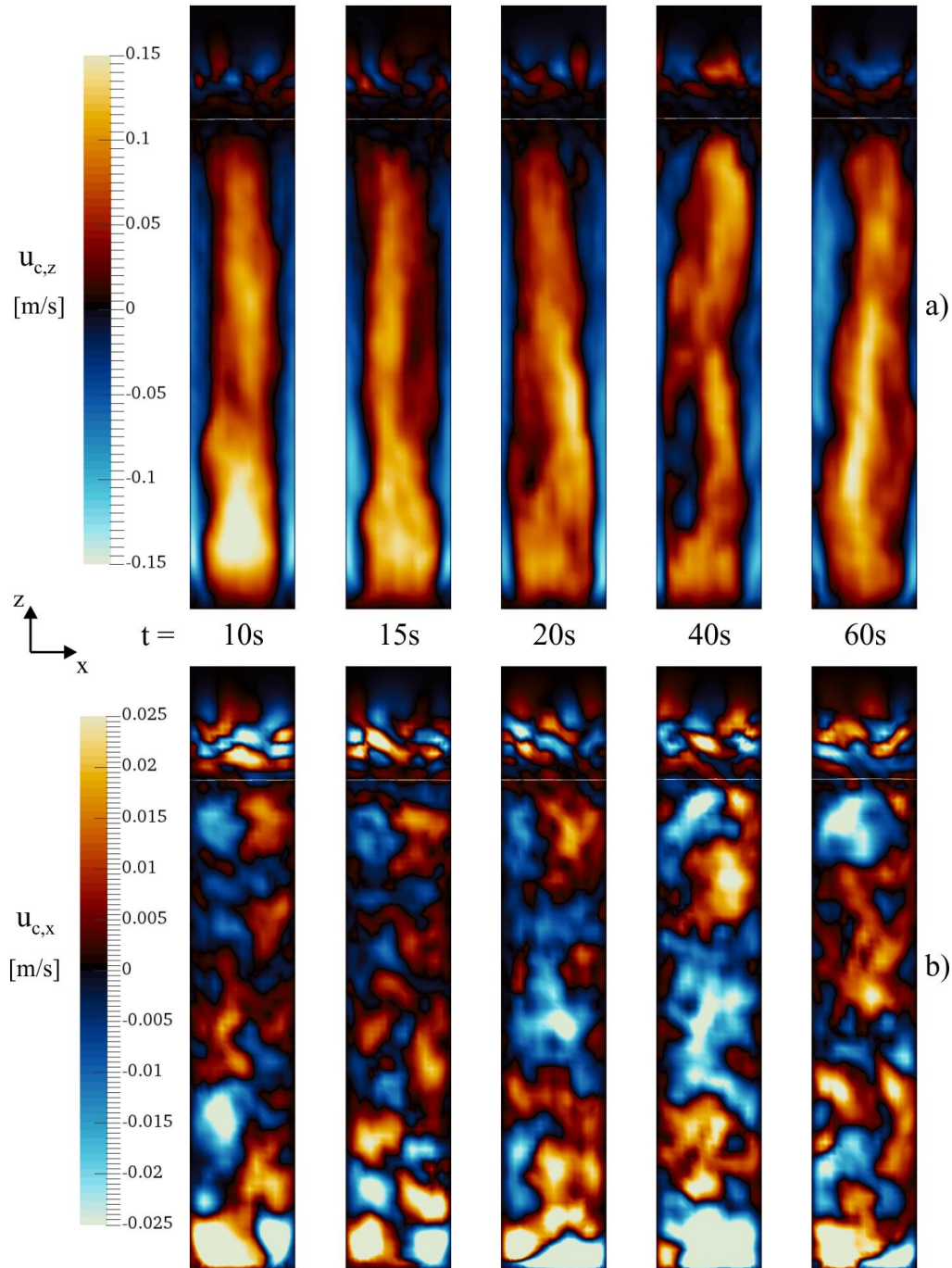


Figure 3-8: Colour fields of instantaneous continuous phase velocity: a) vertical; b) horizontal. Case 5 (full model – L1),  $Q_g=160$  L/h,  $\bar{d}_b = 2.55$  mm.

### 3.2.2 Results and discussion

As already mentioned, a set of numerical cases for bubble swarms was conducted with different model configurations. To present all this gathered data would be tedious, insomuch as some models do not affect the results significantly. Thus, only the relevant outcomes will be highlighted in the following.

The Cases 2 and 3 account, additionally to the case 1, for turbulent dispersion and bubble-induced turbulence on the sub-grid scale, respectively. The resulting bubble and liquid velocity profiles from Cases 1 and 3 are shown in the Figure 3-9. Here, average and RMS values of velocity in the vertical and horizontal directions are compared with experimental data [56]. As seen in the Figure 3-9a, the bubble rise velocity is underestimated for both the cases. Another fact is that the bubble velocity fluctuations in the horizontal direction are experimentally higher than in the vertical one, which was not captured by the model. Moreover, the modelling improvement through consideration of TDM and BIT models (Case 3) did not reflect a significant change in the bubble velocities profiles.

With regard to the liquid phase (Figure 3-9b), on the other hand, a considerable reduction of the velocity RMS values on the resolved scale from Case 1 to Case 3 is observed. This effect may be the outcome from this BIT modelling for the LES method [19,15] used here, in which the influence of bubbles is simply modelled through the enhancement of effective viscosity. Since the numerical grid is larger than the bubble size, and if this BIT model acts only by increasing the SGS viscosity, an enhancement of liquid velocity fluctuations on the resolved scales would never be achieved. As a consequence, the diffusion term of the momentum equation is higher and fluctuations in the resolved scales are smoothed.

The resulting PDFs of fluctuating liquid velocity seen by the bubble (TDM) and the SGS integral time are shown in the Figure 3-10. The Case 2, in which only the TDM is considered, predicts isotropic liquid fluctuations up to 0.05m/s and a mean turbulence integral time of 139ms. However, the influence of bubble motion on the SGS turbulence (Case 3) reveals a different scenario, in which the velocity fluctuations spread to magnitudes around 0.07 m/s (40% increment), indeed. Moreover, a reduction from the mean integral time to the half is observed, as expected from Eq. (2-62). Although the mean value for  $T_L$  in this case is 69 ms, local values are found down to 10 ms. Such small values are taken into account in the bubble tracking, which can limit the size of the Lagrangian time-step (Eq. (2-54)) in relation to the Eulerian time-step (in this case,  $\Delta t_E = 5\text{ms}$ ).

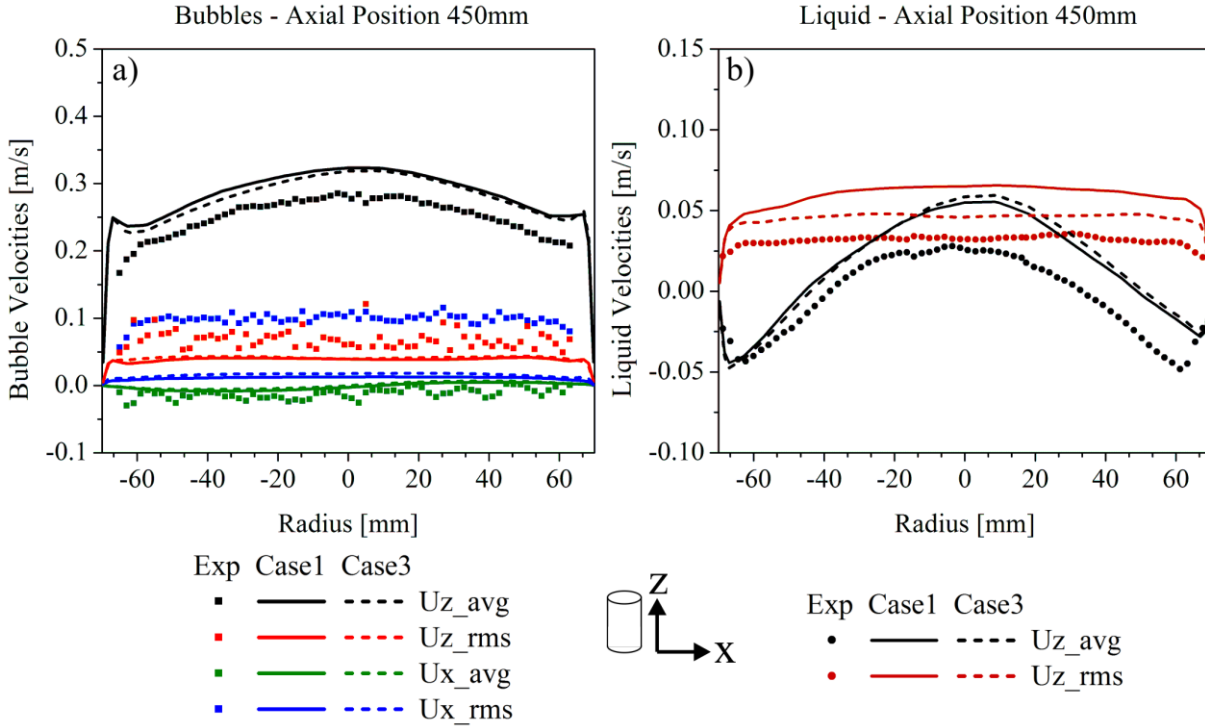


Figure 3-9: Comparison of averaged velocities and RMS values of fluctuations (resolved scale) with experimental data [56]: a) Bubbles, b) Liquid,  $Q_g=160$  L/h,  $\bar{d}_b = 2.55$  mm. Case 1: All forces(D1,L1), no TDM, no BIT, Case 3: All forces(D1,L1) + TDM + BIT.

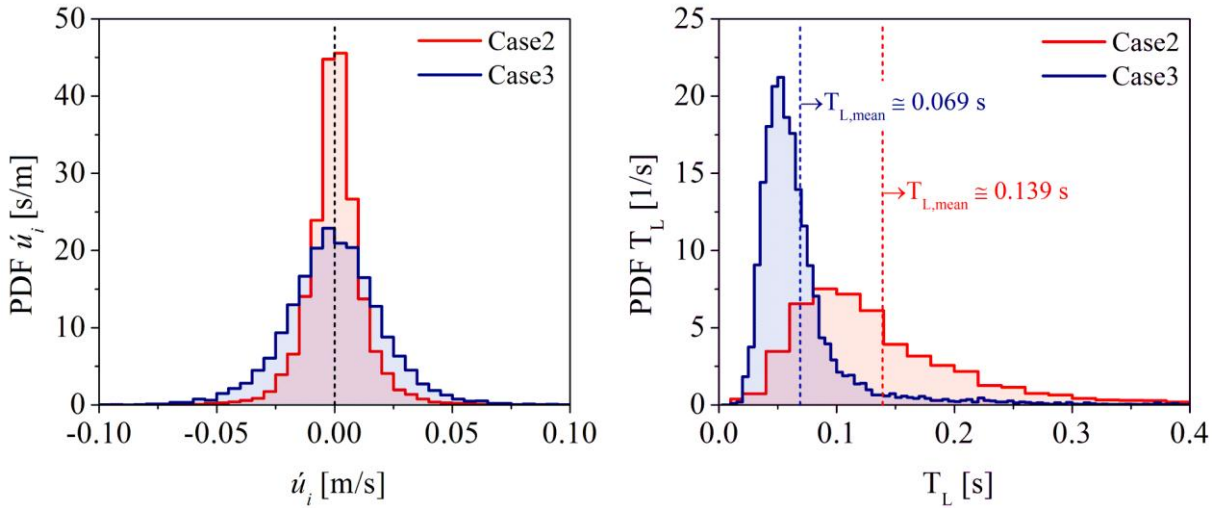


Figure 3-10: Comparison of resulting PDFs for the cases, regard to the SGS integral time and fluid fluctuating velocities seen by the bubble.  $T_{L,mean} \cong 0.139$  and  $0.069$  s.  $Q_g=160$  L/h,  $\bar{d}_b = 2.55$  mm. Case 2: All forces(D1,L1) + TDM, Case 3: All forces(D1,L1) + TDM + BIT.

A preliminary summary of the cases with respect to fluctuating energies of continuous is presented in the Figure 3-11. Here, area-averaged values of fluctuating energy  $k_{av}$  in different cross-sections of the column were obtained, based in the assumption that the horizontal components of the fluctuating velocity are equal, as described by Sommerfeld and Bröder [11]:

$$k_{av} = \frac{1}{A} \sum_{i=1}^n 0.5 \left( 2\overline{u'^2} + \overline{w'^2} \right)_i A_i \quad (3-1)$$

$$A_i = \frac{\pi}{2} (r_2^2 - r_1^2) \quad (3-2)$$

where  $u'$  and  $w'$  are the RMS values of liquid velocity fluctuations in the horizontal and vertical directions, respectively.  $A_i$  is the annular area by rotating the measurement points 180 degrees around the central column axis.  $r_1$  and  $r_2$  are the inner and outer radii of the annular area, respectively.

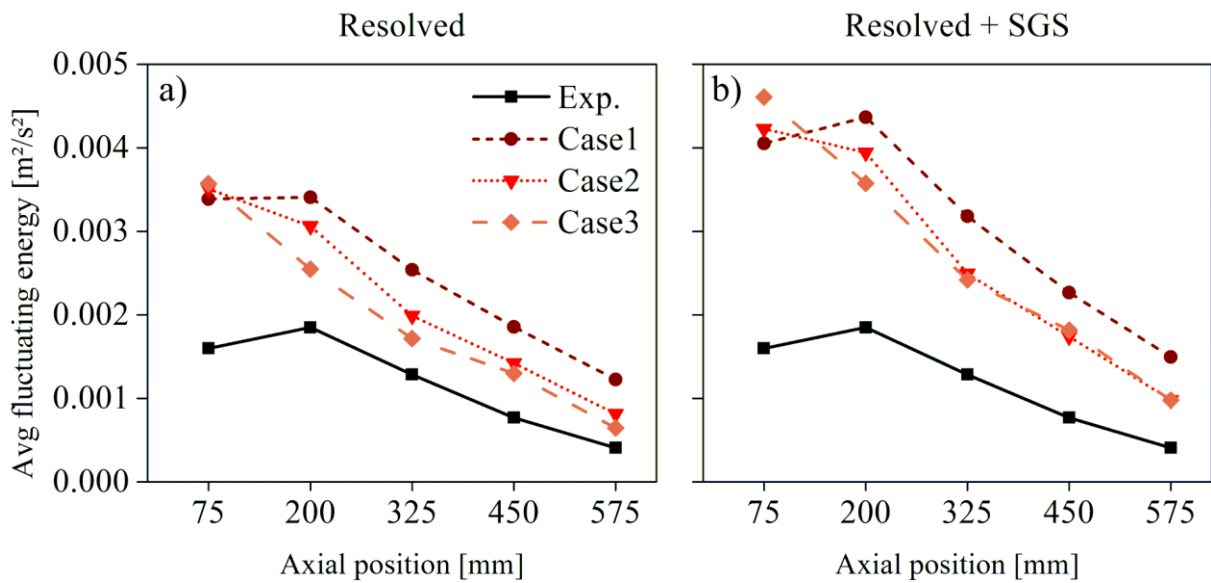


Figure 3-11: Fluctuating energies of the liquid phase:

a) Resolved scale; b) Resolved + Sub-grid scale.

Experiments: Sommerfeld & Bröder [56]. Case 1: All forces(D1,L1),  
Case 2: All forces(D1,L1) + TDM, Case 3: All forces(D1,L1) + TDM + BIT.

As seen in the Figure 3-11a, the consideration of TDM in the Case 2 revealed a reduction of liquid velocity fluctuations. This effect is exclusively caused by the momentum coupling between the phases, in which higher bubble dispersion is expected in the Case 2 compared to the Case 1. The inclusion of BIT (Case 3) reflects a further reduction of fluctuations in the resolved scales. However, the turbulence coupling through enhancement of SGS viscosity gives the aforementioned counterbalance, in which the total fluctuating energy (resolved and unresolved scales) from Cases 2 and 3 are equivalent, as seen in the Figure 3-11b.

Unfortunately, even considering all relevant forces (inclusive Basset), SGS turbulent dispersion and bubble-induced turbulence, was not possible to capture the lateral velocity

fluctuations using “point-mass” approximation. In order to do so, an additional model which mimics bubble oscillations was required. According to the Table 3-2, this model setup corresponds to the Case 5 and the results obtained for this case are shown in the Figure 3-12.

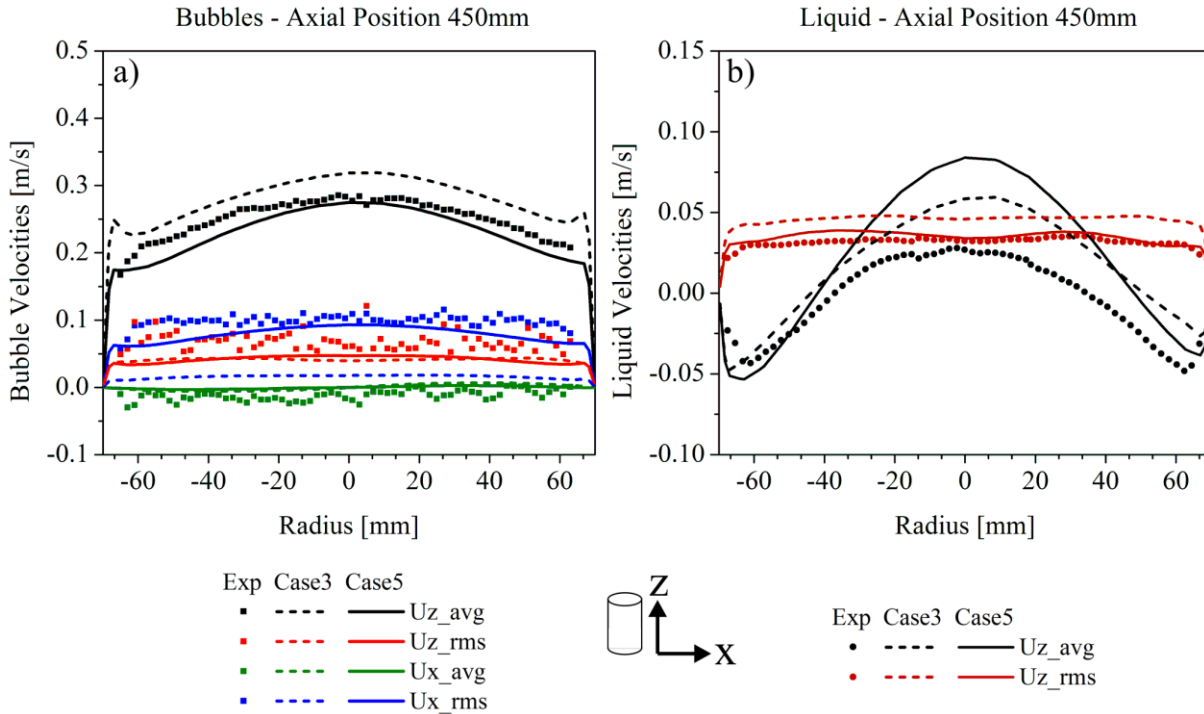


Figure 3-12: Comparison of averaged velocities and RMS values of fluctuations (resolved scale) with experimental data [56]: a) Bubbles; b) Liquid,  $Q_g=160$  L/h,  $\bar{d}_b = 2.55$  mm, Case 3: No oscillation (D1,L1), Case 5: With oscillation (D2,L1).

Expectedly, the inclusion of bubble dynamics yielded a significant impact on the results. First, a reduction of the average bubble rise velocity is noticed. Additionally, since the oscillation model promotes bubble lateral dispersion, as seen before for the cases with single bubbles, the velocity fluctuations in the horizontal direction are now greater than in the vertical one. Consequently, the velocity peaks at the vicinity of the wall almost disappear, inasmuch as the bubbles neither rise straight nor accumulate in this region anymore. Such differences in the results are in agreement with the experimental observations, as seen in the Figure 3-12a.

Once the average bubble rise velocity was decreased, the gas volume fraction is naturally increased due to longer residence times. Subsequently, as seen in the Figure 3-12b, a more intense upflow for the liquid phase in the core region is evidenced, as well as a stronger downflow at the wall. Although higher magnitudes of average liquid velocity were revealed in the Case 5 (Figure 3-12b), lower RMS values of velocity fluctuations in the resolved scales were found. The reason for this may be a better distribution of bubbles in the domain due to

the oscillation model. In order to expose this behaviour, instantaneous images with regard to the discrete phase from Cases 3 and 5 are shown in the Figure 3-13.

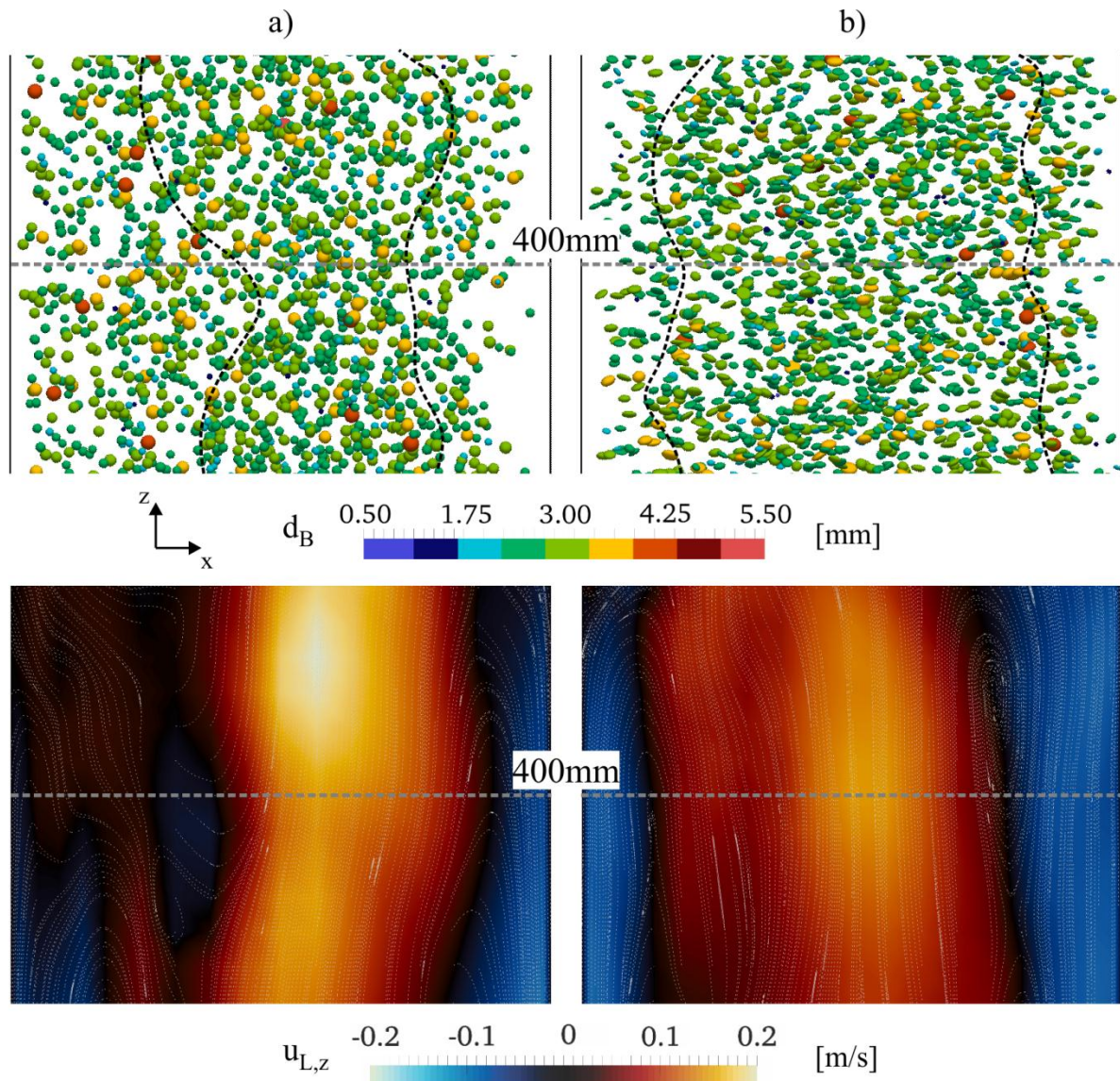


Figure 3-13: Numerical visualization of the discrete phase and vertical velocity of continuous phase for: a) Case 3, b) Case 5,  $t = 500\text{s}$ , Axial position: 400mm,  $Q_g = 160\text{ L/h}$ ,  $\bar{d}_b = 2.55\text{ mm}$ , Case 3: No oscillation (D1,L1), Case 5: With oscillation (D2,L1).

Note in the Figure 3-13a (Case 3) that the bubbles are not evenly distributed in the column, in which a dense swarm is concentrated in a narrow core region, marked in the figure between dashed lines. This condition is reflected in the instantaneous liquid velocity, where a similar pattern is found (red-yellow colours). In the Case 5, on the other hand, the bubble plume is clearly wider and the core flow is apparently more stable. After all, this stability results in lower RMS values of liquid velocity fluctuations.

Despite use of “point-particles” approximation in the calculations, the numerical visualization in the Figure 3-13 was possible, since the bubbles properties are stored individually, e.g., diameter, position, eccentricity, motion angle. Once the drag model used in the Case 5 depends on the instantaneous bubble eccentricity (Eq. (2-21)), differently than from Case 3, where only the equivalent bubble diameter is considered (Eq. (2-15)), a distinct scatter for the drag coefficient is naturally expected. This data are shown in the Figure 3-14, as follows:

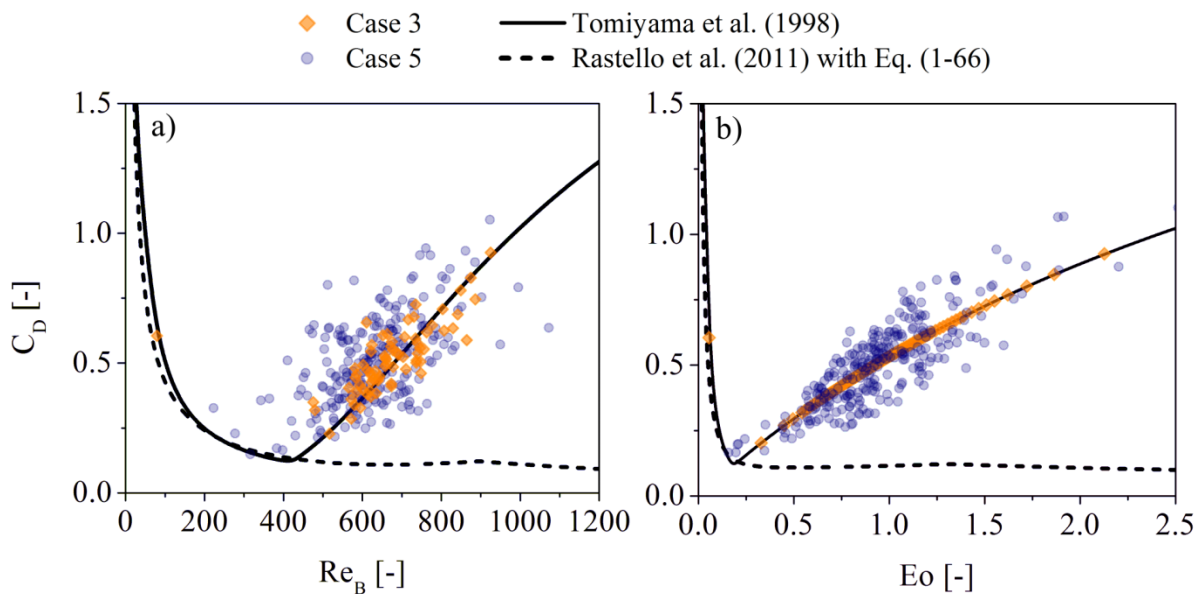


Figure 3-14: Resulting drag coefficients from Cases 3 and 5 versus:  
a) Reynolds number, b) Eötvös number,  $Q_g=160$  L/h,  $\bar{d}_b = 2.55$  mm.  
Case 3: No oscillation (D1,L1), Case 5: With oscillation (D2,L1).

In order to produce the graphs in the Figure 3-14, some hundreds of bubble samples were taken from various stored times of simulation. Subsequently, the drag coefficients were plotted versus the correspondent Reynolds and Eötvös numbers. As seen in the Figure 3-14b, the majority of bubbles from the present cases lie in the coefficient range dominated by the Eötvös number. As consequence, the resultants drag coefficients from Case 3 follow strictly the correlation proposed by Tomiyama et al. [24], since no bubble dynamics is considered (D1). As aforementioned, the information of an expected bubble eccentricity is already implicit in the fitted correlation, which predicts successfully average values of drag coefficients based in a large amount of experimental data. The second drag approach (D2), used in the Case 5, on the other hand, proposes deviations around the average value making use of the modified Eötvös number, dependent on the major bubble axis. After all, the proposed modification “D2” does not predict a different mean value, as seen in the Figure



3-14b, yet improves the determination of the drag coefficient according the instantaneous bubble eccentricity.

The computation of bubble eccentricity is performed in this work stochastically. However, the use of a proper correlation for its mean value and standard deviation is essential. For purpose of model validation with this study case [56], there is no better way than comparing the resulting numerical data with the experimental one, which was used to produce the correlation (Eqs. (2-66) and (2-67)). In this framework, the resulting PDF of eccentricity obtained from Case 5 is compared with experiments in the Figure 3-15. Here, only bubbles with equivalent diameter of 2.5 mm ( $\pm 0.1$ ) were sampled from the whole data of Case 5.

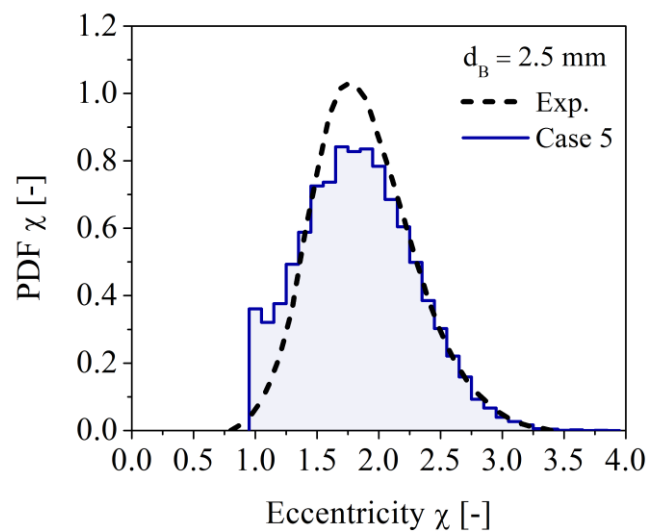


Figure 3-15: Comparison of numerical and experimental [56] PDF of bubble eccentricity,  $Q_g=160$  L/h,  $\bar{d}_b = 2.55$  mm, Case 5: With oscillation model (D2,L1).

Note that, although the input parameters for mean and RMS values come from the experimental observations, the resulting PDF of bubble eccentricity can slightly deviate from the measurements. Inasmuch as the Langevin equation will produce a normal distribution, and the experiments do not show this exact behaviour, as seen in the Figure 3-15, such differences are justifiable. Moreover, the light peak existent at  $\chi = 1.0$  is derivate from the limit imposed in the model (Eq. (2-68)), in order to avoid inconsistencies ( $\chi \geq 1.0$ ). In consideration of the desired model simplicity, the produced values of bubble eccentricity are satisfactory and sufficient for the purpose of the present work.

Following the old eccentricity correlation suggested by Wellek et al. [67], Ziegenhein et al. [35,68] proposed recently new fitting parameters for clean bubbles in the wobbling regime in air-water systems. Once the flow conditions of the present study case [56] fit inside the range of application from their correlation, a fair comparison is shown in the Figure 3-16.

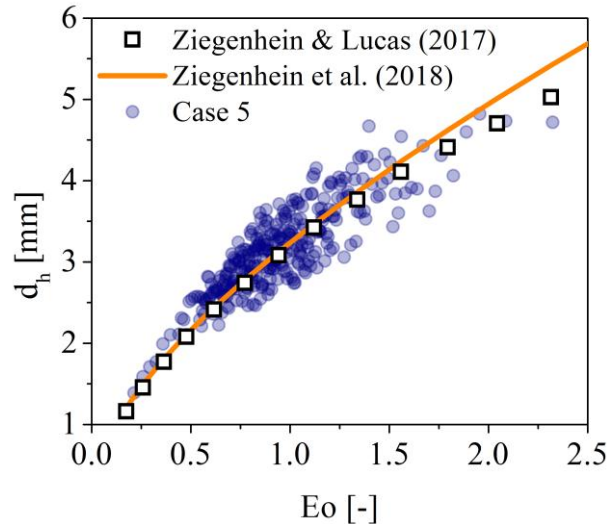


Figure 3-16: Comparison of resulting bubble major axis with experimental data [35,68],  $Q_g=160$  L/h,  $\bar{d}_b = 2.55$  mm, Case 5: With oscillation model (D2,L1).

The bubble major axis from Case 5 was obtained from Eq. (2-64), in which the data from Sommerfeld and Bröder [56] was used as input parameters. As seen in the Figure 3-16, such results are in good agreement with other data present in the literature, where the same system (air-water) was evaluated.

As aforementioned, the bubble eccentricity plays a role not only in the drag force, but also in the other forces, mainly in added mass and transversal lift. While the prediction of added mass coefficient is already well established in the literature, the transversal lift present complex dependencies with fluid properties, bubble size and shape. Until end of last year, the lift coefficient for bubbles in low-viscosity systems, e.g. air-water, was not fully clear, and only numerical predictions have been done hitherto. Ziegenhein et al. [35] provided then experimental data in these flow conditions, which supported directly the development of the present CFD model. In this framework, the results obtained using the recent lift data (“L2”) will be shown in the following. According to the Table 3-2, this model setup corresponds to the Case 6 and the results obtained for this case are shown in the Figure 3-17.

Note in the Figure 3-17a and b that the predicted lift coefficient using the approach “L1” was almost constant and equal to 0.288 for the whole bubble size spectrum, resulting in a narrow PDF. When the second lift approach is considered (“L2”), not only the mean value for  $C_L$  is evidently increased, shifting the PDF to the right-hand side of Figure 3-17b, but also a direct dependency with bubble eccentricity/major axis is revealed, where the scatter in the Figure 3-17a disperses away from the mean correlation line “L2”.

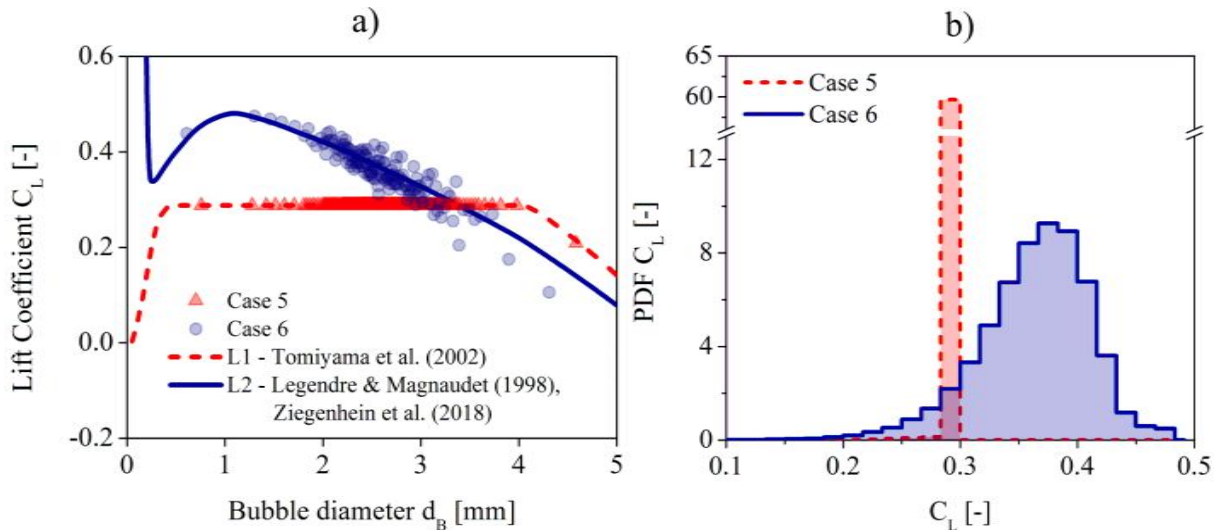


Figure 3-17: a) Comparison of resulting lift coefficients  $C_L$  from Cases 5 and 6 with the correlations [31,34], b) resulting PDFs for  $C_L$ ,  $Q_g=160$  L/h,  $\bar{d}_b = 2.55$  mm, Case 5: With oscillation model (D2,L1), Case 6: With oscillation model (D2,L2).

In order to evaluate the impact on the velocity profiles and bubble dispersion, the results from Case 5 and 6 are compared in the Figure 3-18. Here, the profiles regarding the averaged bubble vertical velocity and volume fraction are exposed for two cross-sections in the bubble column, namely at 325mm and 450mm above the aerator. As noticed in the Figure 3-18a and c, either considering the bubble dynamics model or not, both lift models yield practically the same bubble rise velocities. However, once the strongest contribution of the lift force in bubbly flows lies on the horizontal direction, a significant effect appears in terms of bubble volume fraction, as seen in the Figure 3-18b and d. The lift model proposed by Tomiyama et al. [31], which was used in the cases Case 3 and 5, may underestimate the resistance coefficient for small bubbles ( $d_h < 3$  mm), indeed, as seen in the Figure 3-18a. When the second approach for the lift model is considered (Cases 4 and 6), an enhancement of bubble dispersion towards the wall is observed. Such differences come into sight around 325mm of column height and become stronger at longer residence times, as seen in the Figure 3-18d. Unfortunately, no local measurements of bubble volume fraction was provided by Sommerfeld and Bröder [56], which would be a potential validation data.

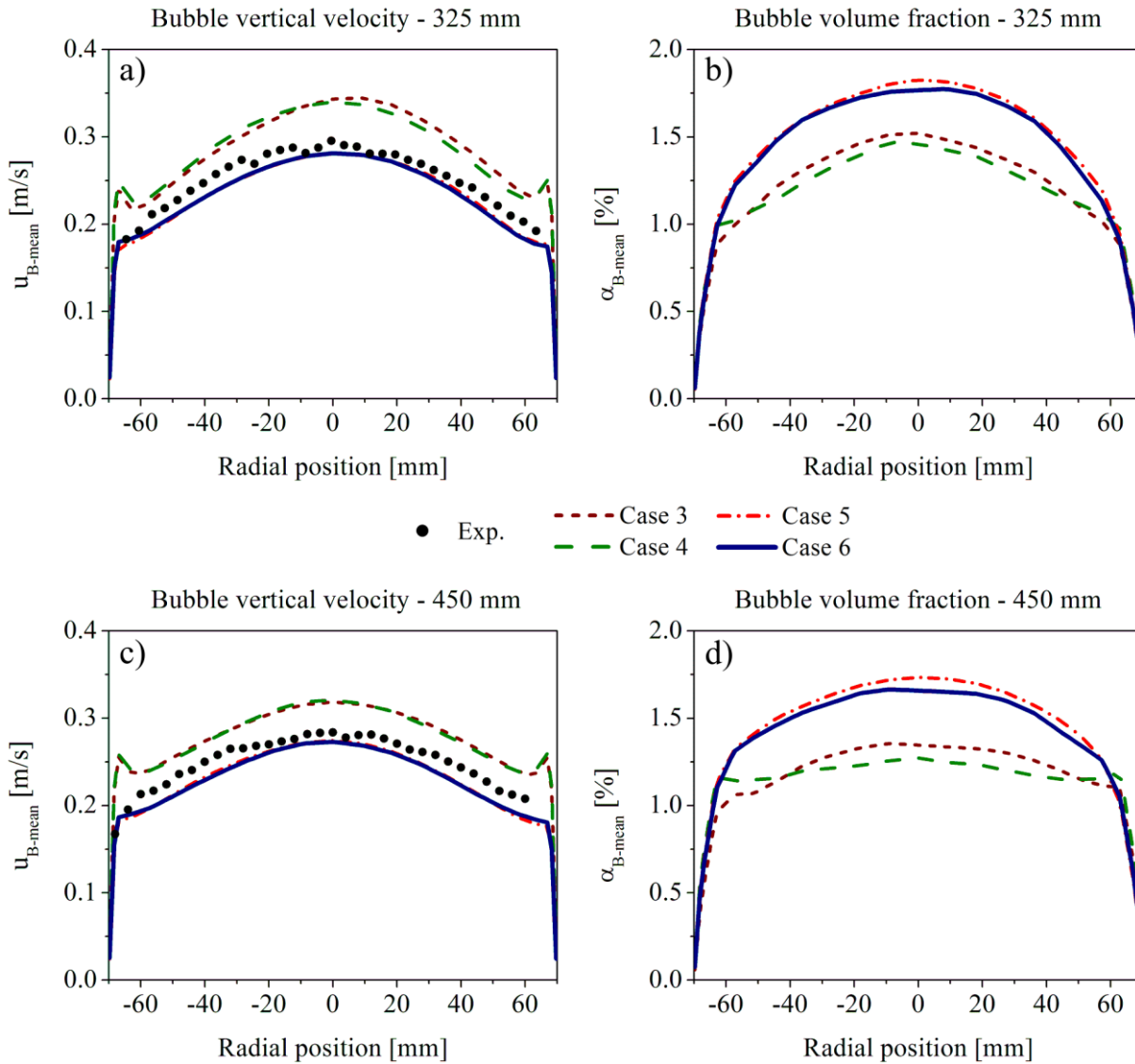


Figure 3-18: Comparison of bubble average profiles: a,c) vertical velocity; b,d) volume fraction. Experimental data: Sommerfeld and Bröder [56],  $Q_g=160$  L/h,  $\bar{d}_B=2.55$  mm, Case 3: No oscillation model (D1,L1), Case 4: No oscillation model (D1,L2), Case 5: With oscillation model (D2,L1), Case 6: With oscillation model (D2,L2).

The interesting part is, at only 450mm above the aerator the relative difference between the cases reaches almost 5%, as seen in the Figure 3-19. This denotes a long term effect of lateral forces on bubble motion, which should not be ignored. Further discussion about the lift approaches in term of force magnitude will be shown later in the subsection 3.3 of this work.

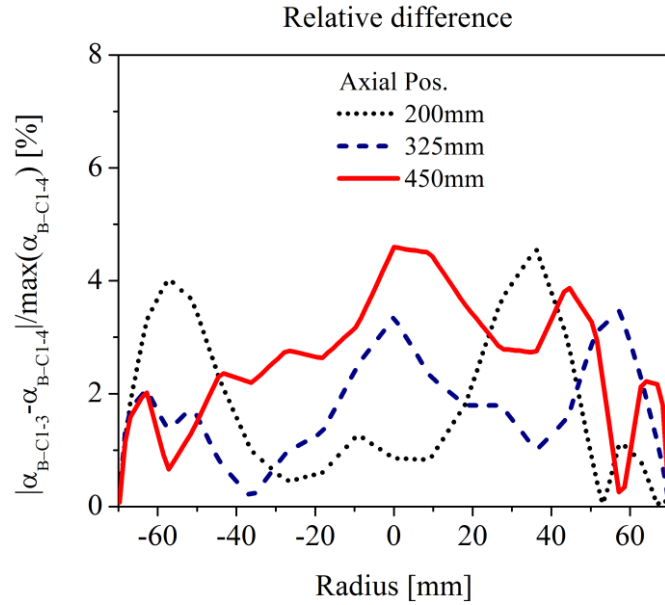


Figure 3-19: Normalized difference of bubble volume fraction between Cases 5 and 6 using different lift models in various axial positions;  $Q_g=160$  L/h,  $\bar{d}_B=2.55$  mm, Case 5: With oscillation model (D2,L1), Case 6: With oscillation model (D2,L2).

In order to lay out the influence of the Basset force on the present results, a simulation in which the history term is neglected (Case 7) was performed. The bubble volume fraction profiles from the Cases 6 and 7 were compared for three cross-sections along the column height, as seen in the Figure 3-20.

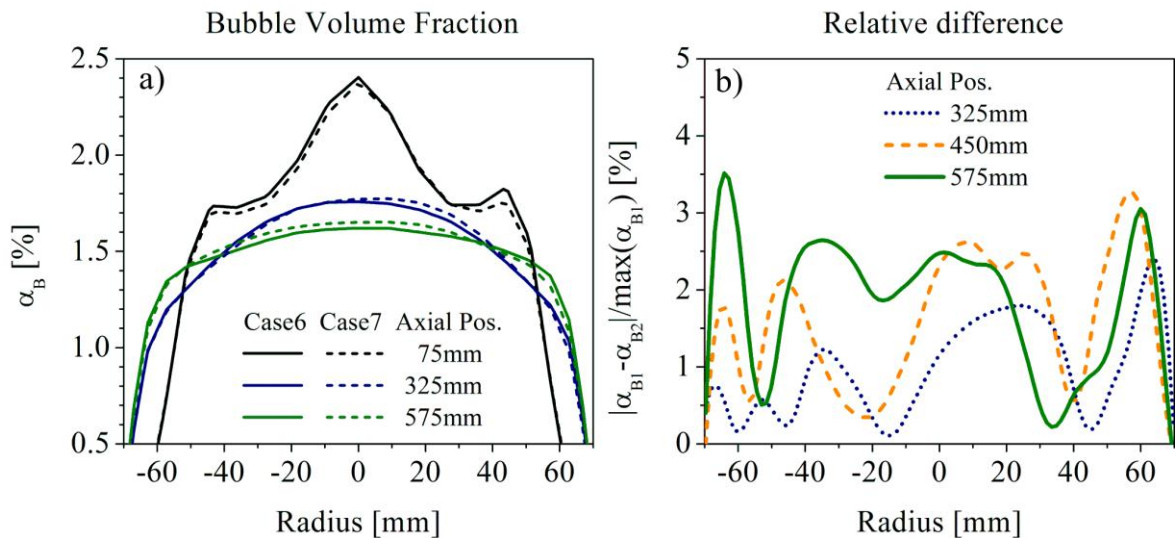


Figure 3-20: Comparison of Cases 6 and 7: a) influence of Basset force on bubble volume fraction; b) relative difference of bubble volume fraction;  $Q_g=160$  L/h,  $\bar{d}_B=2.55$  mm, with oscillation model; Case 6: D2,L2,with Bassset; Case 7: D2,L2,no Basset.

Note in the Figure 3-20a, that this force promotes slightly lateral dispersion of bubbles. Close to the aerator (75 mm) the effect is not remarkable and the results from case 6

and 8 are practically the same. However, 250 mm above, the difference is somewhat notable and grows with the ascension distance. In half a meter over the first cross-section, the relative error increases up to 3.5%. This only reinforces the importance to consider the Basset force.

With respect to the bubble average vertical velocities, no significant change is found between Cases 6 and 7, though, as seen in the Figure 3-21. From an interesting point of view, this force acts as a resistance to the bubble oscillation imposed by model, decreasing the resulting RMS values of velocity fluctuation on all directions, as seen in the Figure 3-21a. Even though, against our intuition, the Basset force supports somehow the bubble overall lateral dispersion. This curious behaviour will be further investigated in the section 3.4. Moreover, a slightly reduction of liquid vertical velocity is noticed in the Figure 3-21b. Since the bubbles are more distributed in the domain, the core and down flows are smoothed and lower velocity gradients are revealed.

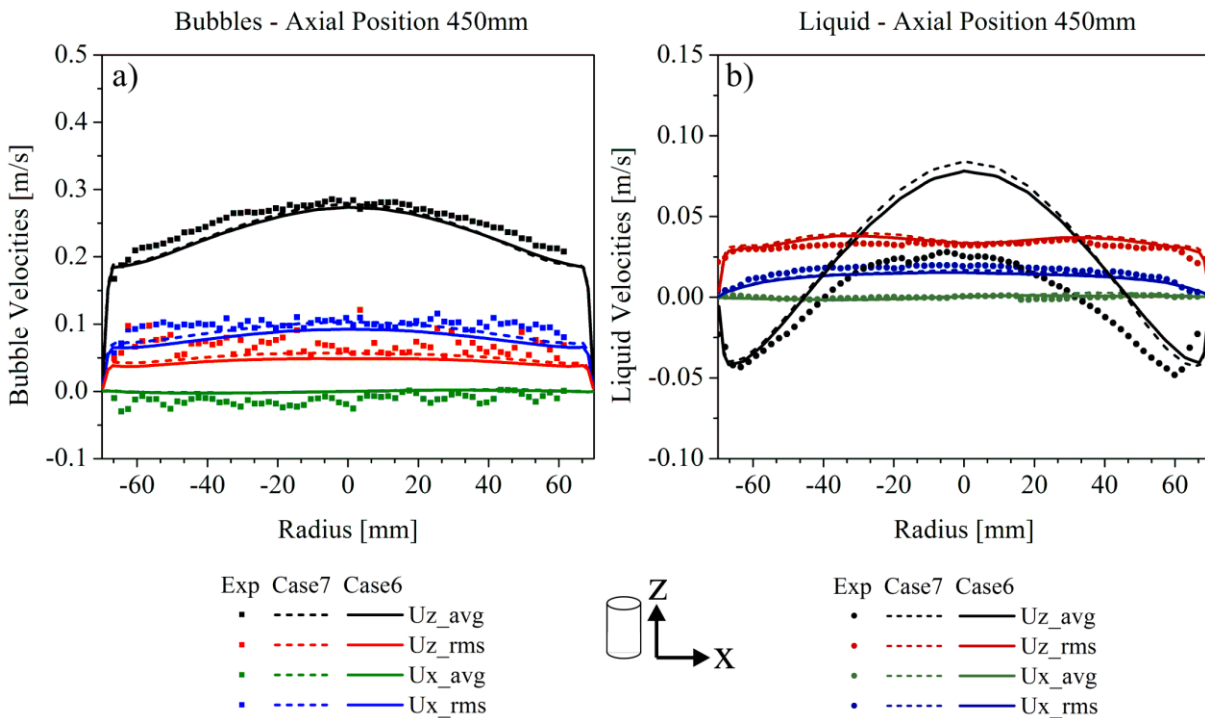


Figure 3-21: Comparison of averaged velocities and RMS values from Cases 6 and 7 with experimental data [56]: a) Bubbles; b) Liquid;  $Q_g=160$  L/h,  $\overline{d_B}=2.55$  mm, with oscillation model; Case 6: D2,L2,with Basset; Case 7: D2,L2,no Basset.

A summary of the cases with respect to fluctuating energies of continuous and dispersed phases is presented in the Figure 3-22. In order to avoid showing excessive data, only the results from cases 4, 6 and 7 are exposed here, in which the second approach for the lift force (“L2”) was used.

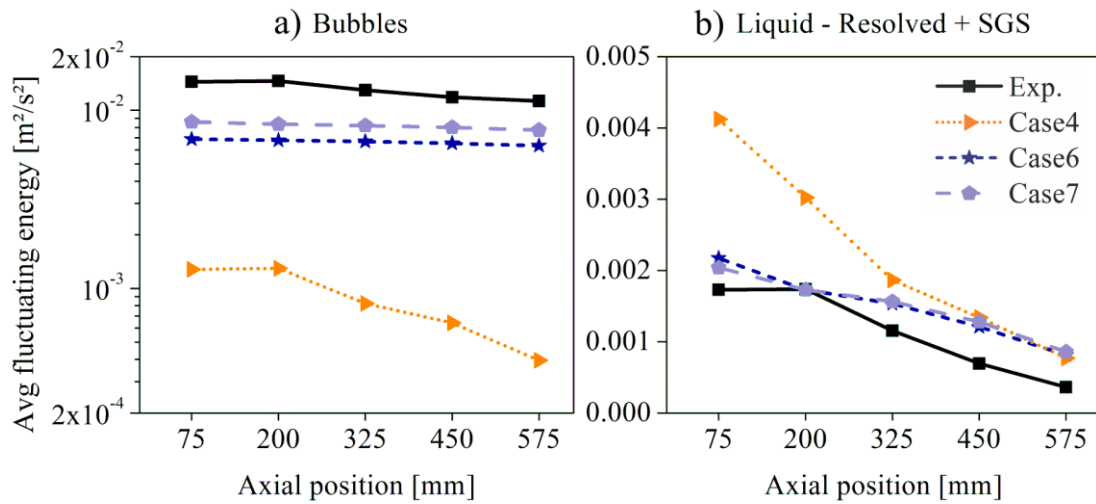


Figure 3-22: Averaged fluctuating energies of: a) bubbles; b) liquid.

Experiments by: Sommerfeld & Bröder [56];  $Q_g = 160 \text{ L/h}$ ,  $d_{B,\text{mean}} = 2.55 \text{ mm}$ ;

Case 4: no oscillation, D1, L2, with Basset;

Case 6: with oscillation, D2, L2, with Basset; Case 7: with oscillation, D2, L2, no Basset.

Note in the Figure 3-22a that when bubble dynamics are neglected (Case 4), the averaged fluctuating energy of bubbles is clearly underestimated in almost one order of magnitude. Additionally, the decay of energy with the column height in this case is steeper than observed experimentally. The inclusion of bubble dynamics in the Cases 6 and 7 implies a better agreement with experiments not only qualitatively but also quantitatively. Nevertheless, the resulting bubble fluctuations are still not equivalent to the measurements. Furthermore, the fact of the Basset force to smooth bubble fluctuations imposed by the oscillation model is here reinforced, as seen in the Figure 3-22a. Although better results (in this case) are achieved neglecting this force, it would be a non-sense not to consider it.

The fluctuating energies with regard to the liquid phase in the Figure 3-22b comprehend both the resolved and unresolved scales. Here, the opposite scenario is found, in which the numerical results reveal higher fluctuations than the experiments. In the Case 4, as aforementioned, the bubble rise almost straight and the distribution in the domain may be underestimated. Additionally, the overestimation of bubble velocity produce higher liquid velocity gradients between core and down flows than expected in the Case 6, as shown in the Figure 3-13, and consequently stronger fluctuations. The discrepancy is more notable in the lower cross-sections than in the column top, as seen in the Figure 3-22b. In order to expose this behaviour, a numerical visualization at the bubble inlet is shown in the Figure 3-23. Once the bubble injection is made in fixed positions accordingly to the experiments (see Figure 3-1), clear line streams of bubbles are notable in the Case 4 even after a height of 75 mm. The vicinity of the wall in there is still free of bubbles, thus, there is no resistance to the liquid

downstream and no turbulent diffusion induced by bubbles. As consequence, the RMS values of liquid velocity fluctuations from Case 4 are greater than from Cases 6 and 7, where bubble dynamics is included. In these last two cases, the imposed bubble lateral dispersion by the oscillation model implies a more stable and homogeneous liquid flow, as seen in the Figure 3-23b and d, as follows:

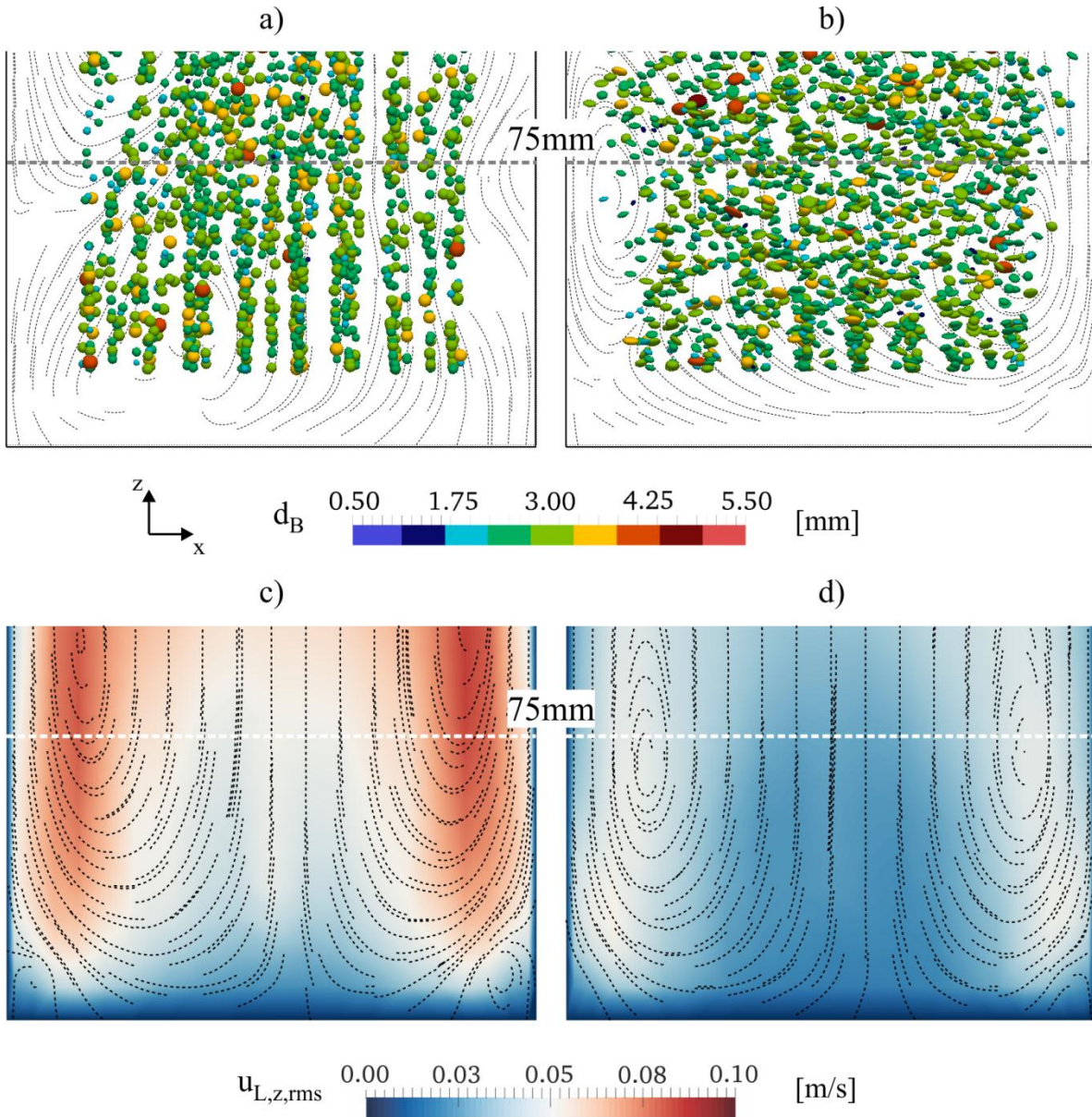


Figure 3-23: Numerical visualization of the discrete phase and RMS of vertical velocity fluctuations from the continuous phase for: a and c) Case 4; b and d) Case 6.  $t = 500\text{s}$ . Axial position: bottom;  $Q_g = 160\text{ L/h}$ ,  $d_{B,\text{mean}} = 2.55\text{ mm}$ ; Case 4: no oscillation, D1,L2; Case 6: with oscillation, D2,L2.



Furthermore, these very results were evaluated in terms of anisotropy, in which the fluctuating energy ratio  $k_{\text{ratio}}$  between the horizontal and vertical directions is calculated as follows:

$$k_{\text{ratio}} = \frac{k_{\text{hor}}}{k_{\text{ver}}} = \frac{k_{(u')}}{k_{(w')}} \quad (3-3)$$

$$k_{(x)} = \frac{1}{A} \sum_{i=1}^n 0.5 \overline{x^2}_i A_i \quad (3-4)$$

where  $x$  is the RMS values of bubble fluctuating velocity in the correspondent direction. The resulting ratios are shown in the Figure 3-24a in terms of absolute value.

As expected from the profiles of velocity fluctuations provided by Sommerfeld and Bröder [56], the anisotropy is clearly greater than the unity ( $k_{\text{hor}} > k_{\text{ver}}$ ). As seen in the Figure 3-24a, the ratio grows with the column height, inasmuch as the bubble injection induces substantial recirculation of liquid in that region. At higher cross-sections, the bubbles are more dispersed in the domain, and consequently, the vertical fluctuations decrease while the horizontal ones remain almost the same. This behaviour was not attended by the model setup in Case 4, in which the resulting ratio is far below the unity. The Cases 6 and 7, on the other hand, reveal a better qualitative agreement with experimental data, although the anisotropy was overestimated in both cases. The cause for such discrepancy lies on the vicinity of the wall, namely for wall distances less than 20mm. The experimental observations presume a slightly increase of fluctuations in the vertical direction, not predicted in the simulations. This error is accentuated when the averaged is based on the correspondent ring-area. Nevertheless, a merely qualitative comparison is shown in the Figure 3-24b, by subtracting the initial ratio  $k_0 = (k_{\text{ratio},75} - 1)$  from the same results. Note that the consideration of Basset force yields a better increase of anisotropy along the column.

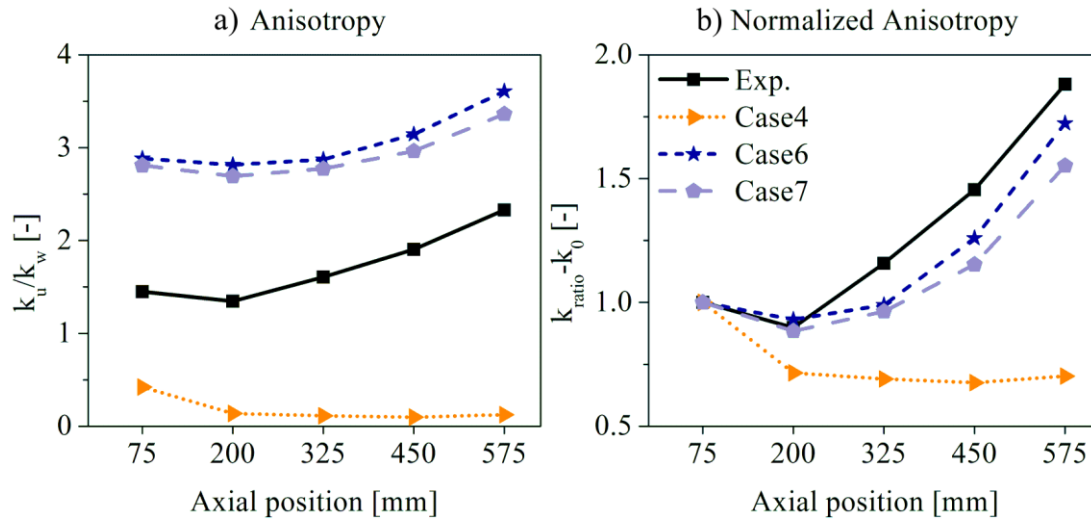


Figure 3-24: Averaged fluctuating energy anisotropy: a) Absolute value; b) Normalized anisotropy. Experiments by: Sommerfeld & Bröder [56];

$Q_g = 160$  L/h,  $d_{B,mean} = 2.55$  mm; Case 4: no oscillation, D1,L2,with Bassset;  
Case 6: with oscillation,D2,L2,with Bassset; Case 7: with oscillation,D2,L2,no Bassset.

Assuming from the results evaluated so far that the model setup from Case 6 is the best choice within the proposals of this work (see Table 3-2) and flow conditions of this study case, a simulation was conducted for the reference case “B1” (Sommerfeld and Bröder [56]), where a different bubble size distribution is investigated. Unfortunately in the experiments, the increment on bubble size deteriorated somehow the data acquisition for the liquid phase, and no fair comparison with experimental results was possible. Nevertheless, the same evaluation as before regarding the bubble velocities is realized and shown in the Figure 3-25. Note that the consideration of bubble dynamics on the model (Case 9 – solid lines) improves significantly the results when compared to Case 8 (without bubble dynamics – dashed lines), not only for the average vertical velocity but also the fluctuations. Contrastively to the previous reference case (“A2”, see Figure 3-21), the resulting bubble rise velocity is here slightly overestimated. Nevertheless, an overall agreement is achieved in both Cases 6 and 8.

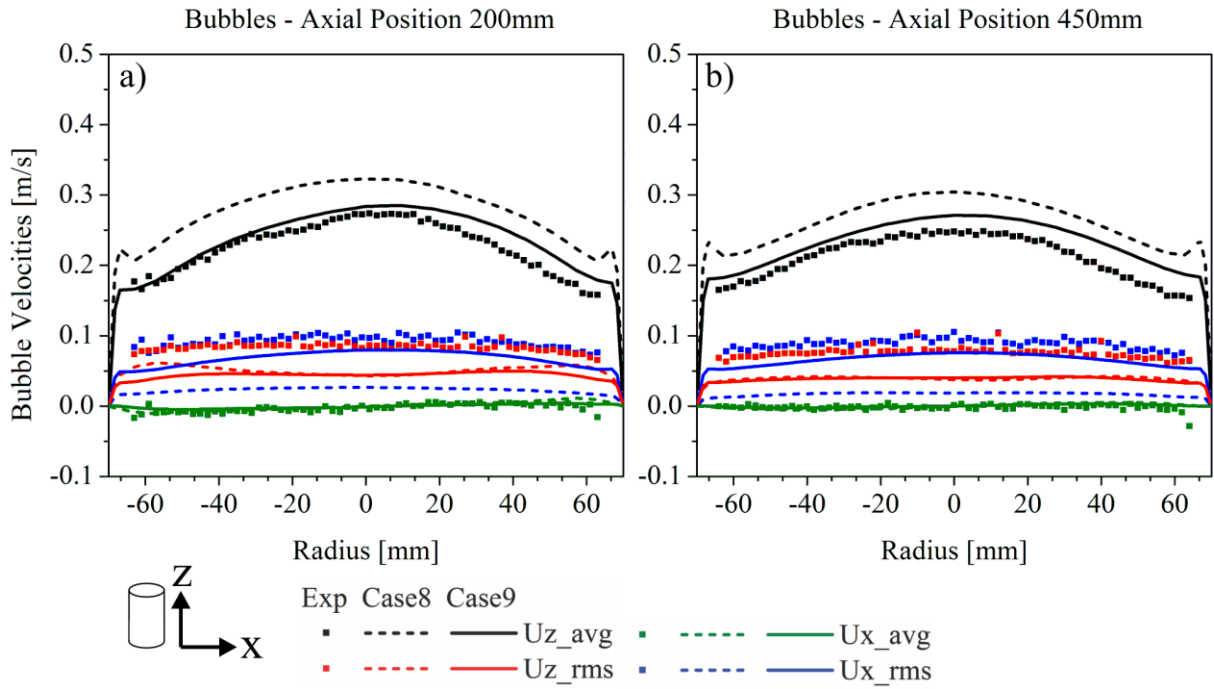


Figure 3-25: Comparison of numerical bubble averaged velocities and RMS values with experimental data [56] in axial positions: a) 200mm; b) 450mm;  
 $Q_g = 160 \text{ L/h}$ ,  $d_{B,mean} = 3.31 \text{ mm}$ ;  
 Case 8: no oscillation, D1, L2; Case 9: with oscillation, D2, L2.

Moreover, a reduction of bubble fluctuating energy from the reference case “A2” to “B1” was experimentally observed [56]. This evidence was attained by the model, as seen in the Figure 3-26, once the oscillations depend directly on bubble size (Eq. (2-56)). In this framework, a qualitative agreement with experimental was achieved only when bubble dynamics are considered.

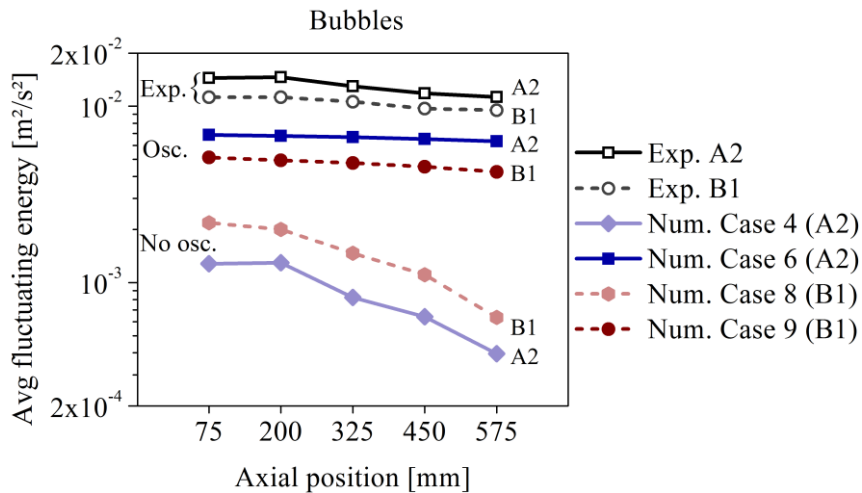


Figure 3-26: Summary of averaged fluctuating energies of bubbles.  
 Experiments by: Sommerfeld & Bröder [56].  $Q_g = 160 \text{ L/h}$ .

Although only an increase of 30% of mean bubble diameter is noticed from the reference cases “A2” to “B1”, the same gas flow-rate ( $Q_g = 160$  L/h) is represented by around the half number of bubbles. A numerical visualization of this matter is exposed in the Figure 3-27 for the axial position 325mm. The interesting part is that different flow conditions are expected between the cases, inasmuch as all the forces depend on the bubble size.

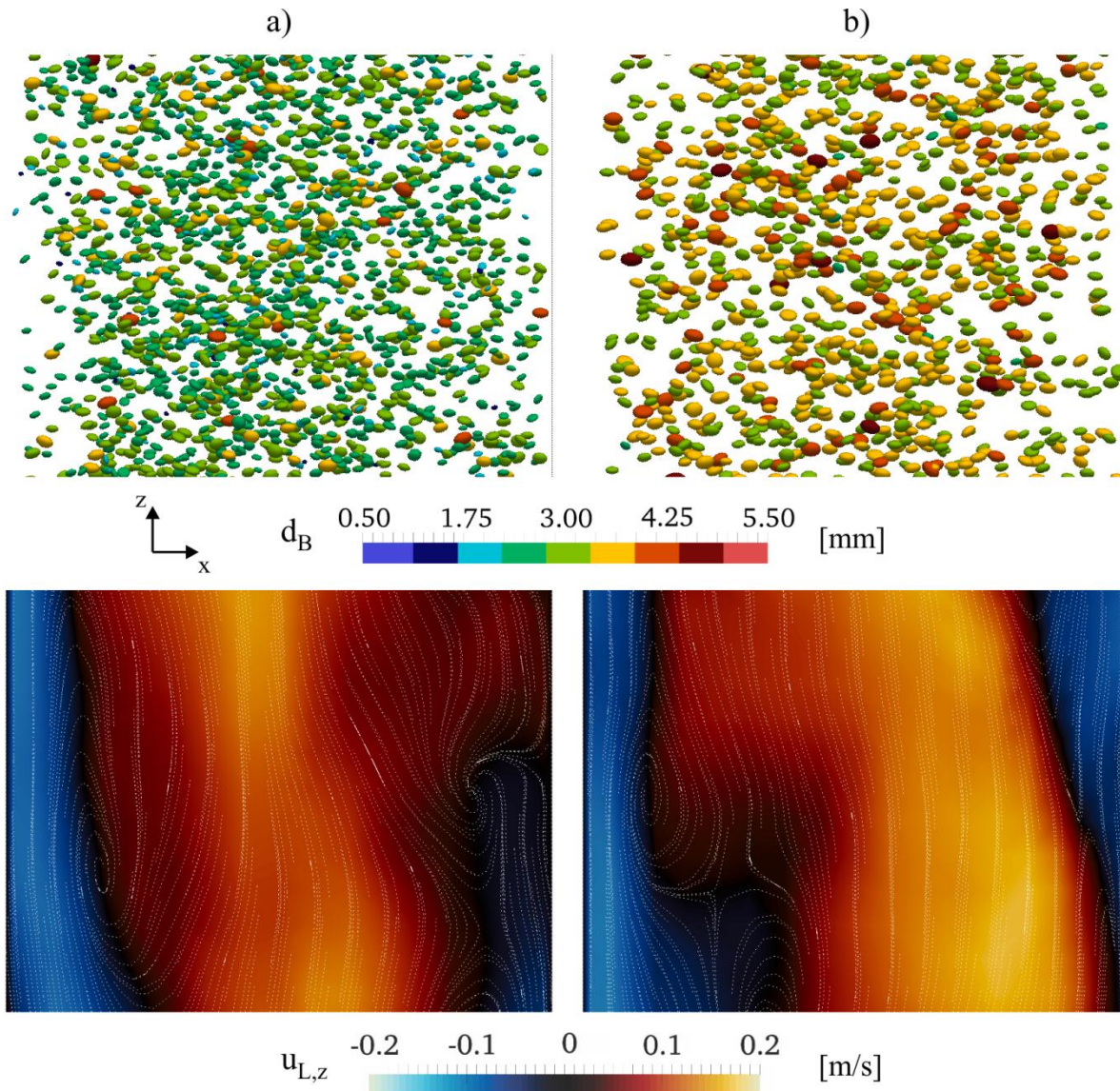


Figure 3-27: Numerical visualization of the discrete phase and vertical velocity of continuous phase for: a) Case 6; b) Case 9.  $t = 500$ s.  $Q_g = 160$  L/h. Axial position: 325mm.

Case 6: with oscillation, D2, L2,  $d_{B,mean} = 2.55$  mm;

Case 9: with oscillation, D2, L2,  $d_{B,mean} = 3.31$  mm.

Within the scope of forces acting on bubbles, the resulting drag and lift coefficients from Cases 6 and 9 are shown in the Figure 3-28. While the drag coefficient increases with bubble size (in this range), the opposite behaviour occurs for the lift force. This increase of

drag coefficient alone does not mean directly, of course, that a greater bubble will experience a lower rise velocity, since all other acting forces change, either. The buoyancy, for example, has a cubic dependency with bubble diameter ( $\mathcal{O} \sim d_B^3$ ), while drag has a quadratic one  $\mathcal{O} \sim d_B^2$ . Nevertheless, in a bubble swarm, the local flow circumstances perceived by each bubble are naturally different than those for isolated bubbles in a quiescent liquid. In order to illustrate this matter, the resulting residence times from many bubble samples along the whole column were classified by size and shown in the Figure 3-29.

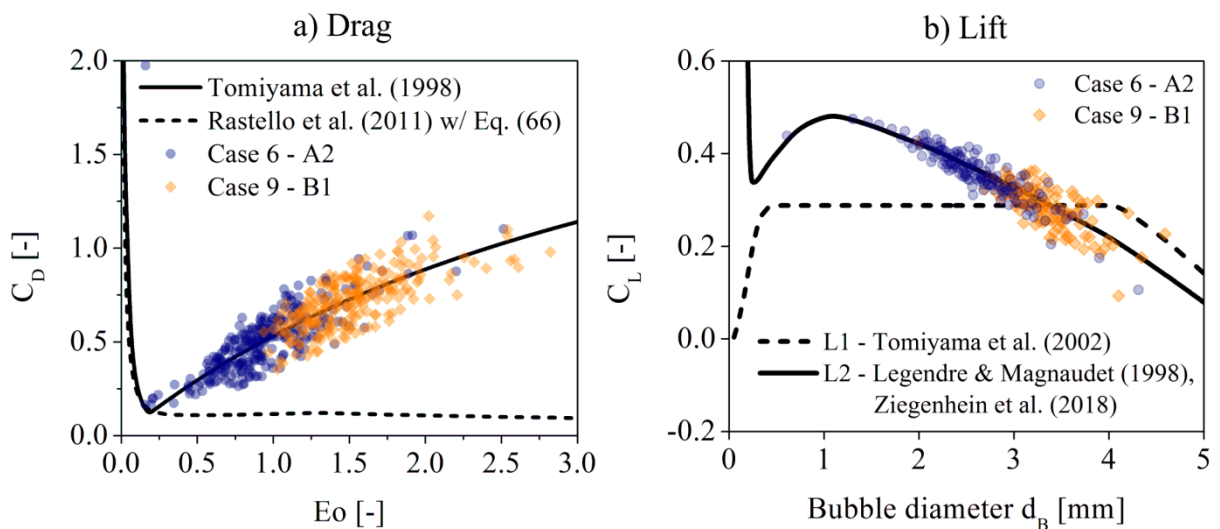


Figure 3-28: Resulting coefficients from Cases 6 and 9 for:  
a) drag force; b) lift force.  $Q_g = 160$  L/h;  
Case 6: with oscillation,D2,L2,  $d_{B,mean} = 2.55$  mm;  
Case 9: with oscillation,D2,L2,  $d_{B,mean} = 3.31$  mm.

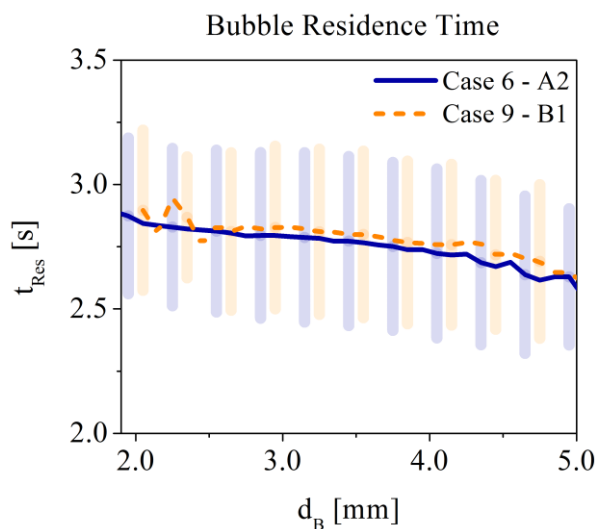


Figure 3-29: Resulting bubble residence time for Cases 6 and 9;  $Q_g = 160$  L/h;  
Case 6: with oscillation,D2,L2,  $d_{B,mean} = 2.55$  mm;  
Case 9: with oscillation,D2,L2,  $d_{B,mean} = 3.31$  mm.

Note that the residence time for the same size of bubbles increases from Case 6 to 9, namely between diameters 3 and 4 mm where enough statistics are found in both cases. This means that bubbles of those sizes are accelerated by the wake from more bubbles in the domain.

Finally, a comparison of Cases 6 and 9 is made with colour fields in terms of average bubble and liquid velocities, turbulent kinetic energy and volume fraction is shown in the Figure 3-30. Since the resulting fields reveal enough symmetry, only the half of the column is exposed, in which the left-hand side from each field is reserved for the Case 6 (Ref. “A2”) and the right-hand side for the Case 9 (Ref. “B1”).

Note in the Figure 3-30a and c, that the averaged liquid and bubbles vertical velocities from Cases 6 and 9 present apparently no difference. Nevertheless, at the bottom of the column, the influence of bubble injection is evident, inasmuch as the capillaries are concentrated in a certain core region and produce a peak of velocity just above. Moreover, once the liquid and bubble phases are directly coupled both in resolved momentum and SGS turbulence, the BIT contribution on the SGS viscosity is notable in the Figure 3-30b. Here, higher values of SGS viscosity in the lower half of column reflect the presence of bubbles disturbing the flow more intense than at the column top, where certain lateral dispersion is achieved, as seen in the Figure 3-30d. Furthermore, the bubbles emerging at the free surface induce also motion in the continuous gas-phase above the water level. In this manner, a higher influence from bubbles on SGS viscosity in Case 9 (“B1”) is there exposed due to their greater size and volume of fluid dislocated.

While similar results for the averaged bubble and liquid velocities were found between Cases 6 and 9, the RMS values of velocity fluctuations reveal a different behaviour. As seen in the Figure 3-31, these results are here shown for both vertical and horizontal directions. Note in the Figure 3-31a and b that the vertical liquid fluctuations present their maximum where the upstream meets the downstream, mainly at the lower half of the column, where the bubbles did not fully distributed in the cross-section. Despite of that, the sparser momentum source-terms from bubbles with more inertia on Case 9 produced higher fluctuations on the liquid phase than in Case 6, as seen in the Figure 3-31a and b. Regarding the bubble phase, on the other hand, the inverse behaviour is noticed, as seen in the Figure 3-31c and d. Here, the bubble velocity fluctuations in both directions are reduced from Case 6 to 9, which is expected from the model (Eq.(2-56)) and also observed experimentally [56].

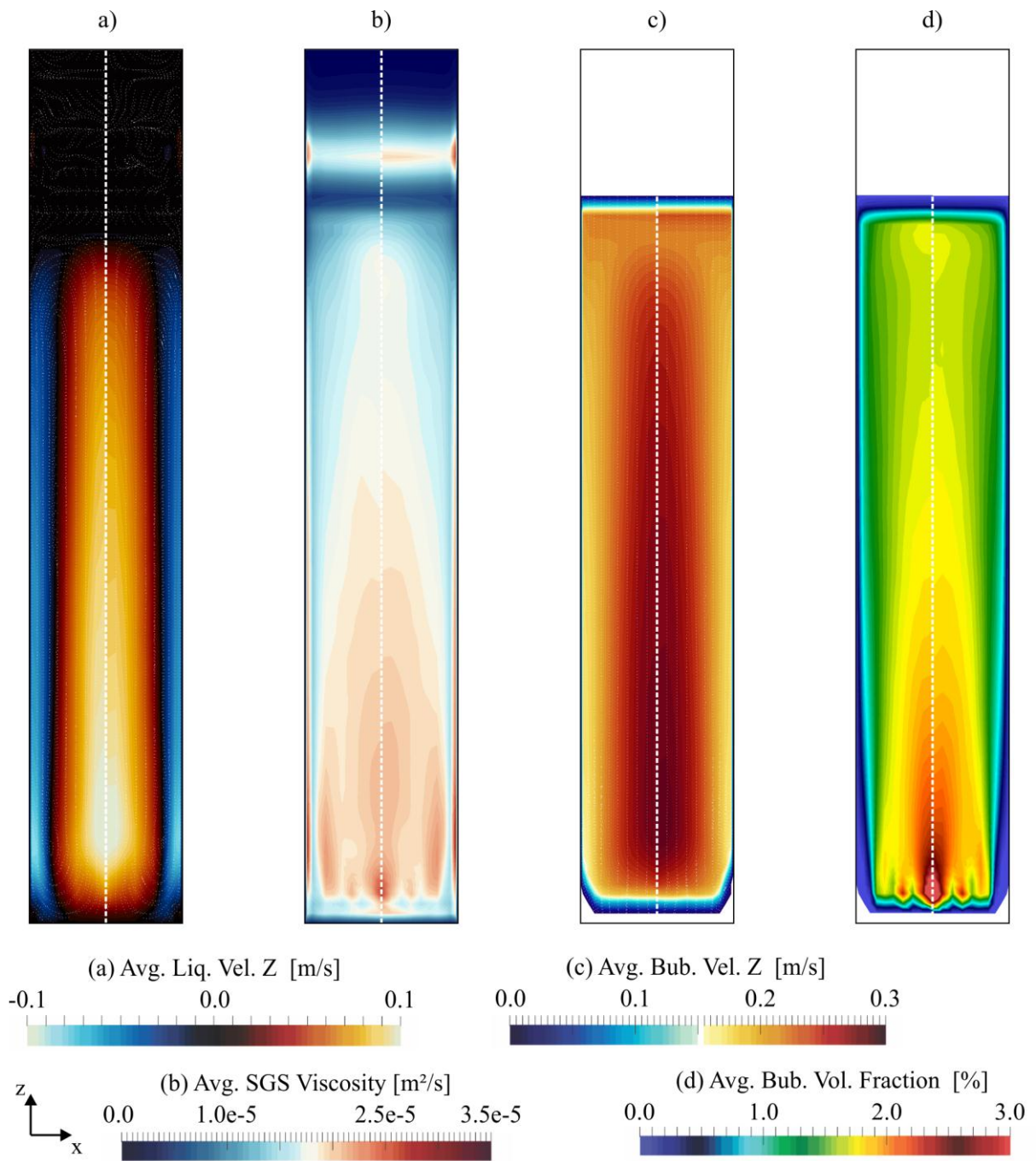


Figure 3-30: Colour fields of Cases 6 and 9 with regard to: a) liquid velocity; b) turbulent kinetic energy; c) bubble velocity; d) bubble volume fraction. Left-hand side: Case 6 (Ref. “A2”); Right-hand side: Case 9 (Ref. “B1”).  $Q_g = 160$  L/h.

Case 6: with oscillation, D2, L2,  $d_{B,mean} = 2.55$  mm;

Case 9: with oscillation, D2, L2,  $d_{B,mean} = 3.31$  mm.

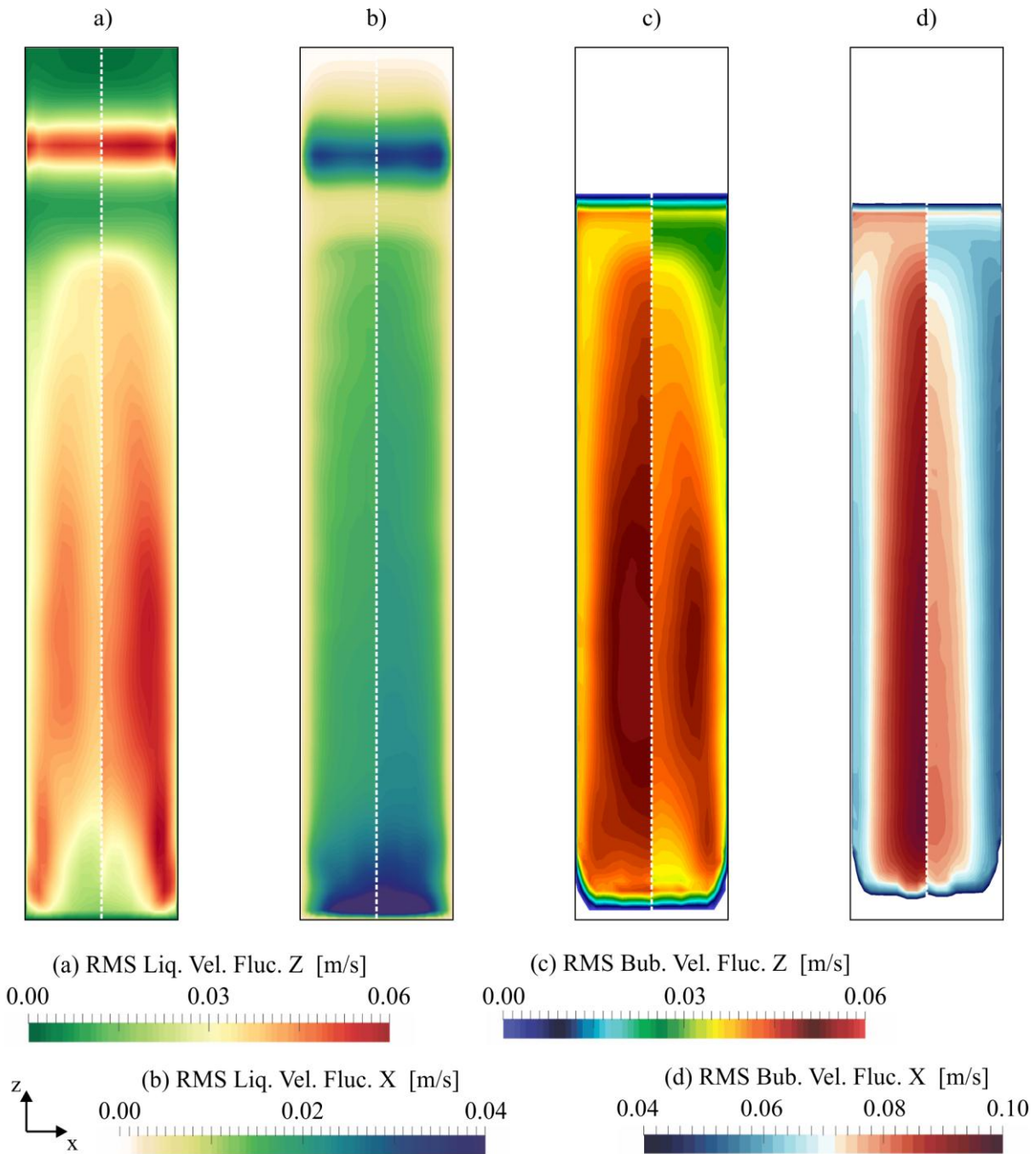


Figure 3-31: Colour fields of Cases 6 and 9 with regard to RMS values of: a) liquid vertical velocity fluctuations; b) liquid horizontal velocity fluctuations; c) bubble vertical velocity fluctuations; d) bubble horizontal velocity fluctuations. Left-hand side: Case 6 (Ref. “A2”);

Right-hand side: Case 9 (Ref. “B1”).  $Q_g = 160$  L/h.

Case 6: with oscillation, D2, L2,  $d_{B,mean} = 2.55$  mm;

Case 9: with oscillation, D2, L2,  $d_{B,mean} = 3.31$  mm.

The interesting part of all this is, that the resulting flow and its characteristics are driven originally by a field force (buoyancy) acting on the bubbles, once no inlet/outlet liquid flow is imposed in these cases. However, in order to achieve a certain level of detail and rigor on the simulations, the proper modelling of the coupled forces is naturally required. As



aforementioned, the resistance coefficients of these forces present a complex dependency with bubble size, eccentricity and also the flow conditions around the bubbles. Additionally, the use of “point-mass” approximation allows storing easily the information of forces values on each bubble individually. In this framework, an evaluation of forces competition in this very bubble column will be presented in the following.

### 3.3 On the Forces Competition

The measurement of the forces acting on bubbles and their resistance coefficients is made experimentally on special conditions, in order to isolate the effect of a certain force and minimize experimental errors. Such measurements would be not possible or too much complex to realize in the flow conditions from a bubble swarm, such as the one described in the previous section (3.2). On the hand, numerical simulations can give a local estimation of these forces separately and statistics can be easily performed on the whole domain of evaluation. In this manner, the relevance of each individual force classified in many aspects will be shown in the following as a plain numerical study.

#### 3.3.1 Cases descriptions and setup

The cases descriptions and the bubble size distribution are shown in the Table 3-3.

Table 3-3: Cases description for different simulations.  $Q_g=160$  L/h.

	Ref.	All Forces	Drag Model	Lift Model	TDM/ BIT	Osc. Model	$\overline{d_B}$ [mm]	$\overline{\frac{d_B}{\Delta x}}$	$\frac{d_{B,max}}{\Delta x}$
Case 1-1	A2	x	D1–Eq.(2-15)	L1–Eq.(2-31)	x		2.55	0.31	0.54
Case 1-2	A2	x	D1–Eq.(2-15)	L2–Eq.(2-39)	x		2.55	0.31	0.54
Case 1-3	A2	x	D2–Eq.(2-21)	L1–Eq.(2-31)	x	x	2.55	0.31	0.54
Case 1-4	A2	x	D2–Eq.(2-21)	L2–Eq.(2-39)	x	x	2.55	0.31	0.54
Case 2-4	B1	x	D2–Eq.(2-21)	L2–Eq.(2-39)	x	x	3.31	0.40	0.60

The assessment of forces competition in the bubble column will be shown in the following in two ways. At first, the magnitude of each individual force is related to the buoyancy as a ratio of importance. The buoyancy force was naturally chosen as reference, since it is a field force, independent of flow conditions and the strongest one. All the instantaneous and local resulting ratios were then classified in terms of bubble size, Stokes number, axial (column height) and radial (wall distance) positions. Subsequently, an arithmetic average of the force ratio  $\overline{F_i}$  inside each class was obtained according to the following equation:

$$\bar{F}_l = \frac{1}{N} \sum_{j=1}^N \frac{|F_{i,j}|}{|F_{buoyancy,j}|} \quad (3-5)$$

where  $N$  is the total number of samples inside the class,  $i$  is the force and  $j$  the individual sample. Note that the information of force direction is deliberately lost by extracting the vector magnitude inside the summation function. In this manner, only the force strength is questioned, either accelerating the bubble or acting against its motion.

The second evaluation was made by extracting the overall force contribution in the radial direction. The objective here is to know if the force pushes the bubbles towards the wall or away from it. In order to do so, the average force contribution in the radial direction  $\bar{F}_{l,r}$  can be calculated as follows:

$$\bar{F}_{l,r} = \frac{1}{N} \sum_{j=1}^N \frac{F_{i,r,j}}{|F_{buoyancy,j}|} = \frac{1}{N} \sum_{j=1}^N \frac{(\mathbf{F}_{i,j} \cdot \mathbf{n}_{r,j})}{|F_{buoyancy,j}|} \quad (3-6)$$

where  $\mathbf{n}_{r,j}$  is a unit vector in the radial direction to the bubble position. Note that a positive value of  $F_{i,r,j}$  means a resulting force towards the column wall, and a negative one the opposite. In this framework, a radially symmetric force contribution would be obtained when  $\bar{F}_{l,r} = 0$ .

### 3.3.2 Magnitude ratio

The resulting forces ratios for cases C1-1 and C1-3 with regard to bubble diameter and stokes number are shown in the Figure 3-32. The graphs on both sides present the same data, but the scale range was modified for a better visualization of results below 10%.

In the case without bubble oscillation model (C1-1, dashed lines in the Figure 3-32) the drag is clearly the most important force with magnitudes over 90% of buoyancy. Expectedly, a minimum peak is observed between bubble sizes of 1 and 2 mm, resulting from a lower resistance coefficient predicted by Eq. (2-15). In the second place comes the added mass force, which presents values of 10-20% of buoyancy. Since this force is related to the displaced volume of fluid due to bubble acceleration, a slightly increase of its magnitude with bubble diameter is observed in the Figure 3-32a. Surprisingly, the Basset term is the third strongest force in this case. For small bubbles sizes the Basset force reaches up to 7% of buoyancy, while transversal lift approaches only 4%. The fluid inertia (part of pressure term)

seemed to be independent of bubble size and its magnitude was around 1% of buoyancy. Since these results come from a averaging of the whole bubble column, the wall force is apparently insignificant and a proper evaluation will be shown later.

As seen in the Figure 3-32b, where the same results are classified by bubble Stokes number, the order of forces magnitude is maintained. Drag, added mass and wall forces are practically constant for the range of bubble Stokes number, except for values higher than 0.4. Since a very small number of samples were obtained in this region, statistics may be not well represented. On the other hand, Basset, lift and fluid inertia forces increase with Stokes number.

When the oscillation model is considered (case C1-3, solid lines in the Figure 3-32), a different scenario is observed. The drag force, which before was almost equivalent to buoyancy, was evidently reduced. This may happened due to continuous change of motion direction imposed by the model, reducing locally the slip velocity magnitude. In counterpart, this everlasting oscillating motion increase considerably the added mass force, once the derivative in time of bubble velocity in Eq. (2-14) becomes always present and substantial. This behaviour is sure not observed for bubbles with diameter below 1 mm, where the oscillation model has no effect. For bubble diameters a little above the unity, the virtual mass force reaches values up to 80% of buoyancy magnitude, even higher than drag. From this size up to 5 mm, a loss of added mass importance is revealed in the Figure 3-32a, once the frequency of bubble oscillation is also decreasing, as predicted by Eq. (2-56). This very behaviour is also noticed for the history term, whose ratio of magnitude was enhanced up to 50% of buoyancy. This denotes a great importance of considering the Basset force in bubble motion calculations, although it is commonly neglected in the literature.

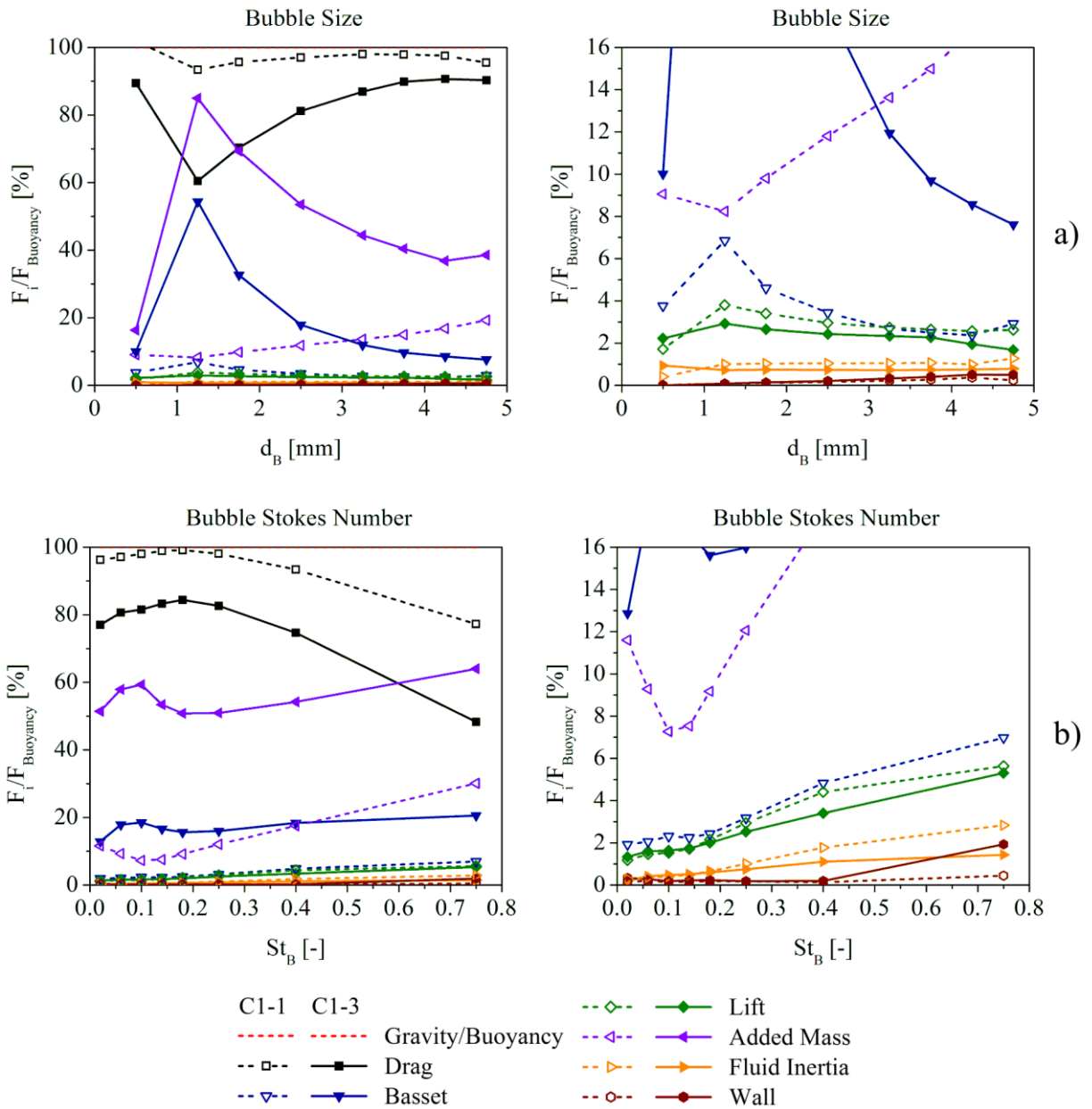


Figure 3-32: Average of resulting forces ratio from cases C1-1 and C1-3 related to bubble: a) diameter; b) Stokes number. Left-hand side: full scale; Right-hand side: scale until 10%;

$$Q_g = 160 \text{ L/h}, d_{B,\text{mean}} = 2.55 \text{ mm};$$

Case C1-1: no oscillation,D1,L1; Case C1-3: with oscillation,D2,L1.

The results for cases C1-1 and C1-3 were also classified spatially and shown in the Figure 3-33. Here, the force ratios are related to the column height and to the wall distance. Despite weak effects from bubble injection and the free surface, drag, added mass and Basset forces are practically constant over the whole column, as seen in the Figure 3-33a. On the other hand, the lift force loses its importance with the column height, while the opposite occurs with the wall force. This is explained by the dispersion of bubbles towards the wall along their ascendance, producing a more uniform flow at the top than at the bottom of column and consequently a lower shear stress.

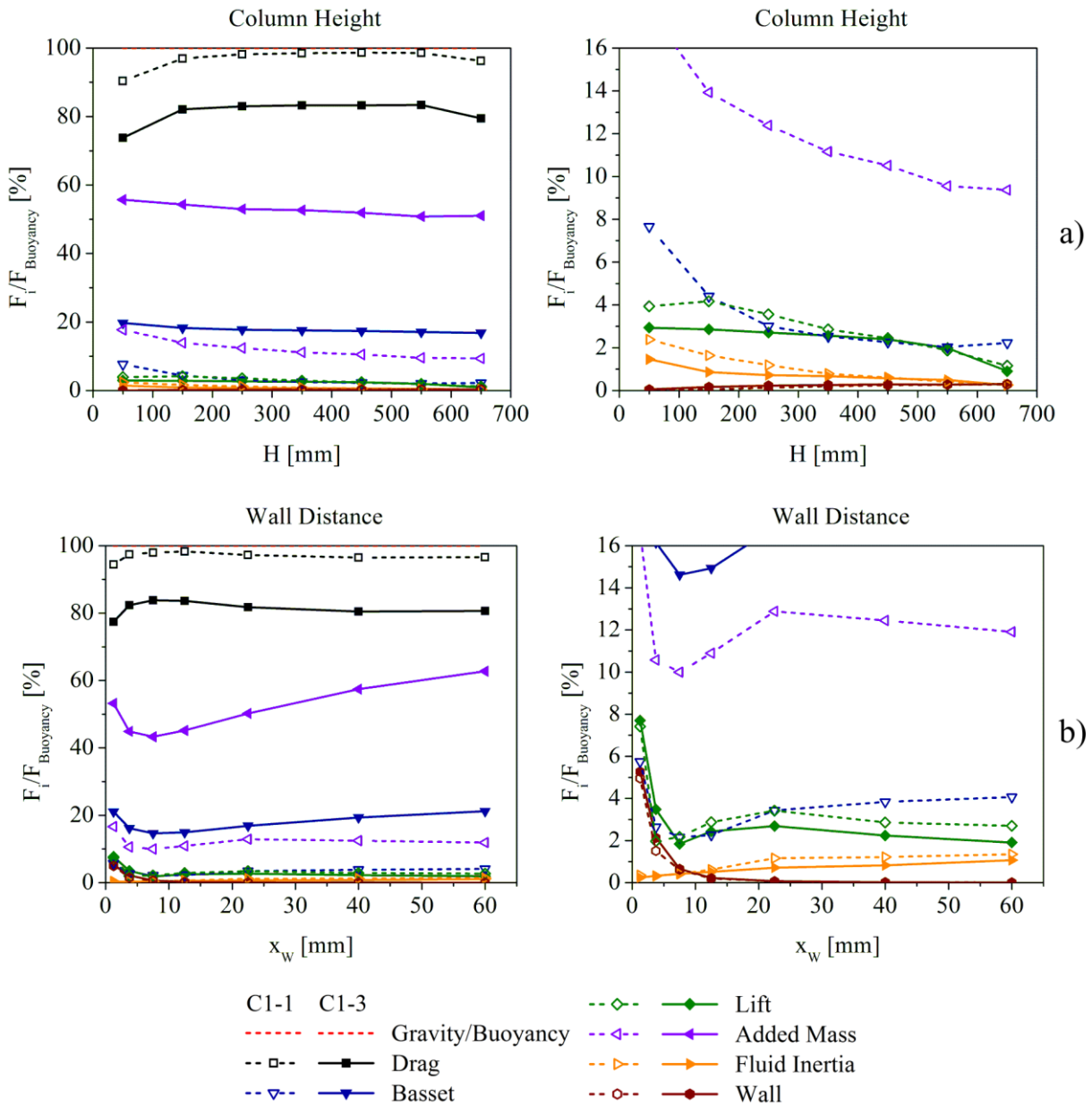


Figure 3-33: Average of resulting forces ratio from cases C1-1 and C1-3 related to:  
a) column height; b) wall distance; Left-hand side: full scale;  
Right-hand side: scale until 16%;  $Q_g = 160$  L/h,  $d_{B,mean} = 2.55$  mm;  
Case C1-1: no oscillation, D1, L1; Case C1-3: with oscillation, D2, L1.

A fair evaluation of the wall force needs to be realized over the wall distance, though. For the range of bubble size present in this case, the wall force starts to act around a distance of 20 mm and grows exponentially up to a magnitude of 5% of buoyancy, which is equivalent to the lift magnitude in this region, as seen in the Figure 3-33b. Such result is somehow expected, once the wall force is a virtual force to represent effects on lift and drag in a bounded flow, e.g., the vicinity of a wall. Additionally, the formulation for the added mass used in this work predicts also a modification of the resistance coefficient in this region (Eq. (2-26)), which is reflected in the results. Furthermore, the drag and Basset forces were

influenced by the presence of a wall, either. However, a resulting enhancement or reduction of these forces comes merely from the different flow conditions at this region, since the wall distance is not included in the correlations.

In the Figure 3-34 a comparison is made for cases where the same gas flow rate is injected in the column, yet through different capillaries thickness, producing larger bubbles. As seen in the Figure 3-34a, the resulting drag, added mass and Basset forces from cases C1-4 and C2-4 are practically equal. Due to distinct bubble size distribution and according to Eq. (2-39), the lift coefficient in the case C2-4 is expected to be slightly weaker. On the other hand, since the equal volume of gas is there represented by almost the half number of bubbles, higher local shear rates are produced, which enhance the lift force for bubbles of same size. Consequently, more intense fluid accelerations should be locally observed than in the case with smaller bubbles, increasing the fluid inertia force (substantive derivative in Eq. (2-14)), as noticed in the Figure 3-34a.

The spatial evaluation of cases C1-4 and C2-4 is shown in the Figure 3-35. Note that full qualitative agreement of forces ratio is carried out from unequal bubble size distributions. Nevertheless, as seen in the Figure 3-34a, the magnitudes of forces in these cases are equivalent for each individual bubble diameter. Therefore, if the average is performed for the whole size spectrum, as did in the Figure 3-35, the quantitative discrepancies founded here are merely an issue of statistics.

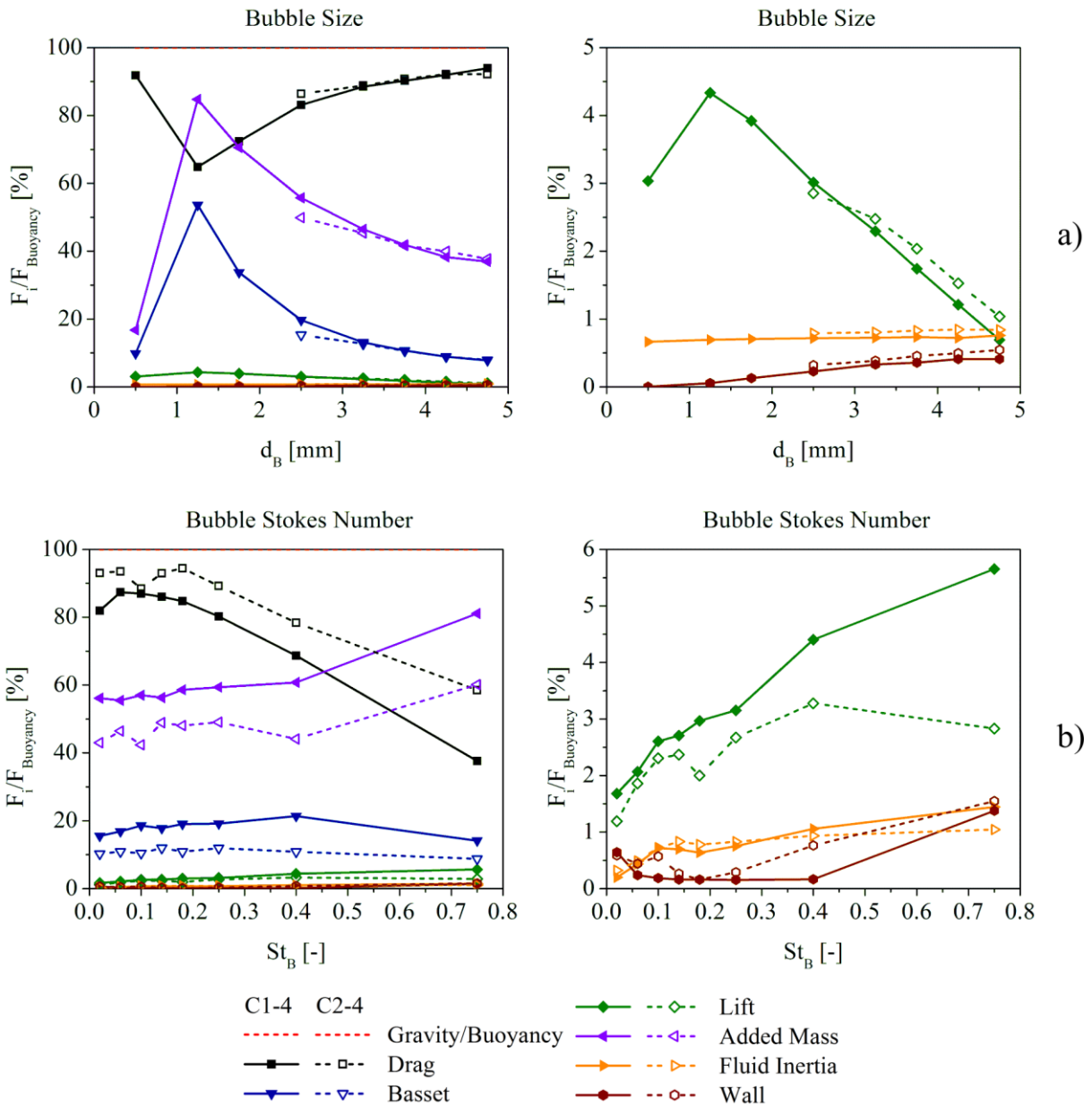


Figure 3-34: Average of resulting forces ratio from cases C1-4 and C2-4 related to bubble:  
 a) diameter; b) Stokes number. Left-hand side: full scale;  
 Right-hand side: scale until 6%;  $Q_g = 160 \text{ L/h}$ ;  
 Case C1-4: with oscillation, D2, L2,  $d_{B,mean} = 2.55 \text{ mm}$ ;  
 Case C2-4: with oscillation, D2, L2,  $d_{B,mean} = 3.31 \text{ mm}$ ;



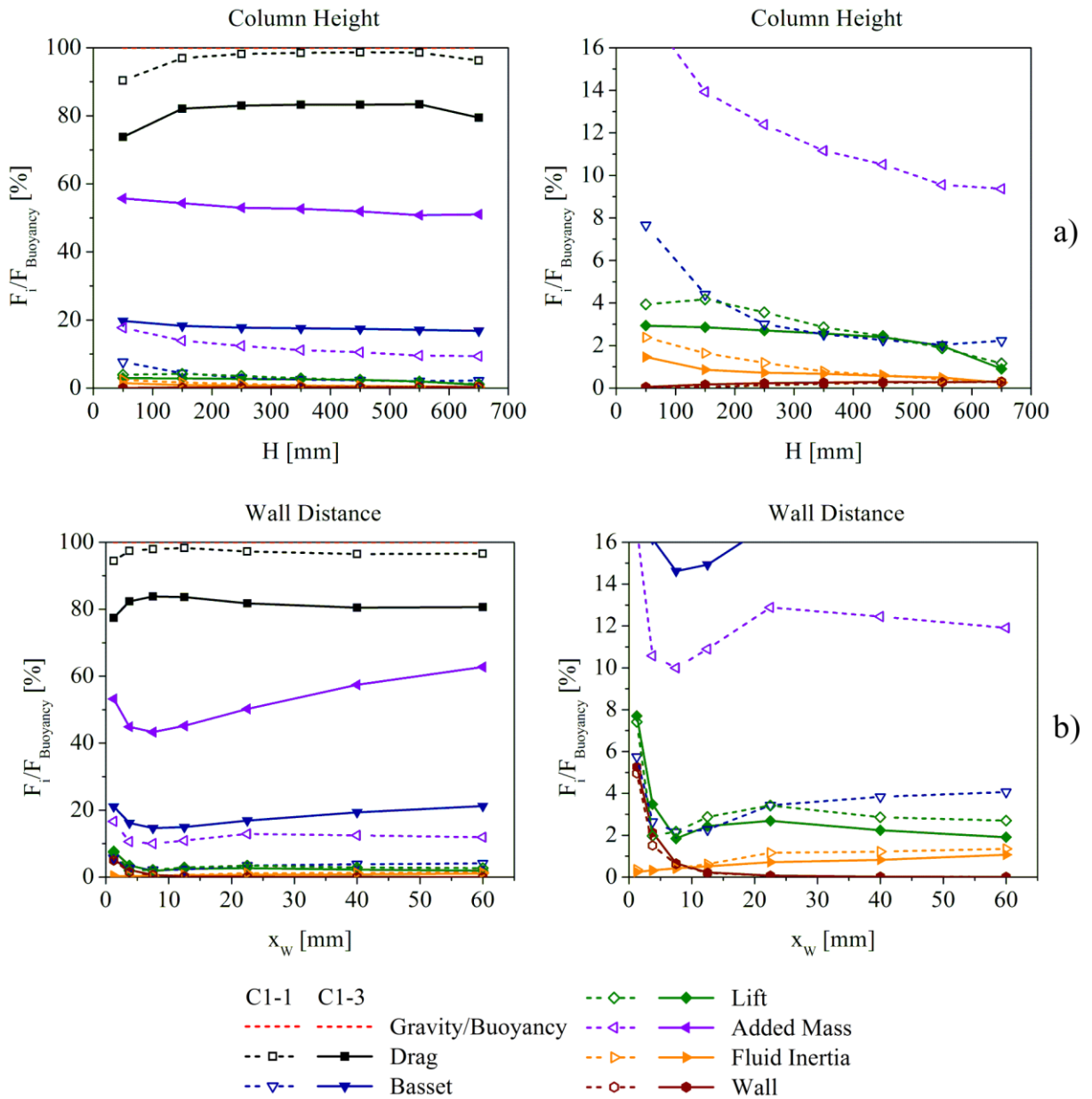


Figure 3-35: Average of resulting forces ratio from cases C1-4 and C2-4 related to:  
 a) column height; b) wall distance. Left-hand side: full scale;  
 Right-hand side: scale until 16%;  $Q_g = 160 \text{ L/h}$ ;  
 Case C1-4: with oscillation, D2, L2,  $d_{B, \text{mean}} = 2.55 \text{ mm}$ ;  
 Case C2-4: with oscillation, D2, L2,  $d_{B, \text{mean}} = 3.31 \text{ mm}$ ;

### 3.3.3 Overall radial contribution

For a further understanding of the results from cases C1-3 and C1-4, the evaluation of forces competition will be shown accounting for forces direction. In order to do so, all stored samples from each case were first classified into different axial and radial positions. After that, the radial components of lift, Basset and wall forces were extracted and averaged according to the Eq. (3-6), insomuch as the positive and negative contributions could cancel

each other. In this framework, the resulting profiles of these forces in the radial direction are seen in the Figure 3-36, in which the left-hand side is correspondent to the case C1-3 (lift model 1) and the right-hand side to the case C1-4 (lift model 2).

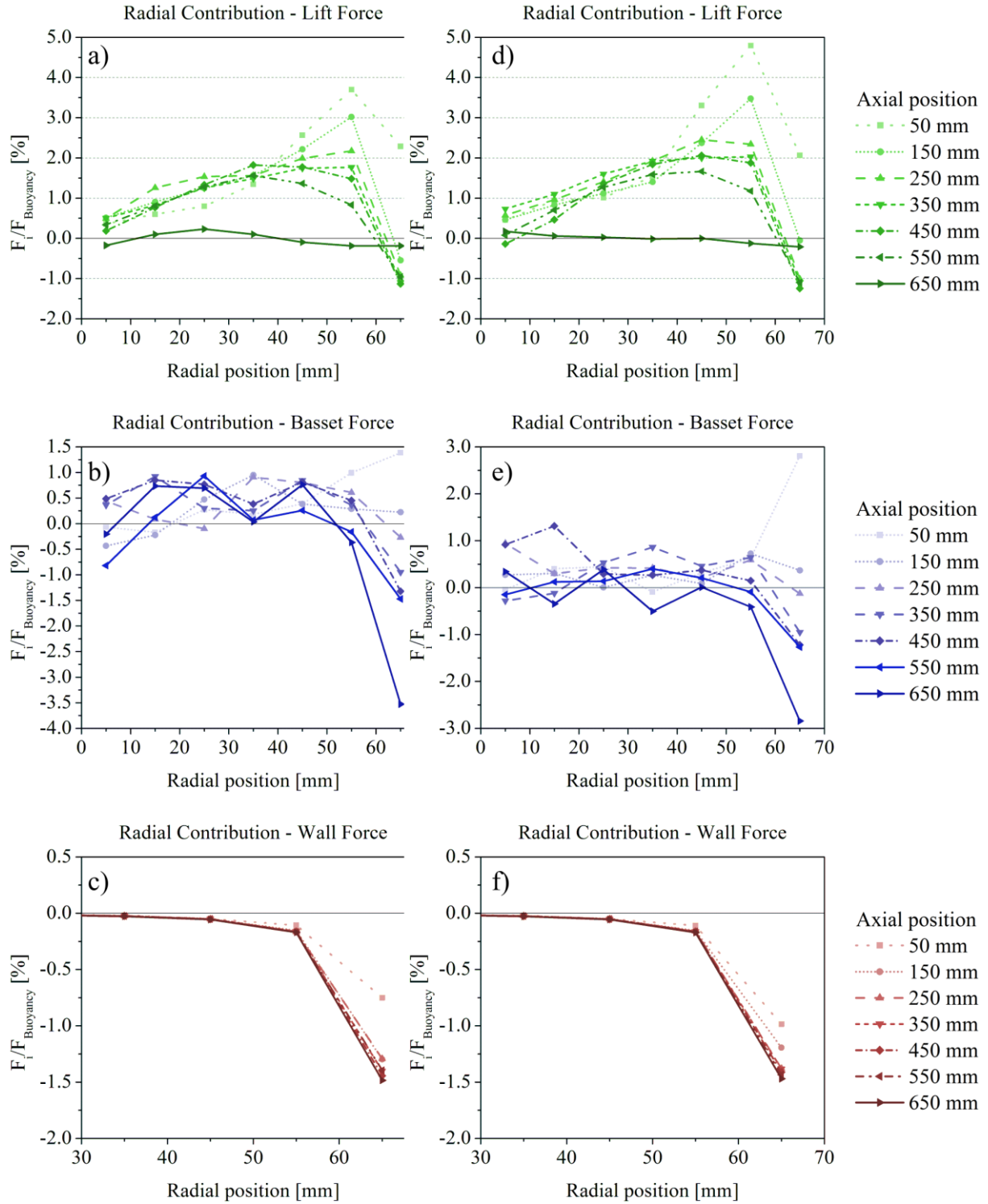


Figure 3-36: Average of radial contribution from lift, Basset and wall forces:  
 a, b, c) Case C1-3; d, e, f) Case C1-4;  $Q_g = 160$  L/h;  $d_{B,mean} = 2.55$  mm;  
 Case C1-3: with oscillation,D2,L1;  
 Case C1-4: with oscillation,D2,L2;

As expected from the positive lift coefficients for the bubble size distribution, a positive lateral lift force is founded in both cases. Nevertheless, the apex tends to be at the vicinity of the column walls, where the highest shear rates are produced, i.e., between the upstream and downstream. Further closer to the wall, the radial contribution of the lift force reverses its sign, due to the opposite direction of the downstream, although the lift coefficient remains positive. Comparing the cases C1-3 and C1-4, a significant increase of this force is noticed in the first cross-sections, as seen in the Figure 3-36d. Once the bubbles are more dispersed at higher axial positions, the transversal lift loses its initial strength, yet an averaged contribution around 0.5% of buoyancy is maintained in all the cross-sections.

The magnitude of Basset force presented to be around 20% of buoyancy, the strong oscillations in the radial direction produce a certain balance and a mean value less than 1% of buoyancy in founded, as seen in the Figure 3-36b and e. Although a trend for this force is not as clear as for the transversal lift, the overall contribution is mostly positive (towards the wall). This means that an enhancement of bubble dispersion due to the history term is expected, either, and should not be neglected. In order to further evaluate the effect of the Basset force on particles dispersion, a simpler test case is used and will be shown later in the present work.

The resulting contribution of wall force is intuitive and straightforward, since based on the model used here [39], this force acts only normal to the wall. Nevertheless, the values at the wall vicinity are around 1% of buoyancy magnitude, which is comparable to the lift and Basset forces, as seen in the Figure 3-36. In both cases C1-3 and C1-4, a lower magnitude of wall force is noticed in the first cross-sections in comparison with higher positions. One reason for that may be effect of injection and low residence times, insomuch as the bubble did not reach the terminal rise velocity yet. Another reason could be merely statistics, in which the bubbles are not fully dispersed in the column and only few bubbles are approaching the wall in this region. Jeong and Park [40] noticed that the presence of a wall does affect not only the transversal lift and drag forces, but also the behaviour of bubble oscillations. Although an extensive evaluation of bubble trajectories in the wobbling regime was performed, unfortunately no correlation was provided by the authors, which could be applied here.

In the present work, the forces competition in a laboratory bubble column was shown in terms of magnitude and radial component. Although interesting results was founded in the radial direction, the analogue evaluation in the tangential direction revealed a complete

symmetry ( $\overline{F_{l,t}} \rightarrow 0$ ) for all forces in all regions. Thus, the swirl from the bubble swarm did not afford a preferential direction under the applicability of the present model.

## 3.4 Basset Force and Dispersion

In order to expose the effect of the Basset force on particles dispersion, the experiments from Calabrese and Middleman [69] were used as study case.

### 3.4.1 Cases descriptions and setup

Their apparatus consists in a developed turbulent pipe flow, in which single droplets were injected through a capillary in the centre and traced photographically along a certain distance. The pipe has a diameter of 51mm and the measurement section extends through 400mm from the particle injections. The system was operated downstream with water in a Reynolds number of 24,500. Three fluids were used for the droplets, with the purpose to obtain situations where the point-particles are heavier than water (carbon tetrachloride – CCl<sub>4</sub>,  $\rho=1595 \text{ kg/m}^3$ ), neutrally dense (butyl benzoate – BB,  $\rho=1000 \text{ kg/m}^3$ ) and buoyant (*n*-heptane – Hep,  $\rho=695 \text{ kg/m}^3$ ). The radial dispersion was evaluated measuring at least 300 droplets in each case.

In this work, simulations were conducted as simple as possible, in order to isolate the effect of forces taken into account. In this manner, the axial velocity profile was considered constant, as follows:

$$U = U_0 \left(1 - \frac{y}{R}\right)^{1/6} \quad (3-7)$$

where  $U_0$  is the maximal velocity in the centre (in this case,  $U_0=0.62 \text{ m/s}$ ),  $y$  is the radial position and  $R$  is the pipe radius. The turbulent kinetic energy and its dissipation rate, required for the dispersion model, were calculated using the following equations:

$$k = \frac{1}{2} (\overline{u'u'} + \overline{v'v'} + \overline{w'w'}) \quad (3-8)$$

$$\varepsilon = c_\mu^{0.75} \frac{k^{1.5}}{l_\varepsilon} \quad (3-9)$$

$$c_\mu = 0.09 \quad (3-10)$$

where  $\overline{u'u'}$ ,  $\overline{v'v'}$  and  $\overline{w'w'}$  are the normal Reynold stresses on the vertical and two horizontal directions, respectively, and  $l_\varepsilon$  is the mixing length. The used values for the Reynolds stresses

were given by Sommerfeld [70] making use of experimental data from Laufer [71], and the mixing length can be calculated according to Schlichting [72], as follows:

$$\frac{l_{\varepsilon}}{R} = 0.14 - 0.08 \left(\frac{y}{R}\right)^2 - 0.06 \left(\frac{y}{R}\right)^4 \quad (3-11)$$

In this framework, the fluid oscillations seen by the particles come only from the turbulent dispersion model and it is independent of grid, once all these properties can be calculated directly in the particle level.

The particle tracking was performed numerically for 5000 samples and five cases were arbitrary chosen for each situation described above, as seen in the Table 3-4. The used droplets sizes for CCl<sub>4</sub>, BB and Hep were constant and equal to 706, 862 and 809 μm, respectively.

Table 3-4: Forces considered in the pipe flow simulations

	Gravity/ Buoyancy	Drag	Added Mass	Basset	$N_{window}$
Case D1	x	x			
Case D2	x	x	x		
Case D3	x	x	x	x	10
Case D4	x	x	x	x	100
Case D5	x	x	x	x	Full history

According to Calabrese and Middleman [69], the droplets injection in the system should be made isokinetically to the fluid flow, although deviations were observed or sometimes necessary. In order to include this factor on the simulations, the initial particle velocity  $\mathbf{u}_{p0}$  was calculated with the following equation:

$$\mathbf{u}_{p0} = [U_0 + \zeta \bar{u}', \zeta \bar{v}', \zeta \bar{w}'] \quad (3-12)$$

where  $\bar{u}'$ ,  $\bar{v}'$  and  $\bar{w}'$  are the RMS values from velocity fluctuations in the vertical and both horizontal directions, respectively, and  $\zeta$  is a linear random number with null mean value and  $-3 \leq \zeta \leq 3$ .

### 3.4.2 Results and discussion

Since a relative small number of particles were calculated, the simulations for all the 15 cases were finished in less than 30 minutes (wall-time), inclusive post-processing. At first moment, the resulting mean square displacement of particles  $\overline{y^2}$  is numerically measured along the dispersion time and compared with experimental data [69], as seen in the Figure 3-37. Comparing the cases D1 and D2, where the added mass force is additionally considered to the drag, no significant changes in terms of dispersion was founded in all the scenarios. On the other hand, the inclusion of Basset force in the cases D3-D5 revealed a clear enhancement of particle dispersion, mainly for the neutrally dense particles, as seen in the Figure 3-37b. A deviation between the results in cases with and without the Basset force does not appear after some time, but since the beginning of dispersion. From around 0.3s to the end of evaluation time, the lateral displacement seems to increase linearly, which agrees with Taylor's [73] theory at large dispersion times. The resulting slopes in this region are very similar to each other, either considering Basset force or not, yet delayed in time. This reflects an effect of particle initial conditions, sustained by the history term and rapidly "forgotten" when only drag and added mass are considered. These results denote a great importance of the Basset force in Euler/Lagrange calculations irrespective of density ratio, even for a very simple situation.

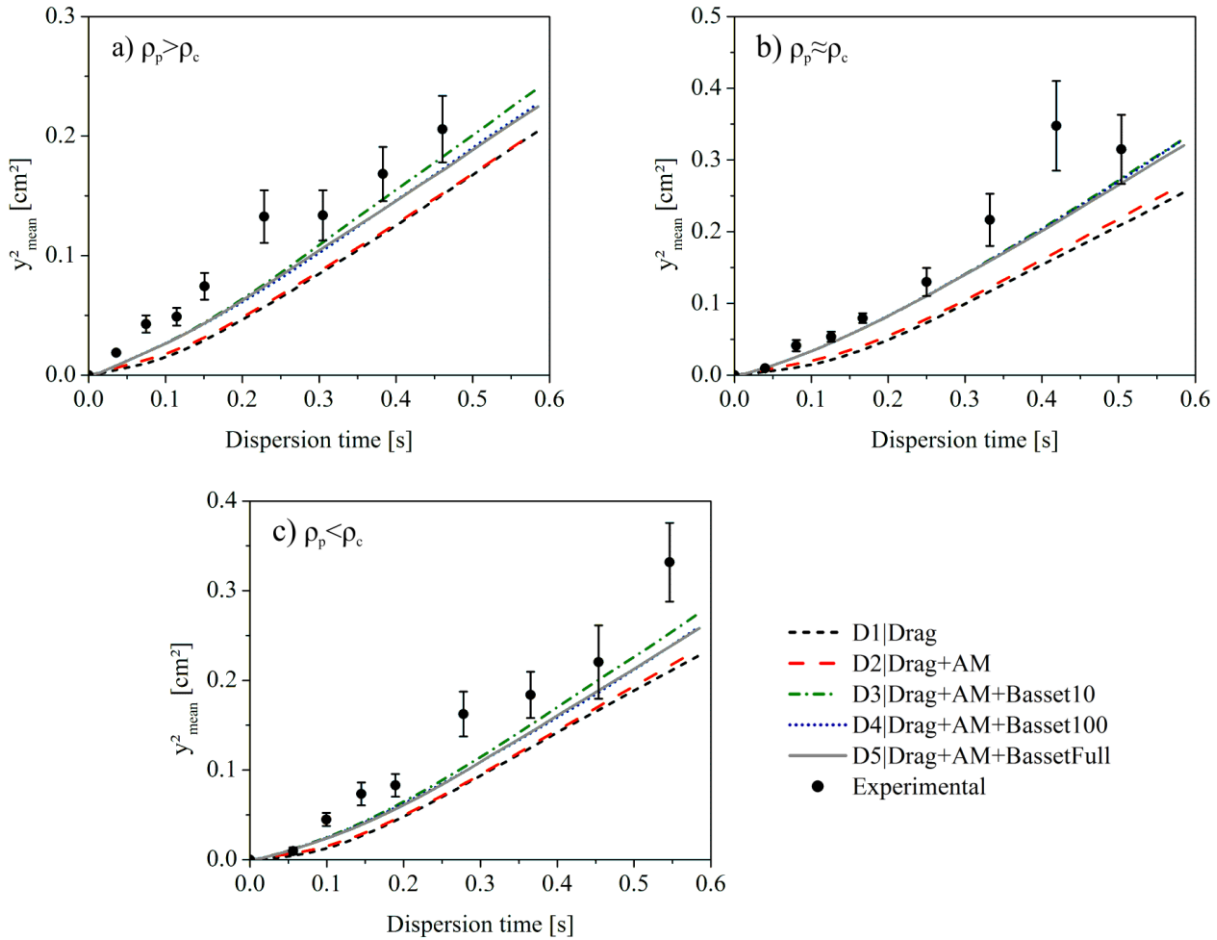


Figure 3-37: Comparison of resulting lateral displacement with experimental data [69] considering different forces for cases: a) CCl<sub>4</sub>; b) BB; c) Hep.

According to Calabrese and Middleman [69], the sizes of these particles are large enough to disturb the flow around them and produce a wake, although they are smaller than the Lagrangian integral length scale. In the case of buoyant particles, their terminal velocity is lower than the fluid flow, which causes them to be convected into their own wake. Thus, a higher dispersion is expected in this case than for particles of same inertia and heavier than the fluid. Such “wake effect”, as called by the authors, cannot be attained in the simulations presented here, since a one-way coupling was assumed. After all, satisfactory results were obtained for all the cases.

A further investigation of these test cases is realized numerically in terms of average and fluctuation velocities. The resulting profiles of both fluid and particles at 300mm after the injection are shown for the streamwise and radial directions, as seen in the Figure 3-38 and Figure 3-39, respectively. As obviously expected, the resulting particle terminal velocities differ from the fluid averaged due to gravity and buoyancy forces. In the first scenario, for example, the particles are heavier than the fluid, and consequently, a higher terminal velocity



is found. In the third scenario, the opposite behaviour is naturally observed. The interesting part is that although different dispersions were obtained by considering (cases D3-D5) and neglecting (cases D1 and D2) the Basset force, practically the same particles averaged velocities were found in all the cases.

Unlike the average velocities, the particle fluctuations from cases D1 and D2 are clearly smaller than the fluid oscillations. This is explained by the particle inertia, insomuch as the particles do not respond to the fluid instantly, also called as relaxation time. Additionally, the inclusion of the Basset force in the case D5 reveals a further reduction of particle fluctuating velocities, acting as a resistance for the motion change. Such effect is more accentuated in the radial direction, as seen in the Figure 3-39. This behaviour is not intuitive, once a less turbulent flow, i.e., smaller fluid fluctuations, would produce lower particle dispersion. Thus, the explanation for having greater lateral displacement with Basset force must lie in the particle initial conditions. An initially non-zero radial component remains in the particle history term and is carried during its whole trajectory, affording a mostly positive integration of this force towards the pipe wall and consequently, a higher overall dispersion.

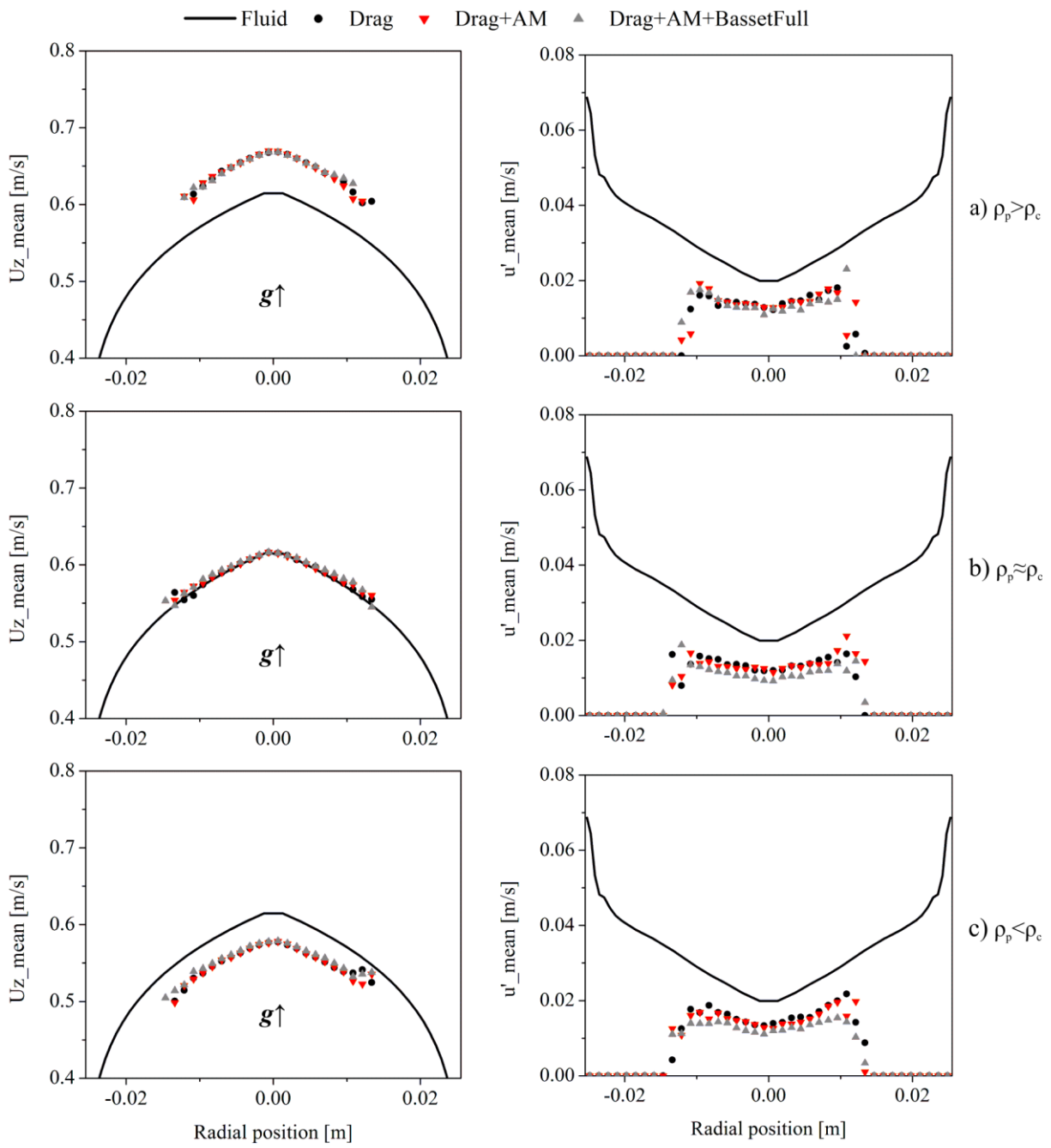


Figure 3-38: Average and fluctuating velocities in the streamwise direction for cases:  
a)  $\text{CCl}_4$ ; b) BB; c) Hep.

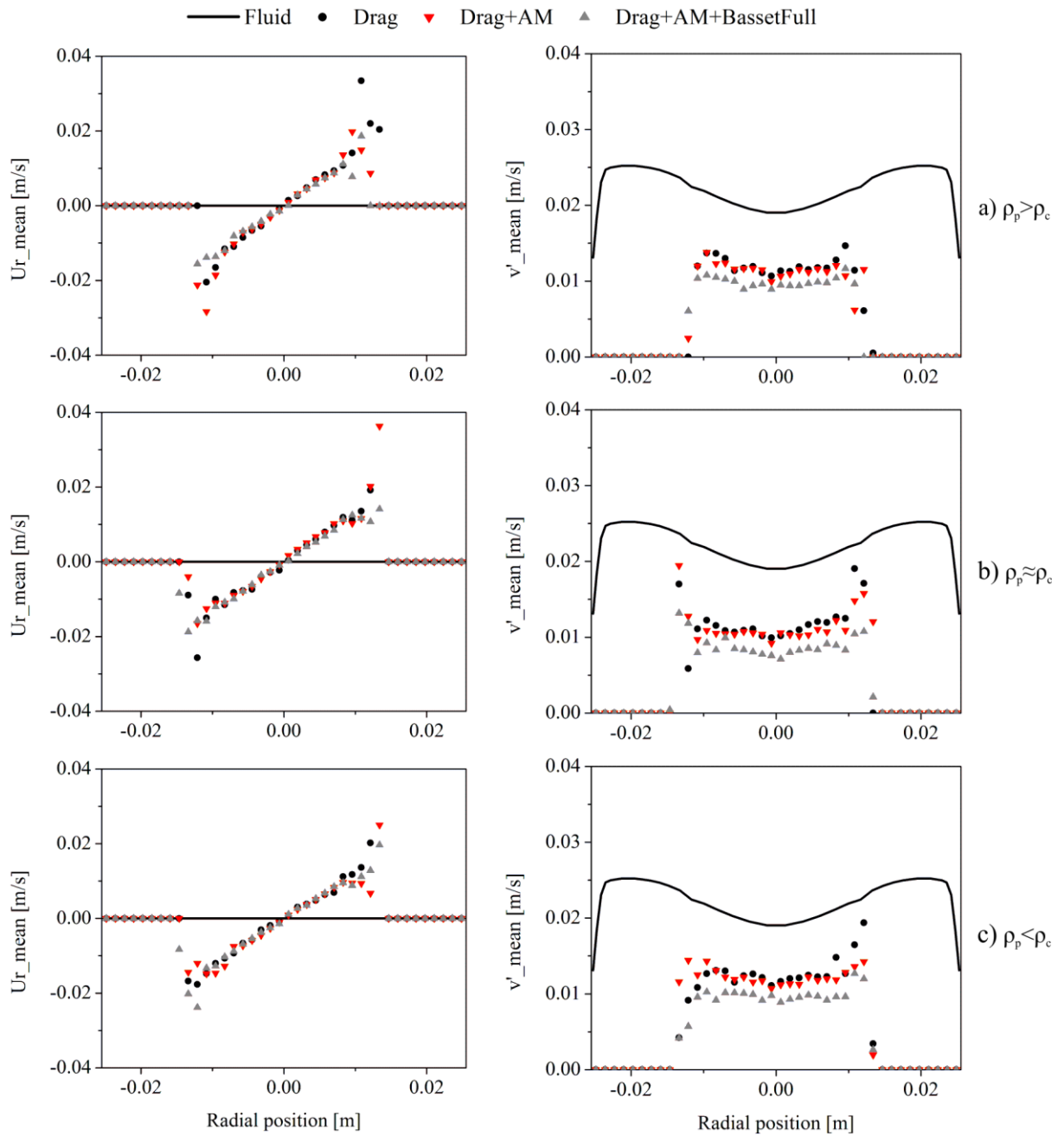


Figure 3-39: Average and fluctuation velocities in the radial direction for cases: a)  $\text{CCl}_4$ ; b) BB; c) Hep.

### 3.5 Bubble Swarms – Study Case II

The previous study case [56], presented in the section 3.2, consisted in a laboratory circular bubble column filled with distilled water. The superficial gas velocity was  $j_g \cong 0.00289$  m/s, represented by two bubble size distributions with mean diameters of 2.55 and 3.31 mm. In order to evaluate the model for different geometries and also larger bubble sizes, the results of Mohd Akbar et al. [54] were used as study case, as described in the following.

#### 3.5.1 Cases descriptions and setup

The case [54] consists in a rectangular bubble column (72 x 240 mm<sup>2</sup>) with an initial tap water level of 700 mm. The bubble injection is made through 35 needles distributed in the bottom and two different superficial velocities were evaluated ( $j_g = [0.003, 0.013]$  m/s). The resulting bubble size distributions are shown in the Figure 3-40 and the correspondent mean bubble diameters are 4.3 mm and 5.5 mm, respectively. In this manner, the smaller superficial gas velocity  $j_{g1} = 0.003$  m/s is similar to the previous study case, but is expressed by even fewer bubbles. Besides, in the second case ( $j_{g2} = 0.013$  m/s) bubble diameters up to 8 mm are found, which can be challenging for the “point-mass” approximations. According to the authors, the PDF of bubble size for this very case is broader at  $z = 0$  m than at  $z = 0.5$  m, but the difference is not significant. Coalescence and break-up phenomena may be there occurring, although here they will be neglected and are not within the purposes of this work.

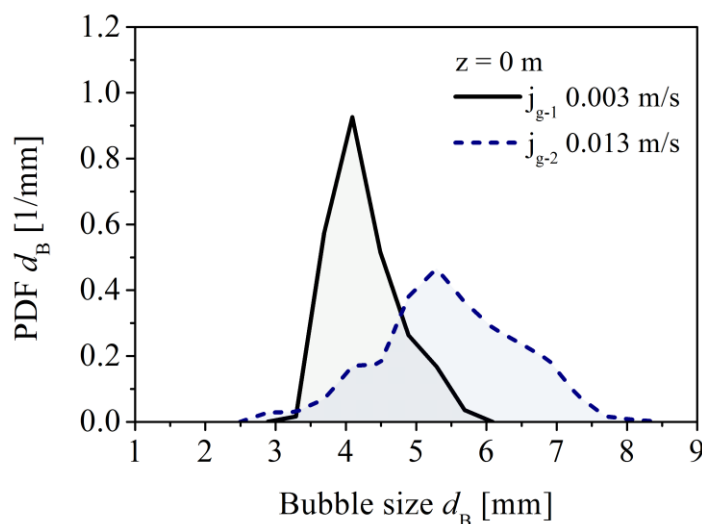


Figure 3-40: Bubble size distribution from different gas superficial velocities.  $\bar{d}_B \cong [4.53, 5.55]$  mm. Source: adapted from Mohd Akbar et al. [54].

An initial numerical grid consisting of 12,000 volumes in total was used for simulations of both cases, in which the cross-section has 150 volumes and the column height is subdivided in 80 elements, as seen in the Figure 3-41.

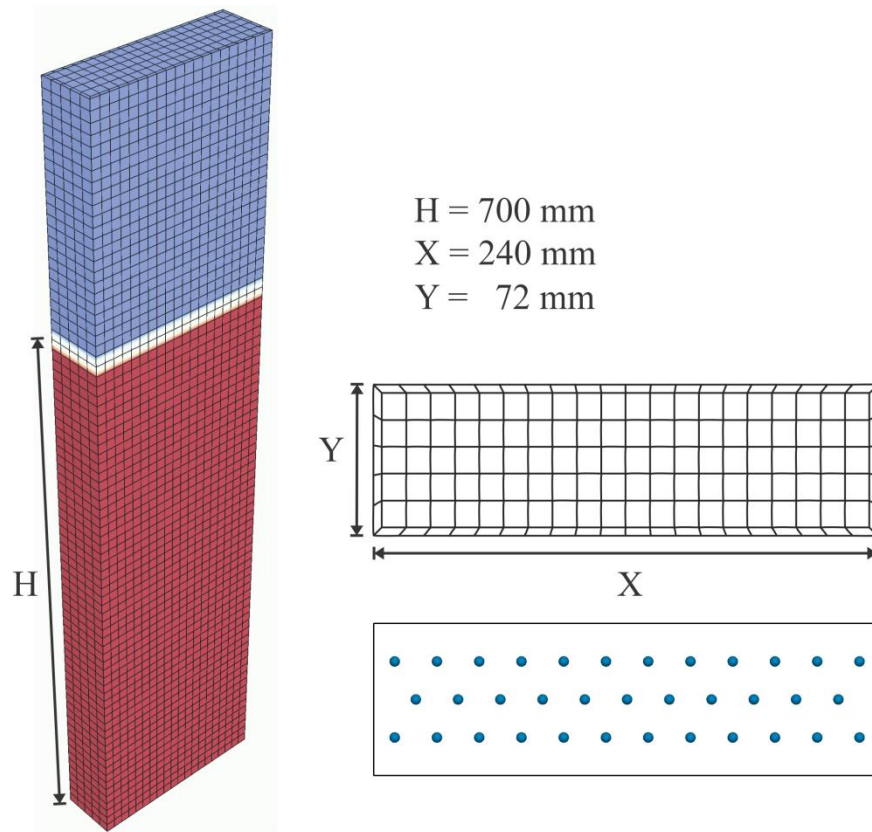


Figure 3-41: Initial numerical grid used in the simulations and bubble injection positions. 12,000 volumes in total (8,400 for the liquid part), 150 volumes per cross section and 80 along the height.

Due to different geometry and bubble size distributions, the flow structure has other behaviour than in the cases from Sommerfeld and Bröder [56]. In this manner, the simulations were here performed for 120 seconds for flow stabilization and statistics was sampled until 750 or 1000 seconds for reaching the symmetry, depending on the case. For the sake of brevity, only the model setups equivalent to Cases 4 and 6 in Table 3-2 (p. 34) will be evaluated here. These cases correspond to the model without and with bubble dynamics, respectively, and will be called here as “M-” and “M+”, as described in the Table 3-5. The Eulerian time-step was set constant for all the cases and equal to  $\Delta t_E = 5 \text{ ms}$ .

Table 3-5: Cases description for different simulations.  $j_g = [0.003; 0.013]$  m/s.

	$j_g$ [m/s]	All Forces	Drag	Lift	2-way coupling	TDM	BIT	OM	$\bar{d}_B$ [mm]	$\frac{\bar{d}_B}{\bar{\Delta x}}$	$\frac{d_{B,max}}{\bar{\Delta x}}$
Case M1-	0.003	x	D1	L2	x	x	x		4.53	0.38	0.50
Case M1+	0.003	x	D2	L2	x	x	x	x	4.53	0.38	0.50
Case M2-	0.013	x	D1	L2	x	x	x		5.55	0.47	0.69
Case M2+	0.013	x	D2	L2	x	x	x	x	5.55	0.47	0.69

L2  $\equiv$  Eq. (2-39)

Since tap water was used in the experiments, some adaptations in the model were required. The first approach of the drag coefficient (“D1” – Eq. (2-15)) was modified for contaminated systems [24], as follows:

$$C_D = \max \left[ \frac{24}{Re_B} (1 + 0.15 Re_B^{0.687}), \frac{8}{3} \frac{Eo}{Eo + 4} \right] \quad (3-13)$$

For the second approach (“D2” – Eq. (2-21)), on the other hand, the pre-coefficient of the drag coefficient dependent on Reynolds number in Eq. (2-17) was changed from 16.0 to 24.0, as follows:

$$C_{D,Re,\chi} = \frac{24}{Re_B} \left\{ \frac{1 + \frac{8}{15}(\chi - 1) + 0.015(3G_\chi - 2)Re_B}{1 + 0.015Re_B} + \left[ \frac{8}{Re_B} + \frac{1}{2} \left( 1 + \frac{3.315H_\chi G_\chi}{\sqrt{Re_B}} \right) \right]^{-1} \right\} \quad (3-14)$$

Furthermore, the bubble eccentricity in contaminated systems can differ from that in clean liquids. In this framework, the correlation proposed by Loth [58], making use of a vast compilation of data available in the literature, is suitable for the range of application in these cases, as follows:

$$\bar{\chi} = [1 - 0.75 \tanh(0.11 We_B)]^{-1} \quad (3-15)$$

$$We_B = \frac{\rho_L |\mathbf{u}_L - \mathbf{u}_B|^2 d_B}{\sigma} \quad (3-16)$$

Note in the Eq. (3-15) that the hyperbolic-tangential function gives an upper limit to the bubble eccentricity for greater Weber numbers. In this manner, the correlation is shown in the Figure 3-42, as follows:

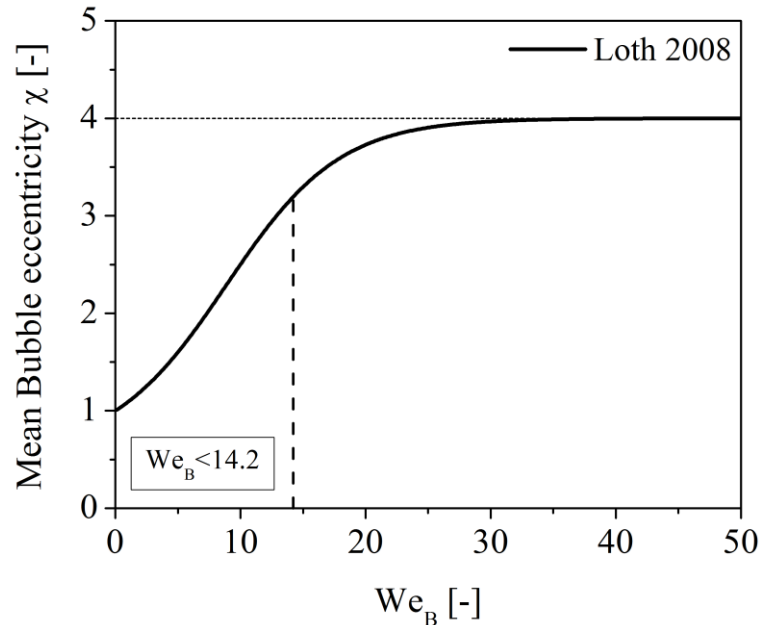


Figure 3-42: Eccentricity correlation [58] in function of Weber number for contaminated systems; Horizontal point line: upper limit from the correlation; Vertical dashed line: max. Weber number expected in the study cases in evaluation.

Due to the lack of data for the RMS values of bubble eccentricity for contaminated systems, the correlation from Sommerfeld and Bröder [56] (Eq. (2-67)) was also used in the simulations for this study case.

### 3.5.2 Prior results and further model adaptations

The data provided by Mohd Akbar et al. [54] corresponds to a measurement section at a height of 500 mm, in which a symmetry was assumed, showing the results only for one half of the bubble column.

As a prior analysis, the colour fields in terms phase's velocities and bubble volume fraction are shown in the Figure 3-43 for the Case M1+, in which the complete model is considered, as follows:

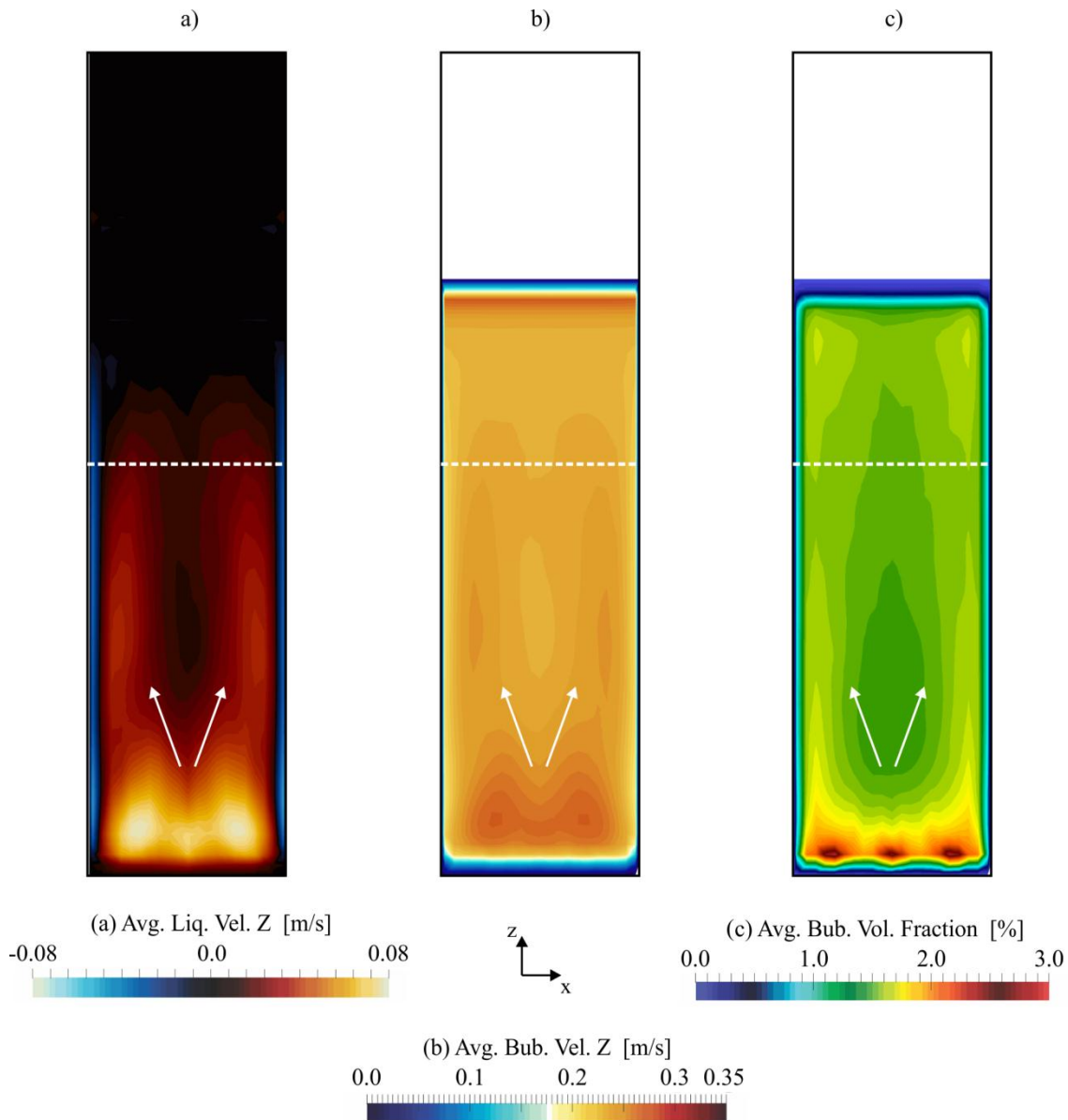


Figure 3-43: Colour fields of Case M1+ with regard to average: a) liquid velocity; b) bubble velocity; d) bubble volume fraction.  $j_g = 0.003$  m/s.  $\bar{d}_b = 4.53$  mm.  
Dashed white line: measurement section at 500 mm.

The results in the Figure 3-43 reveal that instead of one typical core flow, two preferential flows were formed in this geometry, indicated there by the arrows. However, such behaviour was not observed experimentally [54]. Nevertheless, a comparison with experimental data was performed, as seen in the Figure 3-44.



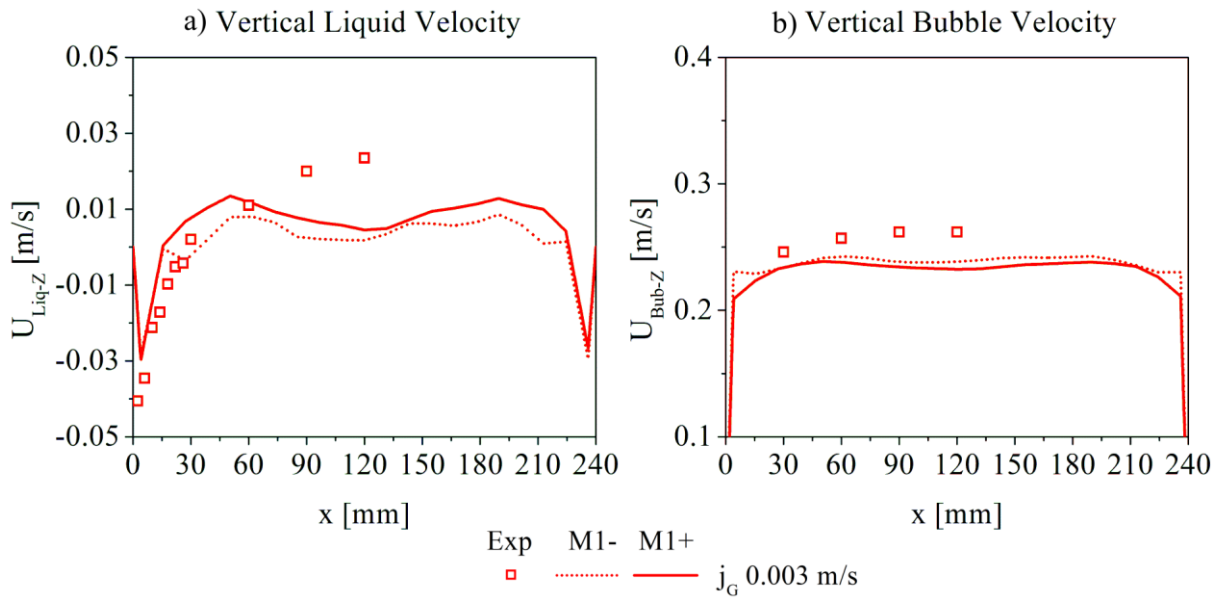


Figure 3-44: Comparison of numerical and experimental data [54] in axial position 500 mm: a) liquid vertical velocity; b) bubble vertical velocity.  $j_g = 0.003$  m/s,  $d_{B,mean} = 4.53$  mm.

Note in the Figure 3-44a that the liquid velocity is overestimated at the vicinity of the column wall and underestimated at the centre. Additionally, the bubble velocity in the Figure 3-44b is underestimated in both cases through the whole measurement line, as some resistance have been applied to the bubbles, whose reason is so far unclear. Moreover, the numerical resolution of the continuous phase is poor and high velocity gradients are notable close to the wall.

This study case denotes a challenge for “point-particles” approximation, in which large bubbles are confined in a thin geometry (in the  $y$ -direction, see Figure 3-41). While a coarse mesh is created with purpose to maintain a control volume greater than the bubble size, a finer grid is desired for having a better resolution for the continuous phase. The simplest solution to avoid numerical divergence in a finer mesh would be neglect the effective density in the momentum equations ( $\alpha_B = 0$ ). A second possible solution would be numerically limiting the volume of bubbles seen by the continuous phase (e.g.  $\max(\alpha_B) = 0.4$ ). This avoids divergence, indeed, however, some information is still lost on the way and the results are not reliable. A third option is proposed by distributing the volume of bubbles not only to the owner cell, i.e. the cell including the bubble centroid, but also to its neighbours. In this manner, the field of bubble volume fraction is smoothed, but the total account of effective density is maintained in its whole. This matter is illustrated in the Figure 3-45.

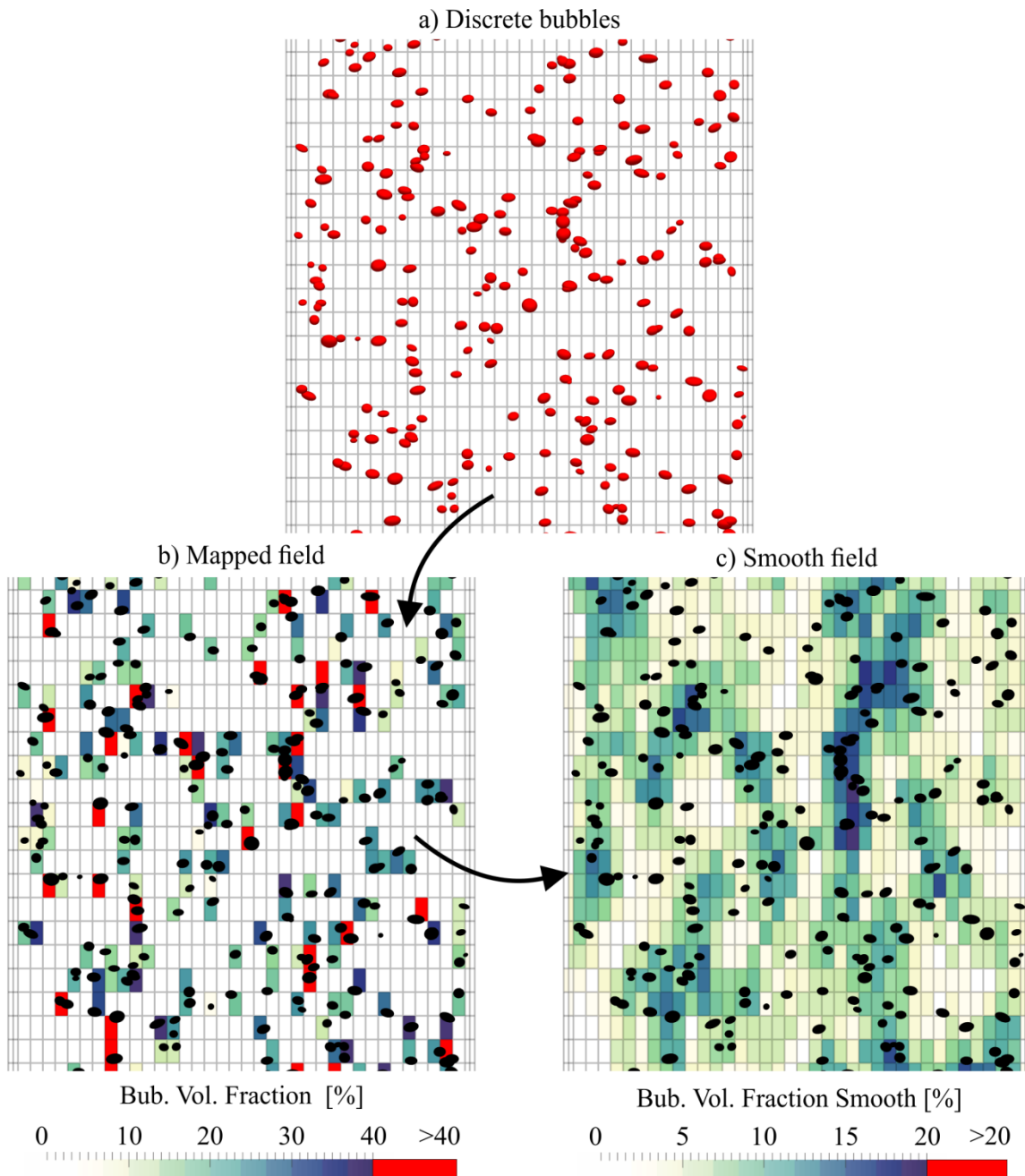


Figure 3-45: Mapping and smoothing of bubble volume fraction field.

Note in the Figure 3-45b that the mapping function applies the bubble volume to its owner cell based on the centroid. When the size of bubbles are relatively large compared to the cell size (i.e.  $d_B/\Delta x$ ), as in this example, some bubbles overlap also neighbouring cells, however, this is not accounted for. With rigor, a radius of influence should be calculated for each bubble, in order to distribute properly the volume to more than only the owner cells, proportionally to its influence. Then, only if necessary, cells above a certain volume fraction could suffer some smoothing, for example, the cells coloured in red in the Figure 3-45b. Naturally, such implementation would require a large amount of computational resources,

which falls out of the scope of this work. The not perfect, but efficient and sufficient solution was to distribute the bubble volume evenly to all neighbouring cells, independent of its exact position. In this manner, the mapping of neighbours can be done once per run, instead once per Eulerian time-step. Additionally, the level of smoothing can be adapted for each case, choosing arbitrary as neighbours three different types: the shared faces (level 1), the shared edges (level 2), and the shared points (level 3), as illustrated in the Figure 3-46.

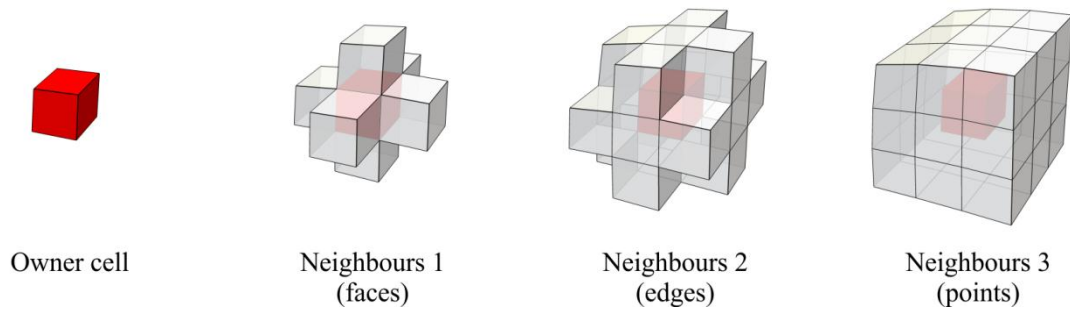


Figure 3-46: Different levels of neighbour cells.

In order to improve the results of this study case, a finer mesh and the smoothing function (level 3) was used in the simulations. The resulting mesh has in total 40,880 elements, in which each cross-section consists in 584 elements, as seen in the Figure 3-47. As consequence, the mean ratios from Table 3-5 changed to  $\overline{d_B}/\overline{\Delta x} = [0.55, 0.71]$  and the maximum ratios to  $d_{B-max}/\overline{\Delta x} = [0.78, 1.06]$  for the Cases M1 and M2, respectively.

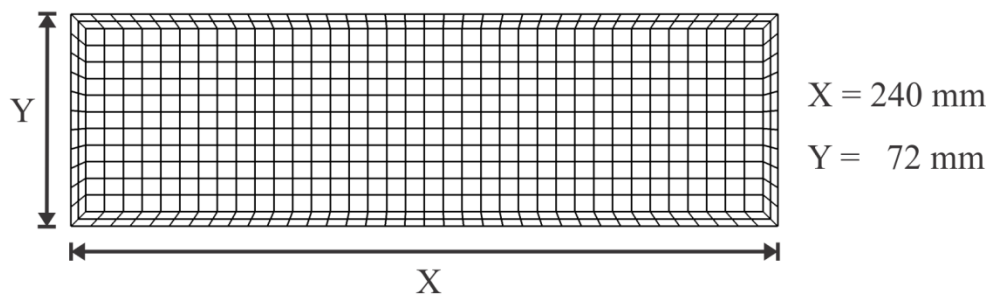


Figure 3-47: Finer mesh used in the simulations for the Cases M1 and M2. 40,880 volumes in total (28,616 for the liquid part), 584 volumes per cross section and 70 along the height.

While the Eulerian time-step for the Cases M1 was maintained  $\Delta t_E = 5$  ms without any issue, this value needed to be decreased for the Cases M2, in order to avoid divergences, inasmuch as higher Courant numbers were produced there. The arbitrary value of  $\Delta t_E = 2.5$  ms was sufficient to maintain a maximum Courant number below 0.3.

### 3.5.3 Final results and discussion

The colour fields in terms of phase's velocities and bubble volume fraction are shown in the Figure 3-48 for the Case M1+ with the new numerical grid, as follows:

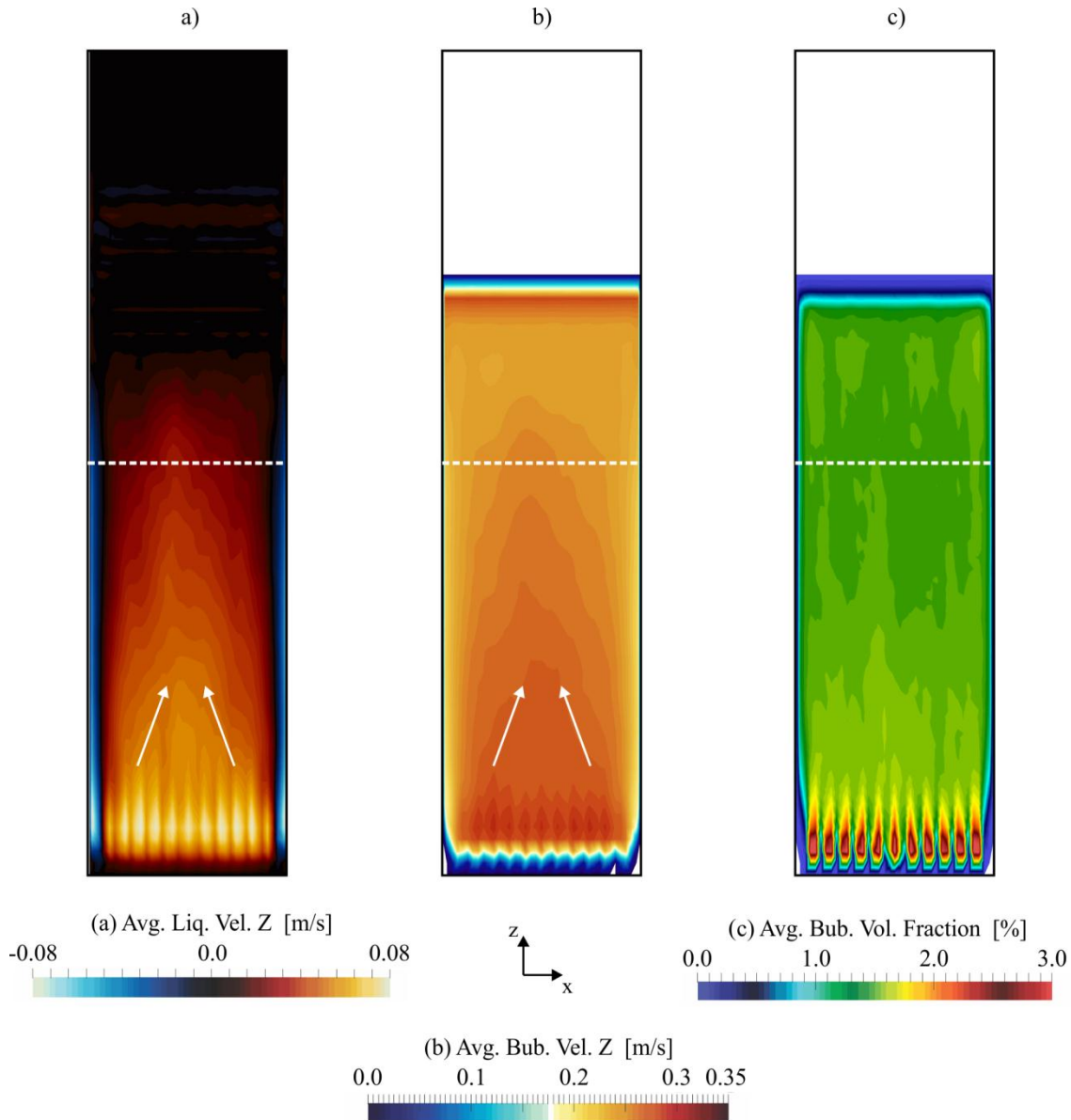


Figure 3-48: Colour fields of Case M1+ with regard to average: a) liquid velocity; b) bubble velocity; d) bubble volume fraction; Dashed white line: measurement section at 500 mm.

Case M1+: with oscillation,  $D2$ ,  $L2$ ,  $j_g = 0.003$  m/s,  $\bar{d}_b = 4.53$  mm.

As a first visual impression, due to a finer resolution in the mesh, it is now possible to note the bubble injection positions in the bottom of the column, reflected by higher velocity streams, as seen in the Figure 3-48a, and even better in the Figure 3-48c in terms of bubble volume fraction. The interesting part is that the preferential flow is now focused on the centre, as one main bubble plume, differently from the results with the coarse mesh (Figure 3-43).

The comparison of the numerical results from Cases M1- and M1+ with experimental data is shown in the Figure 3-49. Note in the Figure 3-49a and b that the Case M1-, where no bubble dynamics model is included, produced a flat profile for both phases. When bubble oscillations are considered (Case M1+), the enhanced bubble dispersion expected from the model occurs surprisingly towards the core.

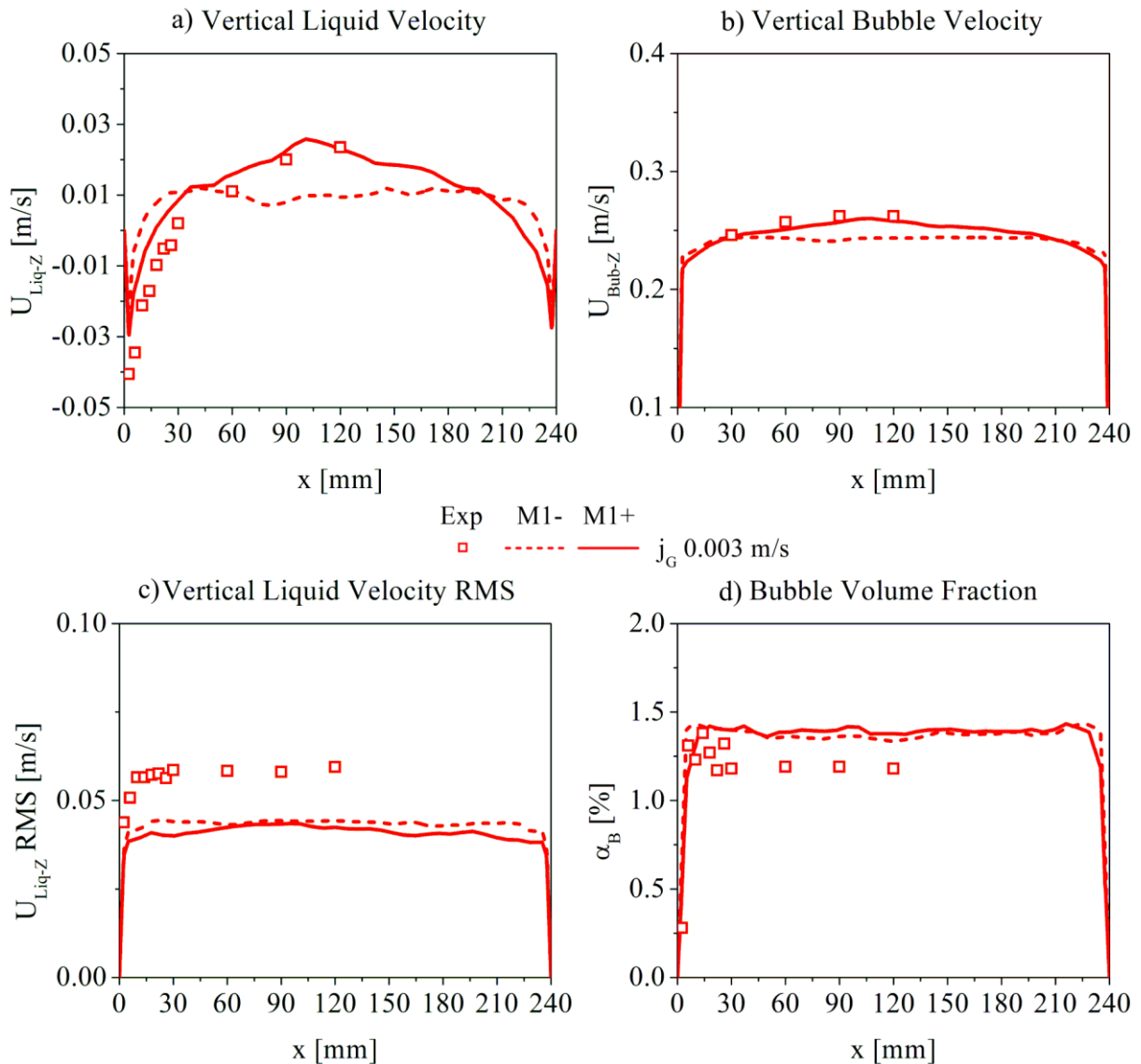


Figure 3-49: Comparison of numerical and experimental data [54] in axial position 500 mm: a) liquid vertical velocity; b) bubble vertical velocity. c) RMS values of liquid velocity fluctuations. d) Bubble volume fraction;  $j_g = 0.003$  m/s,  $d_{B,mean} = 4.53$  mm; Case M1-: no oscillation, D1, L2; Case M1+: with oscillation, D2, L2.

Although this behaviour is against our intuition, the reason lies on the geometry. While the column is wide in the  $x$ -direction (see Figure 3-41), the size in  $y$ -direction is relatively thin. Additionally, the bubble injection is well distributed over the whole cross-sectional area, differently than in the previous study case, which was concentrated in the core.

Nevertheless, if bubble dynamics is neglected (Case M1-), bubbles close the wall rise almost straight and will not return easily to the core, confined by the lift force, as expected from the results in the Figure 3-36. This matter causes a peak of bubble velocity in the profiles, as seen in the Figure 3-50, also observed in the previous study case (Figure 3-9). Thus, if bubble oscillations are imposed by the model (Case M1+), the dispersion occurs also towards the centre, benefiting a core flow. After all, the numerical results for this study case revealed a satisfactory agreement with experimental data.

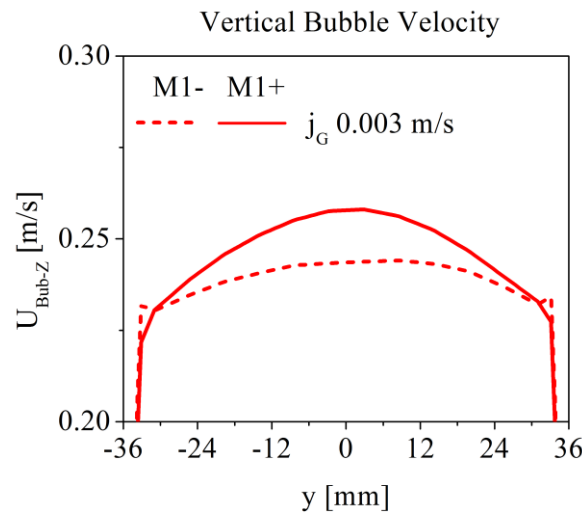


Figure 3-50: Numerical bubble vertical velocity at the axial position 500mm;  
 $j_G = 0.003$  m/s,  $d_{B,mean} = 4.53$  mm;  
 Case M1-: no oscillation, D1, L2; Case M1+: with oscillation, D2, L2.

The second case evaluated by Mohd Akbar et al. [54] consists in more than four times the previous superficial gas velocity for the same geometry. Additionally, because greater sizes of bubble are present in the Cases M2, the solution of the free surface and the continuous gas phase above it was deactivated due to strong entrainment into the liquid domain, since no surface reconstruction is performed. Such entrainment polluted the solution of the liquid phase, in which the volume fraction of continuous gas  $\alpha_G$  reached values up to 10%. Once the free surface was “frozen”, the solution for this case was obtained without numerical issues.

The resulting profiles for the Cases M2- and M2+ are compared with experimental measurements in the Figure 3-51. Note in the Figure 3-51a that values for the vertical liquid velocity are in concordance with the experiments, as well as for the velocity fluctuations in the Figure 3-51c, either considering bubble dynamics or not. Unfortunately, the same cannot be concluded for the bubble phase, as seen in the Figure 3-51b. Here, the bubble velocities are overestimated in comparison with the measurements. As aforementioned, the authors noticed

that the bubble size distribution at the column top was broader than at the injection [54], which means that collisions, coalescence and break-up occur, phenomena that are being neglected here. This fact can be a reason for the overestimation founded in both cases, but this will not be investigated in this work. Nevertheless, the Case M2+ present slightly lower bubble rise velocities due to consideration of bubble dynamics.

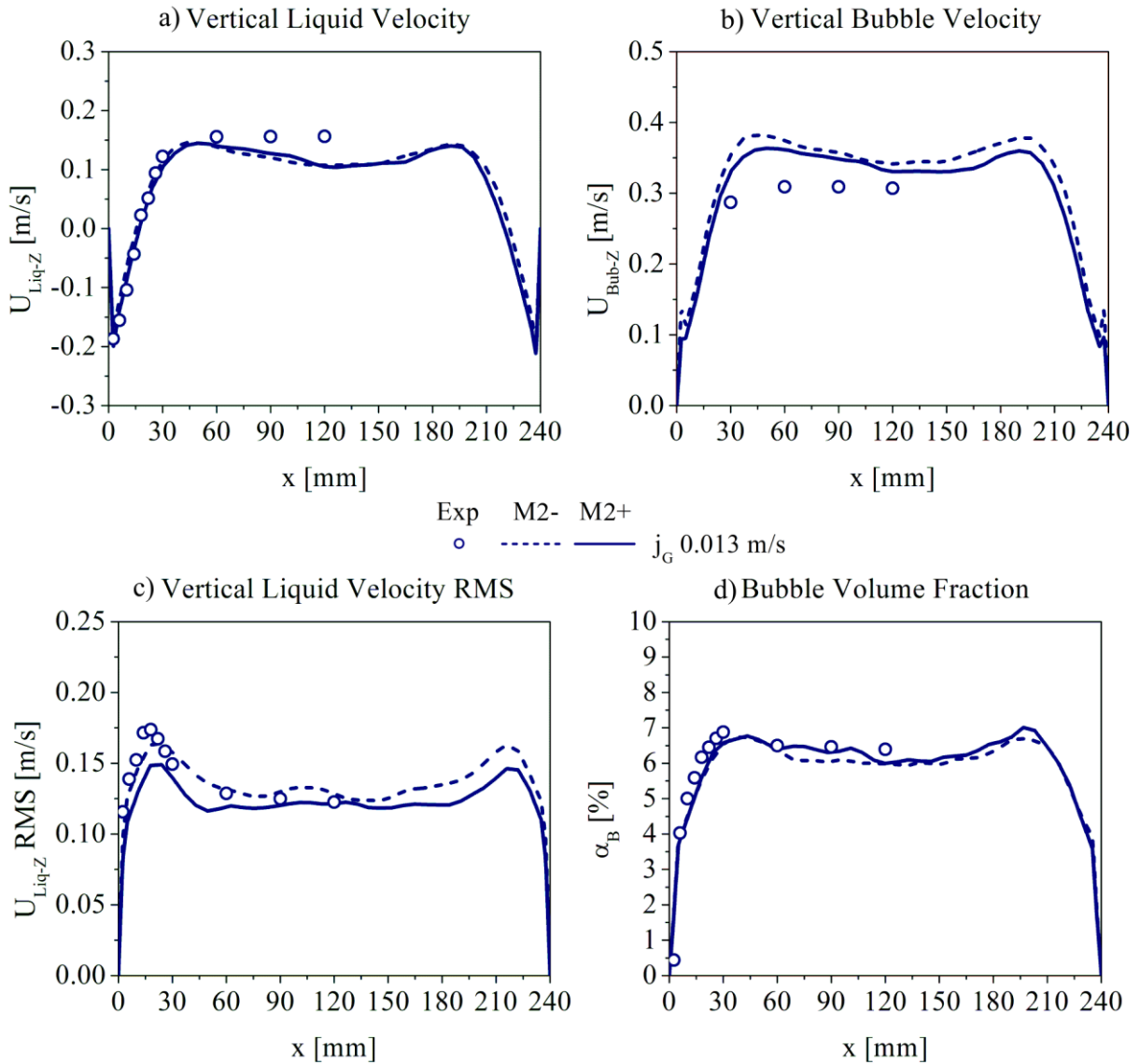


Figure 3-51: Comparison of Cases M2- and M2+ and experimental data [54]:

a) liquid vertical velocity; b) bubble vertical velocity.

c) RMS values of liquid velocity fluctuations. d) Bubble volume fraction.

$j_g = 0.013$  m/s,  $d_{B,mean} = 5.5$  mm, axial position 500 mm.

Case M2-: no oscillation, D1, L2; Case M2+: with oscillation, D2, L2.

It is apprehensible that bubble vertical velocity, residence time and volume fraction are somehow related to each other. In this framework, based on the profiles from Figure 3-51b, the underestimation of bubble volume fraction in the Figure 3-51c would be expected.

Surprisingly, the numerical and experimental results are in good agreement. The reason for that may lie on the way how the averaging is made, i.e., the mean bubble velocities are number-based and the volume fraction is time-based. For example, two bubbles with the same velocity but with different sizes, in a same time interval, would give different average volume fractions. Another example would be, a faster and greater bubble or a slower but smaller bubble could give the same volume fraction. Thus, the bubble velocity and volume fraction may not be directly related to each other.

After all, the discrepancies between the Cases M2- and M2+ are not remarkable as with the Cases M1 or the previous study case shown in the section 3.2. This can be explained by the size distribution. Once the frequency of oscillations tends to decrease with size (see Eq. (2-56)), the effect from the bubble dynamics model proposed in this work decrease as well, yet it is still present.



## 3.6 Conclusions of the chapter

In this chapter, a comprehensive study concerning the application of point-mass approximation for bubble column simulations was conducted. The model validation was made by comparing the numerical results with data found in the literature [56]. Several cases considering different models supported an extensive evaluation of the phenomena involved and their complexity.

While turbulent dispersion and bubble-induced turbulence have an impact on the fluctuations on the liquid phase, oscillations on the dispersed phase were weakly improved. Satisfactory results using the Euler/Lagrange approach were only achieved, when a bubble dynamics model was considered. Here, a stochastic estimation of bubble eccentricity and motion deviation was performed locally, yet based on experimental observations of oscillation frequencies and amplitudes. Although shape and trajectory oscillations of bubbles are not resolved within “point-mass” approximations, such dynamics imposed by the proposed model improved significantly the results with regard to bubble average velocity and fluctuations.

Moreover, a numerical evaluation of the forces competition in a bubble column was performed. The ratio of importance of each force was computed normalizing its magnitude by the correspondent buoyancy value and interesting results were obtained. As obviously expected, the drag force came out as the most important force in such flows with more than 80% of buoyancy magnitude. Successively, the added mass showed a high dependency with bubble equivalent diameter, insomuch as its values vary from 20% up to 85% of buoyancy. This may be related to the bubble oscillation attained by the model, since in the case without modelling bubble dynamics the values lie only between 10-20%. The Basset force, commonly neglected in bubble columns simulations, resulted in magnitudes from 10% to 50% of buoyancy, even higher than the transversal lift with maximum value of 9%. The fluid inertia and wall forces remained with minor significances. However, at the wall vicinity ( $x_w < 10$  mm) the wall effects raise up to 5% of buoyancy magnitude.

Furthermore, the overall contribution of the lift, Basset and wall forces in the radial direction was exposed in the very study case. It was noticed for the present bubble size spectrum, that although these forces are apparently weak in comparison to buoyancy, a long-term effect in the radial direction can yield impact on bubble dispersion. The differences in the volume fraction profile seem to grow with the ascending time. However, the averaged bubble rise velocity using two lift models remained practically unchanged.

The Basset force, which is commonly neglected in simulations, plays an important role in bubbly flows, reaching magnitudes even higher than lift force. In the case where this force was not considered, a relative error up to 3% with regard to the bubble volume fraction profile was found, though. The most impact of the history term was acting as a resistance to the motion deviation imposed by the bubble dynamics model, causing a significant reduction of RMS values from bubble fluctuating velocity. However, a higher overall lateral dispersion was promoted by the Basset force.

Due to this fact, an investigation on the Basset force was conducted in a pipe flow. In this study case [69], a constraint flow condition conceived a better interpretation of particles dispersion in terms of lateral displacement and fluctuating velocities. It was concluded that the Basset term enhanced the particles dispersion in all the present cases. Surprisingly to this, in all the three scenarios (buoyant, inert and heavier particles) a reduction of particle velocity fluctuations were found due to the history term, acting as a resistance to motion change. Once the resulting slope for longer dispersion times is similar when the Basset force is neglected, the reason for a higher lateral displacement lies in the initial conditions.

Finally, the model is applied in a study case [54] with different geometry and greater bubble size distributions than the previous simulations. The last study case of this chapter was challenging for simulations with the Euler/Lagrange method, since relative large bubbles are confined in a thin geometry. In order to achieve numerical stability using a fine mesh for the continuous phase, a smoothing function of the volume fraction field was proposed, by distributing the mapped bubble volumes to the neighbour cells. After all, the simulation where bubble dynamics is considered shows good agreement with experimental data. In the case with lower superficial gas velocity, the trajectory oscillations induced by the model yielded a core flow by avoiding the bubbles to stay at the walls. In the case with higher gas flow rate, on the other hand, both simulations revealed satisfactory results. The discrepancies by considering and neglecting bubble dynamics were here not remarkable, once oscillations frequencies for the size distribution are expected to be lower.

Summarizing, the present model was applied for two study cases, where the superficial gas velocities vary from 2.8 to 13.0 mm/s with bubble diameters from 0.5 to 9 mm. These conditions resulted in local average bubble volume fractions up to 7%. Besides, two different geometries (circular and rectangular) and systems (pure and tap water) were here evaluated. Once there is concordance between numerical and experimental data within the purposes and limitations of this work, the proposed model can be assumed so far validated from the hydrodynamic point of view. In the next chapter, an extension of this development

and implementation is proposed for the situations with mass transfer. The following cases will be evaluated with a different perspective, focused in mass fractions and bubble volumes. Nevertheless, all the hydrodynamic background needed to be first understood and validated.



# 4 On the Mass Transfer

As aforementioned, the prior commitment of modelling bubble columns is the capability to predict precisely chemical reactions and product selectivity in such apparatus. In many instances, the desired reactions and the product of interest remain in the liquid phase. However, required reagents located in the gas phase must be transported into the liquid in an efficient way, in order to promote faster reaction rates or reduce equipment dimensions.

A considerable effort has been made in order to understand mechanisms of mass and heat transfer. As a common practice, the physics is transcript into dimensionless numbers which give a way to characterize the phenomena involved. In this manner, both mass and heat transfer are practically represented by relating the convective and diffusion rates, resulting in the Sherwood and Nusselt numbers, respectively. Boussinesq [74] provided an approximation for the Nusselt number around a sphere in potential flow, dependent on Reynolds and Prandtl numbers. By analogy, this correlation is commonly applied for mass transfer on spherical clean bubbles by substituting the dependency with Prandtl by the Schmidt number, resulting in:

$$Sh_i = \frac{2}{\sqrt{\pi}} Re^{1/2} Sc_i^{1/2} \quad (4-1)$$

$$Sc_i = \frac{\mu_L}{\rho_L D_{ij}} \quad (4-2)$$

where  $D_{ij}$  is the diffusivity constant of the specie  $i$  in the specie  $j$ .

The influence of bubble oscillations on the mass transfer was theoretically determined by Montes et al. [75]. In this work it is emphasized that the mass transport rates of oscillating

bubbles can be much higher than for volume equivalent spherical bubbles. The influence of the oscillations on the mass transfer is essentially the result of a continuous change of the contact surface (bubble surface), the modification of the flow field and the concentration fields of the species near the bubbles interface. Based on a perturbation theory in conjunction with a theory for hydrodynamic oscillations, a correlation has been developed for the Sherwood number which does not include any adjustment parameters and depends on the mode and the amplitude of the oscillation. A comparison of the Sherwood number for different oscillation amplitudes shows the significant increase with increasing amplitude. Furthermore, an approximation of the Sherwood number for the amplitude and the second oscillation mode was given, which is easier to handle in a numerical calculation [75]. In later publications of this working group the approach of the Sherwood number for oscillating bubbles is combined with bubble coalescence and break-up to calculate the mass transfer coefficient values for bubble columns [76].

Due to its high solubility in water and several interests, the carbon dioxide is very attractive and popular among experimental works regarding mass transfer. High speed imaging techniques have been applied on single CO<sub>2</sub> bubbles by many research groups, in order to evaluate mass transfer coefficients with precision. Merker et al. [48], for example, measured the decay of volume from CO<sub>2</sub> and NO bubbles between 1.5 and 3.0 mm in degassed water, showing also the transition from ellipsoidal and oscillating bubbles to a sphere. Dissolution of Taylor-bubbles in water and glycerol solutions was also evaluated by Hosoda et al. [77,78]. Moreover, the presence of surfactants or contamination at the bubble surface can have also effects on the mass transfer and, thus, this is also a point of interest in the engineering [79,80]. Beside the individual assessment of mass transfer from single carbon dioxide bubbles, many works are also related with bubble swarms and chemical reactions in the liquid phase, such as the chemisorption of CO<sub>2</sub> in NaOH solutions [81,82,83,84].

The chemisorption of CO<sub>2</sub> has been used until nowadays as study case for development and validation of CFD models with mass transfer in bubble swarms. This is a complex case for simulations, once the prediction of bubble and liquid flows, mass transfer and chemical reactions are directly coupled with each other, not to mention the thermal sensibility of physics properties. Nevertheless, a great development has been already done not only in the frame of Euler/Euler [85,86] approach, but also in Euler/Lagrange [5,13,84]. However, in all the numerical calculations performed so far, withal the detailed and rigorous modelling with respect to thermodynamics and reaction kinetics, one important aspect has been neglected, namely the dynamics of the bubbles.

In the present work, a CFD model based on the Euler/Lagrange point-particle approach is proposed, considering not only bubble dynamics through stochastic generation of eccentricity and tumbling motion, as seen in the Chapter 2, but also its effect on mass transfer, making use of a dynamic Sherwood number [75], accounting for the oscillation amplitude.

## 4.1 Modelling the mass transfer

As aforementioned, the following description of the numerical approach is an extension of the modelling presented in the section 2, with purpose for simulating cases with mass transfer. For the sake of brevity, equations which were not modified will not be here repeated.

### 4.1.1 Continuous phase

Consistent to the approach for hydrodynamic situations, Large Eddy Simulations (LES) were used for solving the flow field and modelling the turbulence of the continuous phase. In all the cases from this chapter, the Volume of Fluid (VoF) method is not significant. Hence, such extra modelling can be spared. Moreover, in order to solve mass transfer between the phases, an additional equation for each participant species is required. In this framework, the governing equations are showed in the Table 4-1, as follows:

Table 4-1: Continuous phase governing equations.

Continuity	$\frac{\partial(\alpha_c \rho_L)}{\partial t} + \nabla \cdot (\alpha_c \rho_L \mathbf{u}_L) = 0$	(4-3)
Momentum	$\frac{\partial(\alpha_c \rho_L \mathbf{u}_L)}{\partial t} + \nabla \cdot (\alpha_c \rho_L \mathbf{u}_L \mathbf{u}_L) = -\nabla p - \nabla \cdot (\alpha_c \rho_L \boldsymbol{\tau}_L) + \alpha_c \rho_L \mathbf{g} + \overline{\mathbf{S}_{u,p}}$	(4-4)
Species	$\frac{\partial(\alpha_c \rho_L Y_{i,L})}{\partial t} + \nabla \cdot (\alpha_c \rho_L u_L Y_{i,L}) = \nabla \cdot [\alpha_c D_{i,eff} \nabla (\rho_L Y_{i,L})] + S'_{Y,i,p}$	(4-5)

in which,  $\alpha_c = 1 - \alpha_B$  is the volume fraction of the carrier phase due to the presence of bubbles,  $\rho_L$  is local density of the liquid phase,  $Y_{i,L}$  is the mass fraction of the specie  $i$  in the continuous phase. The cell-based species source-terms  $S'_{Y,i,p}$ , regarding to the mass transfer

between the phases, is expressed by the Equation (4-6), by summing over all traversing parcels  $k$  and the number of Lagrangian time steps  $n$  as follows:

$$S'_{Y,i,p} = -\frac{1}{V_{cv}\Delta t_E} \sum_k \sum_n [(m_k^{n+1} - m_k^n)N_k] \quad (4-6)$$

With regard to the species equation, an additional term for the effective diffusion coefficient is also taken into account based on the SGS turbulence, as follows:

$$D_{i,eff} = D_{i,L} + D_{t,i,L} \quad (4-7)$$

$$D_{t,i,L} = \frac{\mu_{eff}}{\rho_L S_{c_{SGS}}} \quad (4-8)$$

where  $S_{c_{SGS}}$  is the Schmidt number of the fine structure in turbulence, considered to be constant and equal to 0.7 in all the cases. In the cases present in this work, the SGS term is much greater than the molecular diffusion coefficient ( $D_{t,i,L} \gg D_{i,L}$ ), so that  $D_{i,L}$  could be negligible.

#### 4.1.2 Discrete phase

The bubble tracking is performed here identically as described by the equations (2-13) and (2-14) in the previous chapter. Since mass transfer occurs between the phases, the diameter of each bubble must be updated at every Lagrangian time-step.

In CFD simulations, the initial diameter and density of parcels are usually defined by the user as input data. If mass transfer occurs during the tracking, two approaches are normally found: either the density is assumed constant and the diameter is updated, or the diameter remains constant and the density is changed. Nevertheless, only these two same options are available in the platform OpenFOAM 4.1. For the case of rising bubbles, none of these assumptions is a good choice, inasmuch as both density and diameter are actually changing. One reason for that is the direct loss/gain of mass, and consequently volume, due to transfer between phases. If the composition of gases inside the bubbles is different, the density must be updated, either. Another reason is the hydrostatic head, inasmuch as the bubble will perceive a different pressure at each position along the column height, resulting in a different density. The solution for that was to implement an equation of state for the discrete phase, namely to assume ideal gas.



In this framework, the bubble density and diameter are updated at every Lagrangian time-step according the local thermodynamic circumstances and the instantaneous composition, as follows:

$$t_B = 0 \quad \left\{ \begin{array}{l} V_{B0} = \frac{\pi}{6} d_{B0}^3 \\ m_{B0} = V_{B0} \rho_{B0} = V_{B0} \frac{p_0}{RT} \sum_i Y_{B,i,0} W_i \end{array} \right. \quad (4-9)$$

$$t_B > 0 \quad \left\{ \begin{array}{l} V_B = \frac{m_B}{\rho_B} = m_B \frac{RT}{p} \frac{1}{\sum_i Y_{B,i} W_i} \\ d_B = \sqrt[3]{\frac{6}{\pi} V_B} \end{array} \right. \quad (4-10)$$

where  $t_B$  is the bubble age in the domain,  $R$  is the universal constant of gases,  $T$  is the temperature,  $Y_{B,i}$  is the mass fraction of the specie  $i$  inside the bubble and  $W_i$  is the molecular weight of the specie  $i$ .

Note that in the bubble injection  $d_{B0}$  and  $Y_{B,i,0}$  are still defined by the user and the correspondent  $V_{B0}$  and  $m_{B0}$  are calculated in function of them. During the Lagrangian tracking, on the other hand,  $m_B$  and  $Y_{B,i}$  are first updated by the mass transfer model, and then  $V_B$  and  $d_B$  are calculated according the new composition. In this manner, the mass flow rate of the gas phase entering in the system is totally dependent of the proper estimation of  $p_0$  and  $T$ , even if the volumetric flow rate is identical to the measurements.

#### 4.1.3 Mass transfer model

In order to simplify the modelling of mass transfer from bubble to the liquid, it is common and reasonable to consider that resistance for this transport remains only on the liquid side [12,15,40,59,60]. Hence, the mass transfer rate  $\dot{m}_i$  dependent on the coefficient  $k_c$  and the ellipsoidal bubble interfacial area  $A_e$  can be defined as follows:

$$\dot{m}_i = \frac{dm_i}{dt} = \rho_L k_L A_e (Y_{S,i,k} - Y_{\infty,i,k}) \quad (4-11)$$

$$k_L = \frac{Sh_i D_{ij}}{d_B} \quad (4-12)$$

$$A_e = 2\pi \left[ a^2 + c^2 \frac{a \tanh(e)}{e} \right] \quad (4-13)$$

$$e = \sqrt{1 - \chi^{-2}} \quad a = \frac{d_B}{2} \sqrt[3]{\chi} \quad c = \frac{a}{\chi}$$

where  $Sh_i$  is the Sherwood number.  $Y_{\infty,i,k}$  represents the bulk mass fraction of specie  $i$  and  $Y_{s,i,k}$  at the bubble surface, both in the liquid side. In some situations, the chemical reactions can have an influence in the mass transfer. Such influence is normally modelled through addition of a so-called enhancement factor  $E$ , in which a proper correlation is required for each case. Concerning to the chemical absorption of carbon dioxide in basic (alkaline) solutions, for example, the enhancement factor is highly increased for large pH values. However, in this study case the pH-value is neutral and there is no influence from the chemical reaction on the mass transfer. Hence, the enhancement  $E$  was set constant and equal to the unity.

Since the active species are dilute in the continuous liquid phase, a relation between the mass fractions at both sides of bubble interface can be assumed, making use of Henry's constant  $H_{i,k}$ :

$$Y_{s,i,k} = H_{i,k} Y_{B,i} \frac{\rho_B}{\rho_c} \quad (4-14)$$

Analogically to the liquid velocity seen by the bubble, it can be also assumed that  $Y_{\infty,i,k}$  consists in two contributions, the mean mass fraction of the active specie interpolated to the bubble position  $\overline{Y_{\infty,i,k}}$  and a SGS variation (standard deviation)  $\dot{Y}_{\infty,i,k}$ , as follows:

$$Y_{\infty,i,k} = \overline{Y_{\infty,i,k}} + \dot{Y}_{\infty,i,k} \quad (4-15)$$

$$\dot{Y}_{\infty,i,k}^{n+1} = \dot{Y}_{\infty,i,k}^n R_L + \sigma_{Y,i} \xi_i \sqrt{1 - R_L^2} \quad (4-16)$$

$$\sigma_{Y,i} = \sqrt{\frac{1}{nb} \sum_{nb} \left( \frac{\overline{Y_{\infty,i,k, nb}} - \overline{Y_{\infty,i,k}}}{2} \right)^2} \quad (4-17)$$

where  $\sigma_{Y,i}$  is the local RMS cell value for the mass fraction of specie  $i$  in comparison with the neighbouring cells  $nb$  (level 1), interpolated to the bubble position.

Sherwood number correlations for bubbles are commonly found in the literature with dependency on Reynolds and Schmidt dimensionless numbers. In order to take into account relevant effects of bubble shape oscillations on the mass transfer, Montes et al. [75] proposed a correlation based on analytical shape oscillations from Tsamopoulos and Brown [87], including the oscillation amplitude  $A$  and the Weber number  $We$ . The authors elaborated the model integrating and averaging a local Sherwood number at the bubble surface during a whole oscillation period, yielding the following equation:

$$Sh_i = \frac{2}{\sqrt{\pi}} Pe_i^{1/2} \left[ I_{n1} + I_{n2} \frac{A}{\omega_n^2} We^{1/2} \right] \quad (4-18)$$

$$Pe_i = Re_B Sc_i \quad Sc_i = \frac{\mu_c}{\rho_c D_i} \quad We = \frac{\rho_c |u_B - u_c|^2 d_B}{\sigma} \quad (4-19)$$

$$A = \frac{1}{2} \left( \frac{\chi - 1}{\chi^{2/3}} \right) \quad (4-20)$$

where  $I_{n1}$  and  $I_{n2}$  are integrals constants dependent on the amplitude [31].  $Pe$ ,  $Sc$  and  $\omega_n$  are Peclet number, Schmidt number and oscillation frequency of the bubble, respectively. These integrals can be solved *a priori* for the range of amplitudes in use ( $0 \leq A < 1$ ) and fitted in a polynomial function of third order, as seen in the Figure 4-1. The resulting parameters are shown in the Table 4-2 for the second mode of oscillation, with  $\mathcal{R}^2 > 0.999$  and the form  $I_n(A) = p_0 + p_1 A + p_2 A^2 + p_3 A^3$ .

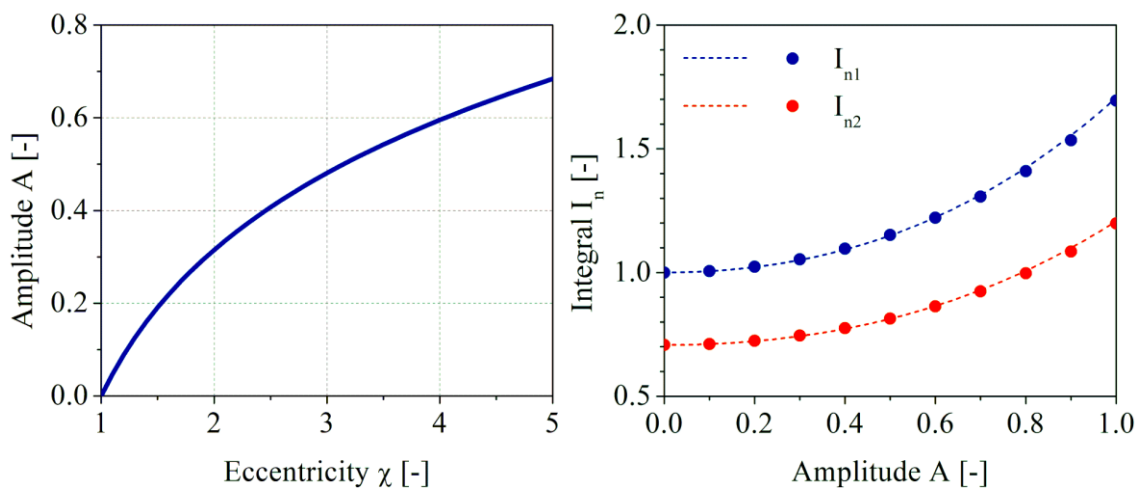


Figure 4-1: a) Amplitude dependency with bubble eccentricity; b) Solved integrals and fitting.

Table 4-2: Fitting parameters for the integral constants  $I_{n1}$  and  $I_{n2}$ .

	$I_{n1}$	$I_{n2}$
$p_0$	1	0.7053824476
$p_1$	0.0518939191	0.0487541958
$p_2$	0.3438189502	0.2202937063
$p_3$	0.2944385138	0.2208741259

Note that when the amplitude reaches a null value ( $A \rightarrow 0$ ), the terms inside the brackets in the Equation (4-18) become the unity. At this point the correlation recovers the form introduced by Boussinesq [74] for oscillating sphere.

Among the two correlations for the Sherwood number showed here, other correlations are found in the literature [88,89], some also in function of bubble eccentricity, e.g., Lochiel and Calderbank [90]. Nevertheless, in this work only the correlations of Montes et al. [75] and Boussinesq [74] will be evaluated. Although a fitting function was proposed here for sparing of computational resources, the preference for Montes et al. [75] correlation is for being based on first principles and accounting for bubble oscillations.

#### 4.1.4 Thermodynamic properties

The solubility of the species in the liquid phase plays also an important role in the prediction of mass transfer, as well as the diffusivity. The proper estimation of these thermodynamics properties will determine the equilibrium between the phases and how fast the equilibrium is reached, according to each of the participant species. Both the Henry's constant and the diffusivity of gases in water are highly dependent on the temperature, inasmuch as a difference of only 5°C can impact significantly on the results.

In this framework, the dimensionless Henry's constant was calculated with the general equation (4-21), in which the required parameters are available in the literature [91], as described in the Table 4-3, as follows:

$$H_{i-H_2O} = RTk^o_H \exp \left[ \theta_T \left( \frac{1}{T} - \frac{1}{298.15} \right) \right] \quad (4-21)$$

Table 4-3: Parameters for the Henry's constants. Source: Sander [91].

	$k^o_H$ [mol m <sup>-3</sup> Pa <sup>-1</sup> ]	$\theta_T$ [K]
CO <sub>2</sub>	$3.3 \times 10^{-4}$	2400
O <sub>2</sub>	$1.2 \times 10^{-5}$	1700
N <sub>2</sub>	$6.4 \times 10^{-6}$	1600
Ar	$1.4 \times 10^{-5}$	1700

where the pre-exponential factor  $k^o_H$  is the dimensional Henry's constant at  $T = 25^\circ\text{C}$  and  $\theta_T$  is the temperature dependence constant. Note that the solubility of these gases increases when the temperature decreases.

The diffusion coefficients for gases in water ( $T = 25^\circ\text{C}$ ) are available in the literature [92], as described in the Table 4-4, as follows:

Table 4-4: Diffusion coefficients for gases in water. Source: Cussler [92].

	$D_{i-H_2O}$ [m <sup>2</sup> s <sup>-1</sup> ]
CO <sub>2</sub>	$1.92 \times 10^{-9}$
O <sub>2</sub>	$2.1 \times 10^{-9}$
N <sub>2</sub>	$1.88 \times 10^{-9}$
Ar	$2.0 \times 10^{-9}$

Once the diffusivity is known for a certain temperature, it can be approximated for other temperatures using the Stokes-Einstein equation from the kinetic theory, as follows:

$$D_{ij,T1} = D_{ij,T2} \frac{T_1 \mu_{T2}}{T_2 \mu_{T1}} \quad (4-22)$$

For the case of carbon dioxide, a more precise correlation than the Eq. (4-22) is proposed by Versteeg and van Swaaij [93]:

$$D_{CO_2-H_2O} = 2.35 \times 10^{-6} \exp\left(-\frac{2119}{T}\right) \quad (4-23)$$

Note that the diffusion coefficient increases with the temperature, differently than the solubility.

Once the modelling for the mass transfer is finally closed, study cases for the model validation will be presented in the next sections.



# 5 Results – Mass Transfer

This following section is focused on the results considering mass transfer. The model validation was conducted in a similar manner as before, in which two study cases were evaluated. The first one consists of single bubbles rising in a quiescent liquid and the other one of bubble swarm with co-current flow.

## 5.1 Single Bubbles

Analogue to the cases without mass transfer in the chapter 3, the model was first tested for isolated bubbles. In order to do so, the experimental data from Merker et al. [48] was used for comparison and model validation.

### 5.1.1 Case descriptions and setup

The experiments conducted by Merker et al. [48] considered single CO<sub>2</sub> bubbles rising in a column filled with water. With the purpose to improve the evaluation of mass transfer in the experiments, the distilled water suffered a degassing process by boiling it for 60 minutes before the experiments. Afterwards, the water was rapidly cooled and stored under an atmosphere of argon. The column was described as circular, with a diameter of 75 mm and a height of 2 m. Three rising bubbles with different initial sizes ( $V_{B0} \cong [4, 9.6, 12.4] \text{ mm}^3$ ,  $d_{B0} \rightarrow 2\sim 3\text{mm}$ ) were evaluated in time in respect of their volume during 3 s, making use of a high speed camera which follows the bubble with a traverse system. In order to simulate this case, a numerical structured O-grid with 51,939 volumes in total (261 per cross-section and 199 in the height) was used. The resulting ratio between the bubble size  $d_{B0}$  and the mean grid length  $\Delta x$  was  $d_{B0}/\Delta x \approx 0.538$ . Since only single bubble simulations are performed, the

mesh has no significant influence on the results. All boundaries were set as non-slip wall condition for the liquid and as rebound for the bubbles. The used Henry's dimensionless constant for  $T = 25^\circ\text{C}$  was  $H_{\text{CO}_2\text{-H}_2\text{O}} \cong 0.818$  [70], the diffusivity coefficient was set to  $D_{\text{CO}_2\text{-H}_2\text{O}} = 1.92 \times 10^{-9} \text{ m}^2/\text{s}$  and the Eulerian time-step was set 5 ms.

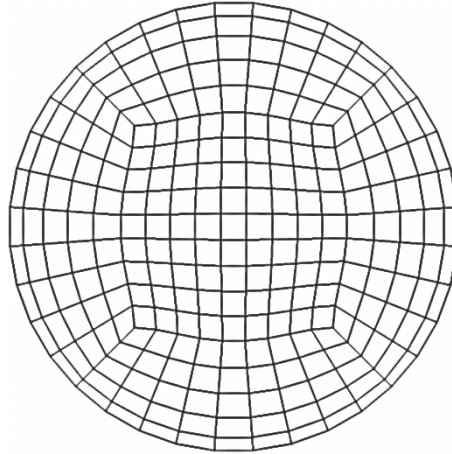


Figure 5-1: Numerical grid used in the single bubble simulations.  
51,939 volumes in total, 261 per cross-section and 199 in the height.

With the purpose of verification and better understanding during the implementation process in this work, different modelling complexities were considered in the simulations for this case. Although single bubble experiments can sound simple, many details should be precisely respected when mass transfer phenomena are present, as will be described in the following. In this framework, a summary from the simulations setup is shown in the Table 5-1.



Table 5-1: Cases description for different simulations.

	Bubble composition			Liquid composition			OM	Mass transfer	General description
	$Y_{B,CO_2}$	$Y_{B,N_2}$	$Y_{B,Ar}$	$Y_{L,CO_2}$	$Y_{L,N_2}$	$Y_{L,Ar}$			
Case 0	1.0	0.0	0.0	0.0	0.0	0.0	x	B→L	Pure CO <sub>2</sub> , bubble osc.
Case 1	0.95	0.05	0.0	0.0	0.0	0.0	x	B→L	Commercial CO <sub>2</sub> , bubble osc.
Case 2	0.95	0.05	0.0	0.0	0.0	$Y_{L,Ar}^{sat}$		B↔L	Commercial CO <sub>2</sub> , no osc., back diffusion
Case 3	0.95	0.05	0.0	0.0	0.0	$Y_{L,Ar}^{sat}$	x	B↔L	Commercial CO <sub>2</sub> , bub. osc., back diff.

### 5.1.2 Results and discussion

The simulations using the present model were conducted for the three bubble initial sizes described in the reference [48], considering at first hypothetically pure CO<sub>2</sub> bubbles (Case 0). The transient bubble volumes are compared with the experimental data in the Figure 5-2. According to the experiments, after the 3s, bubbles were still present in the system, surprisingly. In the calculations for Case 0, on the other hand, all the three bubbles disappear before 2.5 seconds. This situation is explained by a possible presence of an unknown second component in the system. To consider pure CO<sub>2</sub> bubbles in such case, i.e., to neglect the possibility of a back-diffusion of another species from the liquid to the bubble, or even that the purity of the CO<sub>2</sub> used is not 100%, results in a total dissolution of these bubbles. In this manner, the Case 1 assumes commercial CO<sub>2</sub> bubbles, where 95% purity is guaranteed, and the other 5% consists in other gases, mostly N<sub>2</sub>. Note in the Figure 5-2 that after 3 seconds the bubbles from Case 1 are still present in the domain. However, the volumes are still underestimated. The interesting part is that an impurity of only 5% of nitrogen can influence significantly the mass transfer. This happens due to the jump condition at the bubble interface (Eq. (4-14)), in which the mass fraction of CO<sub>2</sub> is not anymore constant and equal to the unity. Since the mass transfer rate is different for each component, in this case faster for the CO<sub>2</sub>, its mass fraction inside the bubble will decrease over time and consequently, the driving gradient at the liquid side. After all, the remainder volume at 3 seconds consists practically from nitrogen, in which the resulting mass fractions of N<sub>2</sub> were 90%, 95% and 97%, from the

smallest to the biggest bubble, respectively. Since the Case 1 assumes no presence of these species in the liquid, it is expected that in a longer and enough time these bubbles would completely dissolve as well.

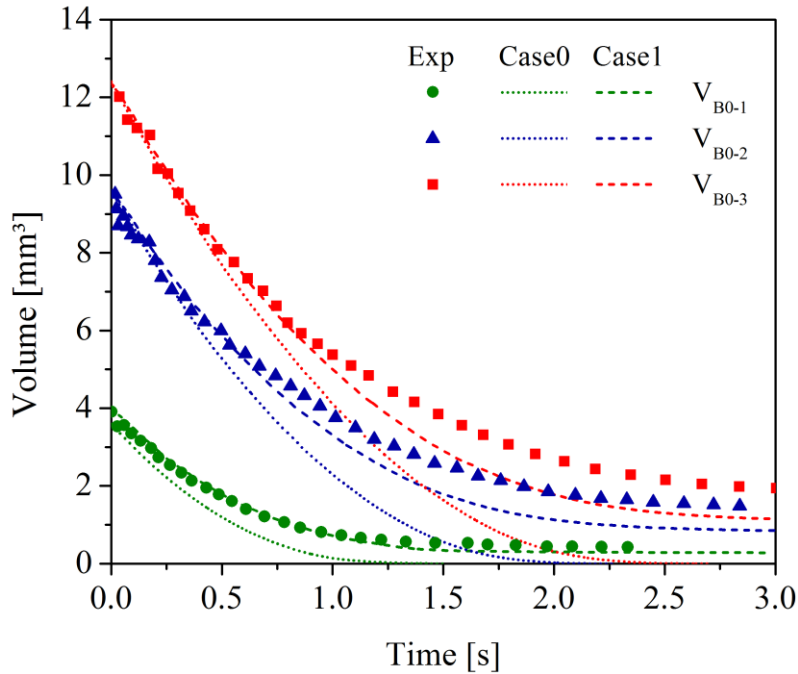


Figure 5-2: Decay of bubble volume in time. Experiments by: Merker et al. [48].  
Case0: Pure CO<sub>2</sub>, bubble oscillations; Case1: CO<sub>2</sub> + N<sub>2</sub>, bubble oscillations.

Boiling the water for 60 min and store it under argon atmosphere can provide enough degassing from non-desired species dissolved in the liquid. However, the diffusion of argon into the water cannot be avoided. In this framework, the subsequent simulations (Case 2 and 3) were performed considering an initial concentration of argon in the water. Once this information is not available, the saturation was assumed.

The Case 2 neglects bubble dynamics, i.e., the bubbles are assumed to be spherical and no trajectory oscillation is imposed by the model. The Case 3, on the other hand, considers the complete model, i.e., effects of bubble dynamics are taken into account not only on their motion, but also on shape and mass transfer, in which the bubble eccentricity increases contact area and the dynamic Sherwood number is based on the oscillation amplitude. The resulting decay of volume from these cases is compared with the experimental data in the Figure 5-3, as follows:

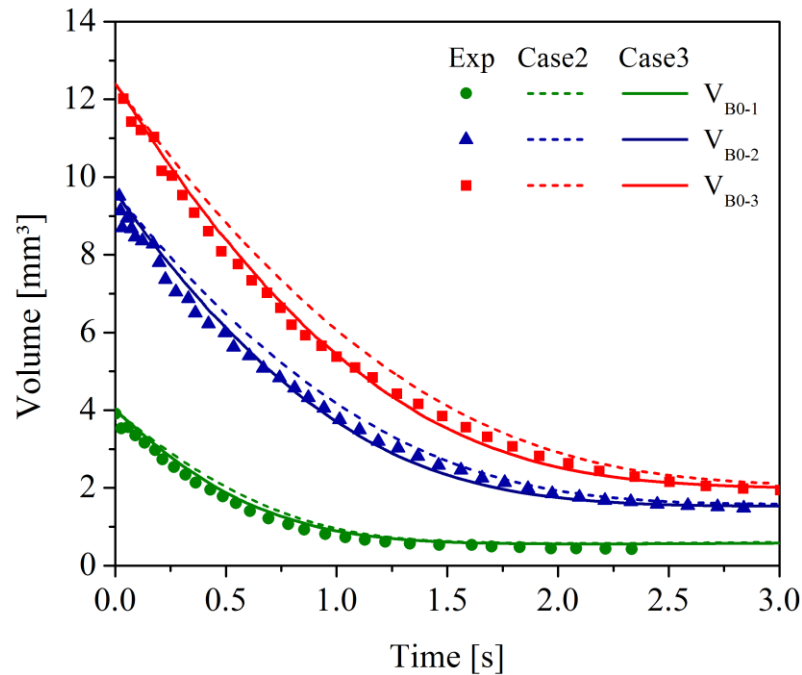


Figure 5-3: Decay of bubble volume in time.  $\text{CO}_2 + \text{N}_2$ , back-diffusion (Ar). Case2: no oscillation; Case3: with oscillations. Experiments by: Merker et al. [48].

Note that the final bubble volume achieved in both cases is in concordance with the experimental data. Nevertheless, the difference between the cases lies during the process. When bubble dynamics is neglected (Case 2), the mass transfer rate may be underestimated, mainly for larger bubbles, where shape and motion oscillations are more accentuated. This discrepancy is corrected when the bubbles are assumed ellipsoids and the dynamic Sherwood number is considered (Case 3). The difference between these cases can be apparently insignificant in the situation of a single bubble. However, thinking in a bubble swarm, the effect on the mass transferred to the fluid or vice-versa would be proportional to the number of bubbles injected, whatever how minimal it is.

After all, the consideration of additional species improved significantly the results with respect to final bubble volume. This behaviour can be better understood comparing the mass fraction of  $\text{CO}_2$  at the bubble surface, estimated by the Henry's law, as seen in the Figure 5-4. As aforementioned, when a pure  $\text{CO}_2$  bubble is considered (Case 0), the mass fraction inside the bubble is constant and equal to the unity. In this manner, a nearly constant mass concentration at the surface comes out, with a light slope resulting from hydrostatic pressure effects on the bubble density during its ascendance in the column. Here, the driving gradient is totally overestimated, resulting in high mass transfer rates. On the other hand, the presence of other species on the bubbles from Case 3 produces a transient decay of  $\text{CO}_2$  mass fraction according to their instantaneous composition. Since a “point-mass” approximation is

being used, such level of modelling can be handled practically without additional computational costs. Thus, this information is calculated and stored individually for each bubble and updated in each Lagrangian time-step.

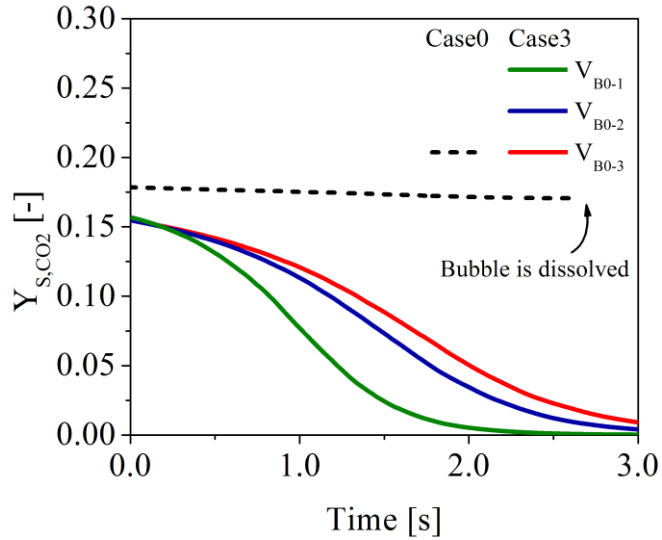


Figure 5-4: CO<sub>2</sub> mass fraction at bubble surface on the liquid side comparing Case0 with Case3 for the three initial bubble volumes  $V_{B0}$ .

The bubbles from these cases present oscillations in the shape and motion, which were considered using the bubble dynamics model proposed [33]. Such behaviour produced direct effects on mass transfer, where the ellipsoidal bubble surface area is greater than a volume equivalent sphere, beside the increase of Sherwood number described by Montes et al. [31]. The stochastic variation of bubble surface area in time due to its eccentricity is shown in the Figure 5-5.

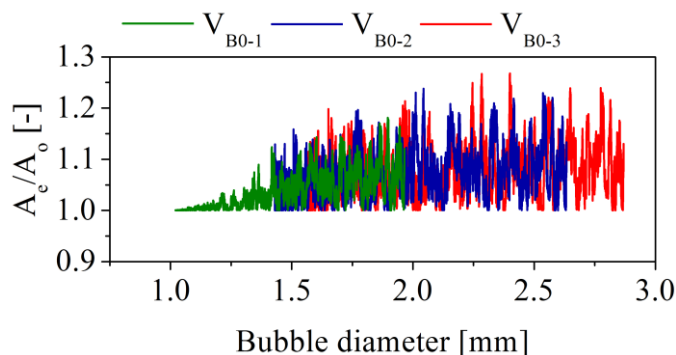


Figure 5-5: Evolution of surface area ratio (i.e. surface area of ellipsoidal bubble over that of a volume equivalent sphere) plotted versus the bubble volume equivalent diameter considering Case3 for the three different initial bubble volumes  $V_{B0}$ .

Note that in these cases the ellipsoidal bubbles present an increase of superficial area up to 20% for sizes over 1.5 mm. From this size down to 1 mm the bubble oscillation become

weaker and eventually bubbles remain spherical. Below 1 mm the bubble is spherical and the eccentricity RMS value becomes null (Eqs. (2-66) and (2-67)).

The tumbling motion of bubbles produced by the oscillation model is also reflected on the Reynolds and, consequently, the Sherwood numbers. The instantaneous bubble Reynolds number calculated with the volume equivalent sphere diameter in dependence of the bubble diameter is shown in the Figure 5-6.

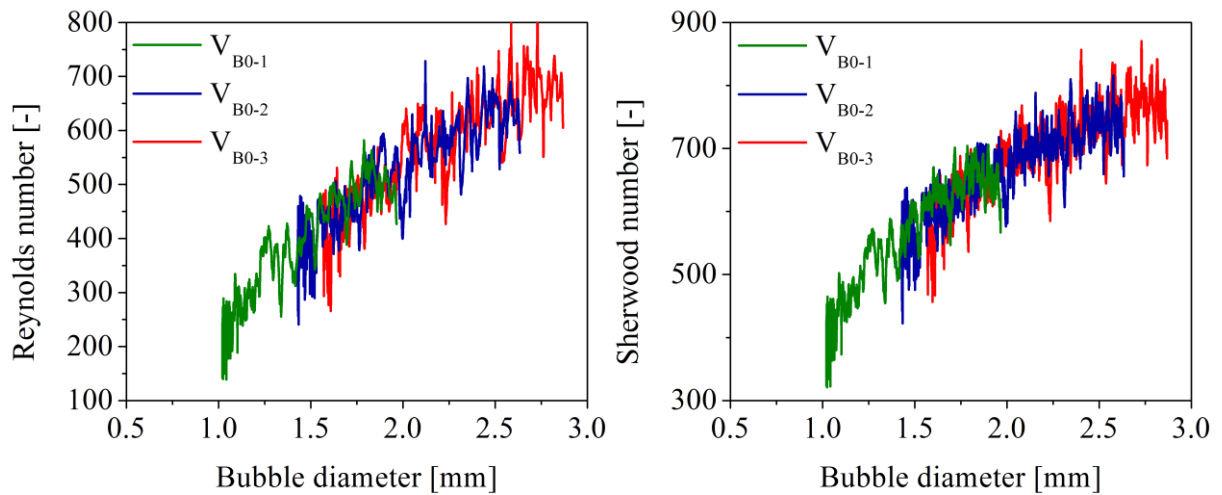


Figure 5-6: Evolution of Reynolds and Sherwood number in function of bubble diameter considering Case3 for the three different initial bubble volumes  $V_{B0}$ .

A comparison of the dynamic Sherwood number obtained numerically with the Boussinesq [74] correlation is shown in the Figure 5-7.

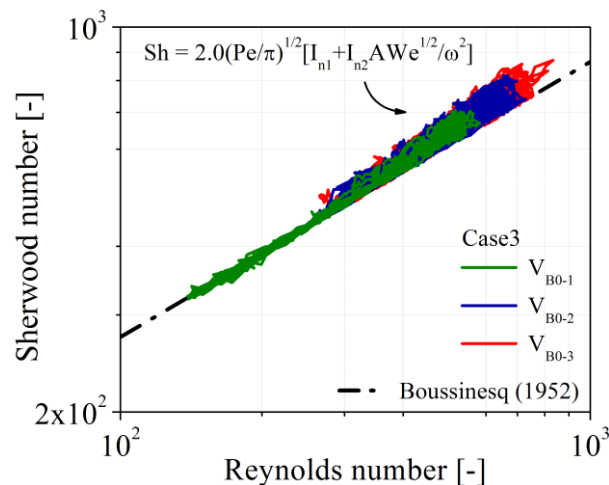


Figure 5-7: Comparison of Sherwood number with experimental observations considering Case3 for the three different initial bubble volumes  $V_{B0}$ .

Here, the numerical results are represented with solid lines show the effect of oscillation amplitude, in which an increase on the Sherwood number afforded by the terms

inside the brackets (i.e. resulting from bubble dynamics) is noticed. The dashed line is the Boussinesq correlation for spherical particles in an oscillating flow. Note that the smallest bubble in evaluation (B-1) reaches a size with lower oscillations, in which the two correlations become equivalent ( $A \rightarrow 0$ ).

Once the model is here assumed validated for mass transfer of single bubbles, the next step is to extend its application for bubble swarms, as presented in the next section.

## 5.2 Bubble Swarms

In this last section the present model will be applied on a scenario, where the mass transfer is evaluated for bubble swarms. The purpose of validation here is to use interesting experimental data, which can verify the model capability and potentiality, as a step closer to further development in the direction of chemical reactions. In this framework, the experimental data from Deckwer et al. [94] showed to be suitable for this objective.

### 5.2.1 Case description and setup

The experiments conducted by Deckwer et al. [94] consist in two bubble columns where co-current and counter-current liquid flows were evaluated in different operational conditions. One case from the several runs performed by the authors was here arbitrary chosen. The column of this case is 4.4 m height with 150 mm of diameter and is operated with tap water as co-current flow with the bubbles. A mixture of carbon dioxide and air is injected through a glass sintered plate at the column bottom in a superficial velocity  $j_G = 0.0275$  m/s. The water inlet occurs around the gas sparger in a superficial velocity  $j_L = 0.0472$  m/s. The numerical grid used in the simulations has 47,740 elements in total, in which 217 elements form a cross-section, as seen in the Figure 5-8. The bottom boundary is divided in two regions correspondent to the bubbles and liquid inlets. The determination of bubble inlet position is made randomly over the whole inner region shown in the Figure 5-8.

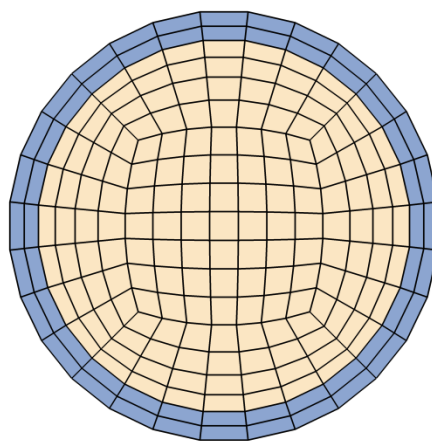


Figure 5-8: Numerical grid used in the bubble swarm simulations. 47,740 volumes in total, 217 per cross-section and 220 in the height. Outer region: liquid inlet; inner region: gas inlet.

The experiment was performed in a temperature of 14 °C, i.e., the solubility of the evaluated gases in the water are higher than from the previous study case, while the

diffusivity is lower. According to the authors, the molar fraction of CO<sub>2</sub> was measured in several positions along the column, in which gas samples were taken from side flanges and quantified with gas chromatography. Moreover, since the bubble column is relatively tall, not only absorption of CO<sub>2</sub> in the liquid is expected, but due to hydrostatic head effects desorption of the same specie was observed experimentally. The evaluation of gas hold-up was performed making use of many pressure sensors in different heights.

The bubble average size is given at the height of 2 m and is equal to  $\bar{d}_b \cong 1.85$  mm, however, due to lack of data a normal distribution was assumed at the column bottom with a mean diameter  $\bar{d}_b = 2.9$  mm and standard deviation of  $\sigma_d = 0.2$  mm. With respect to the gas superficial velocity, the resulting number of bubbles injected per second is  $f_B \cong 38,055$  s<sup>-1</sup>. In order to spare computational time without losing significant resolution of the bubble phase, the number of real bubbles per parcel in this case was set to  $N = 5$ .

Since the liquid used in the experiments was tap water, model adaptations for a contaminated system are needed, as described before in the section 3.5.1. In the case of mass transfer, additional modifications are required. In this manner, the dependency of the Sherwood number on Schmidt number turns from the power of 1/2 to 1/3 [95], as follows:

$$Sh_i = 0.6Re_B^{1/2}Sc_i^{1/3} \quad (5-1)$$

The account for bubble oscillation can be made analogue to clean bubbles, similarly as performed by Aoki et al. [79], transforming the Eq. (5-2) into:

$$Sh_i = 0.6Re_B^{1/2}Sc_i^{1/3} \left[ I_{n1} + I_{n2} \frac{A}{\omega_n^2} We^{1/2} \right] \quad (5-2)$$

Finally, the description of different simulations conducted in this work is shown in the Table 5-2. The Case D0 considers hypothetically a clean system and bubble dynamics. The Cases D- and D+, on the other hand, consider a contaminated system, but compare the models with and without bubble dynamics.



Table 5-2: Cases description for different simulations.

	Bubble composition		Liquid composition		OM	General description
	$Y_{B,CO_2}$	$Y_{B,Air}$	$Y_{L,CO_2}$	$Y_{L,Air}$		
Case D0	0.8886	0.1114	3.286e-7	2.36e-5	x	Clean, with osc.
Case D-	0.8886	0.1114	3.286e-7	2.36e-5		Contaminated, no osc.
Case D+	0.8886	0.1114	3.286e-7	2.36e-5	x	Contaminated, with osc.

### 5.2.2 Results and discussion

Inasmuch as the bubble column operates in concurrent flow, a pseudo-steady state is achieved. Using the operational conditions of the liquid phase described in the Table 5-2 also as initial conditions, the pseudo-steady state was reached around 120~160 s of simulation. After this point, the mean concentrations of the species in both liquid and gas phases are nearly constant as well the total gas hold-up. This same behaviour was observed in all the cases with some deviations from each other. Statistics were sampled for 50 seconds for a satisfactory averaging.

With the objective of comparison with experimental data, the average molar fraction of  $CO_2$  from the dispersed phase over the column height was calculated for many cross-sections and shown in the Figure 5-9.

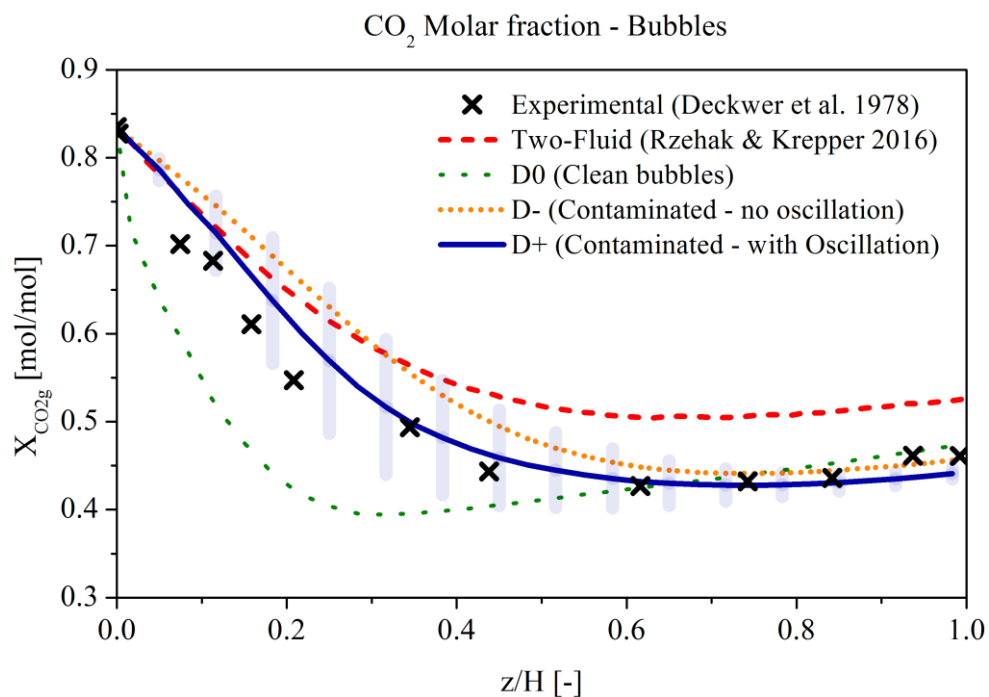


Figure 5-9: Resulting molar fraction of  $CO_2$  over the column height. Experiments: Deckwer et al. [94]; Two-fluid simulations: Rzehak and Krepper [96].

Note in the Figure 5-9 that the gas phase reaches the equilibrium with the liquid phase around the half of the column height, came after a steep decay of CO<sub>2</sub> molar fraction at the column bottom. In this region, a great driving concentration gradient is combined with large contact area between the phases, resulting in high mass transfer rates. When bubble dynamics are considered, this behaviour is well captured in the simulations. Moreover, since the column is tall enough, effects of the hydrostatic head becomes notable, i.e., during their ascendance the bubbles expand slowly by perceiving lower pressure from the liquid, which decreases their density. Consequently, the concentration of CO<sub>2</sub> at the bubble surface (liquid side) will become lower than in the bulk of the liquid ( $Y_{B,CO_2}^* < Y_{\infty,CO_2}$ ), shifting the equilibrium. At this point, the dissolved carbon dioxide in the liquid is transferred back to the bubbles, which causes the light increase of molar fraction seen in the Figure 5-9.

Note in the Case D0, where the Sherwood number for clean bubbles is considered (Eq. (4-18)), the mass transfer rate is overestimated, resulting in a too fast decay of CO<sub>2</sub> molar fraction in the gas phase, not observed experimentally.

On the other hand, when the bubbles are assumed to be contaminated and bubble dynamics is neglected (Case D-), the decay of CO<sub>2</sub> molar fraction is too slow, inasmuch as the trajectory and shape oscillations are not modelled. Expectedly, a better quantitative behaviour is achieved in the Case D+, in which the dynamic Sherwood number is considered. This behaviour is naturally reflected in the resulting CO<sub>2</sub> mass fraction in the liquid phase, as seen in the Figure 5-10. Although no experimental data is available for comparison, the amount of CO<sub>2</sub> transferred to the water in the Case D- is significantly lower than in the Case D+, mainly in the first half of the column, where the driving gradient is still substantial. Afterwards, the phases are almost in equilibrium and the results are similar.

The present model is also compared with simulations from a two-fluid model [96]. As seen in the Figure 5-9, the average CO<sub>2</sub> molar fraction in their case is well overestimated. The mass transfer coefficient used in their simulations was constant for the whole column and taken from the experimental results provided by Deckwer et al. [94]. The problem is that the measurements for the coefficient were performed based on the specific interfacial area at 2 m ( $z/H=0.45$ ), where the bubbles are already much smaller than at the injection. This denotes one advantage on using Euler/Lagrange simulations in bubble columns, inasmuch as the properties are estimated locally and dynamically according the flow conditions.

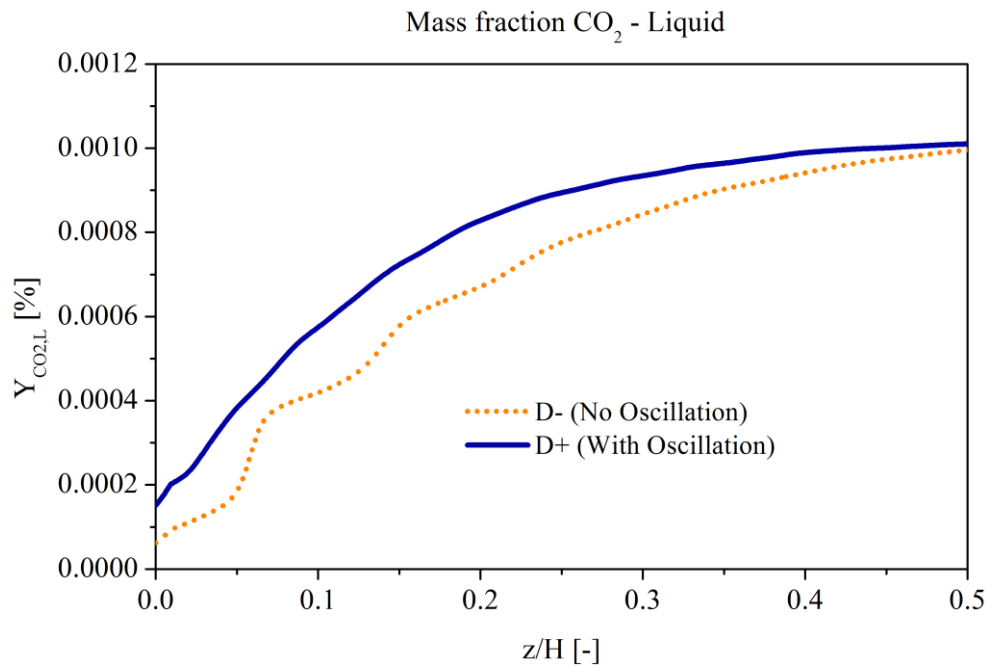


Figure 5-10: Average mass fraction of CO<sub>2</sub> in the liquid phase over the column height.

Furthermore, the average bubble volume fraction is compared with experimental data in the Figure 5-11. Here, the profile is plotted along the centre line of the column (axis). Note that in all simulations a relative high value of volume fraction at the bubble injection is revealed, reaching magnitudes more than 8%. Analogue to the CO<sub>2</sub> molar fraction (Figure 5-9), the volume fraction decreases rapidly due to absorption of gas in the liquid phase. Such behaviour is not found in the experimental data. Nevertheless, as aforementioned, the measurements were performed making use of pressure sensors positioned at side flanges along the column. Hence, the assessment of bubble volume fraction at the column axis may be in this case inappropriate.

In this framework, the same comparison is shown in the Figure 5-12, but extracting the results from cells at the boundary ( $r = 74$  mm). Note that a better agreement with experimental data is observed, not only quantitatively but also qualitatively. This denotes the importance of full connection between experiments and simulation, inasmuch as details should be taken with fidelity.

Moreover, the resulting volume fraction from Case D+ (with bubble dynamics) is lower at the walls than from Case D-, but higher in the core. A similar behaviour was already seen for a case without mass transfer. In order to illustrate the results in the whole domain, colour fields from the average values of bubble volume fraction and diameter are shown in the Figure 5-13. Since the column is 4.4 m height but only 150 mm wide, the images were pressed together in the vertical direction for a better visualization (scale 1:10). Note in the

Figure 5-13a that the case without bubble dynamics (Case D-) presents again some gathering of bubbles at the wall vicinity. This behaviour was already made clear in the section 3.5.3 and will not be discussed here again.

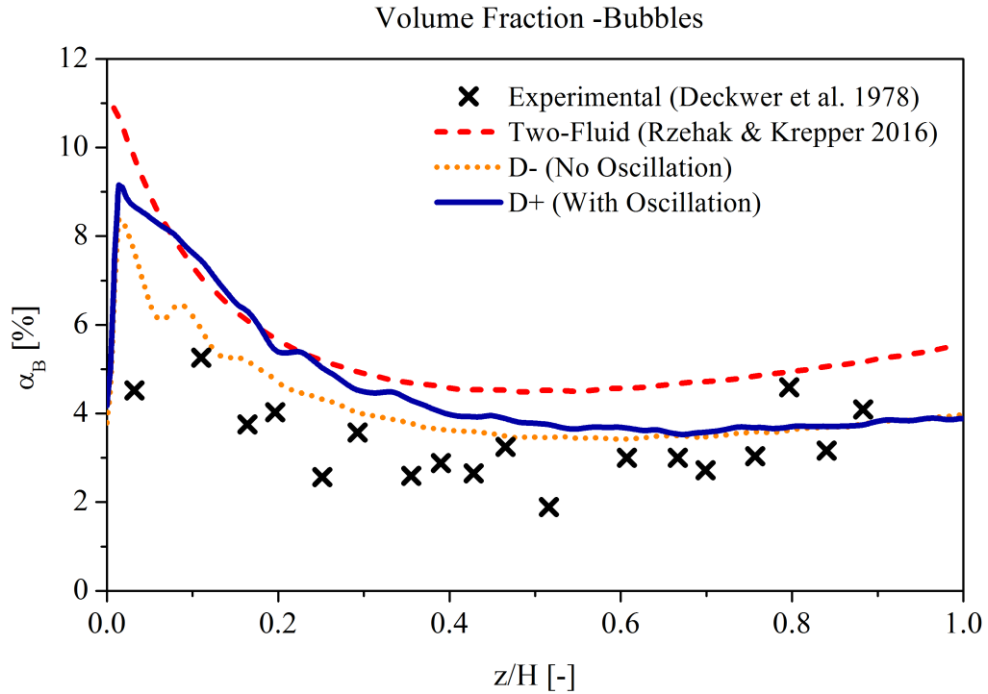


Figure 5-11: Average bubble volume fraction over the column height at the centre line. Experiments: Decker et al. [94]; Two-fluid simulations: Rzehak and Krepper [96].

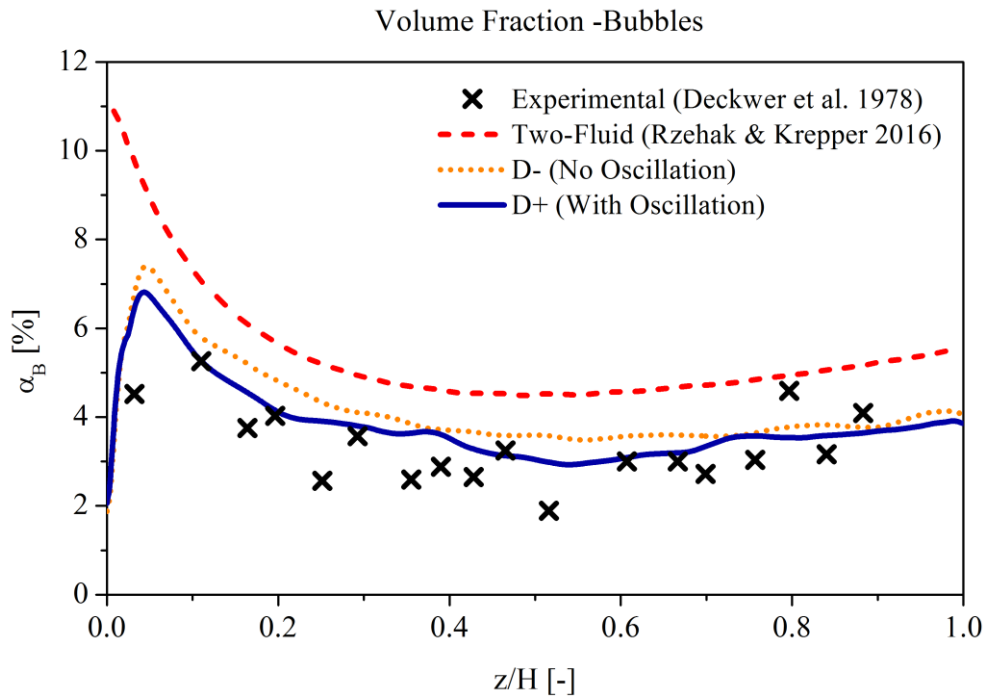


Figure 5-12: Average bubble volume fraction over the column height at the walls. Experiments: Decker et al. [94]; Two-fluid simulations: Rzehak and Krepper [96].

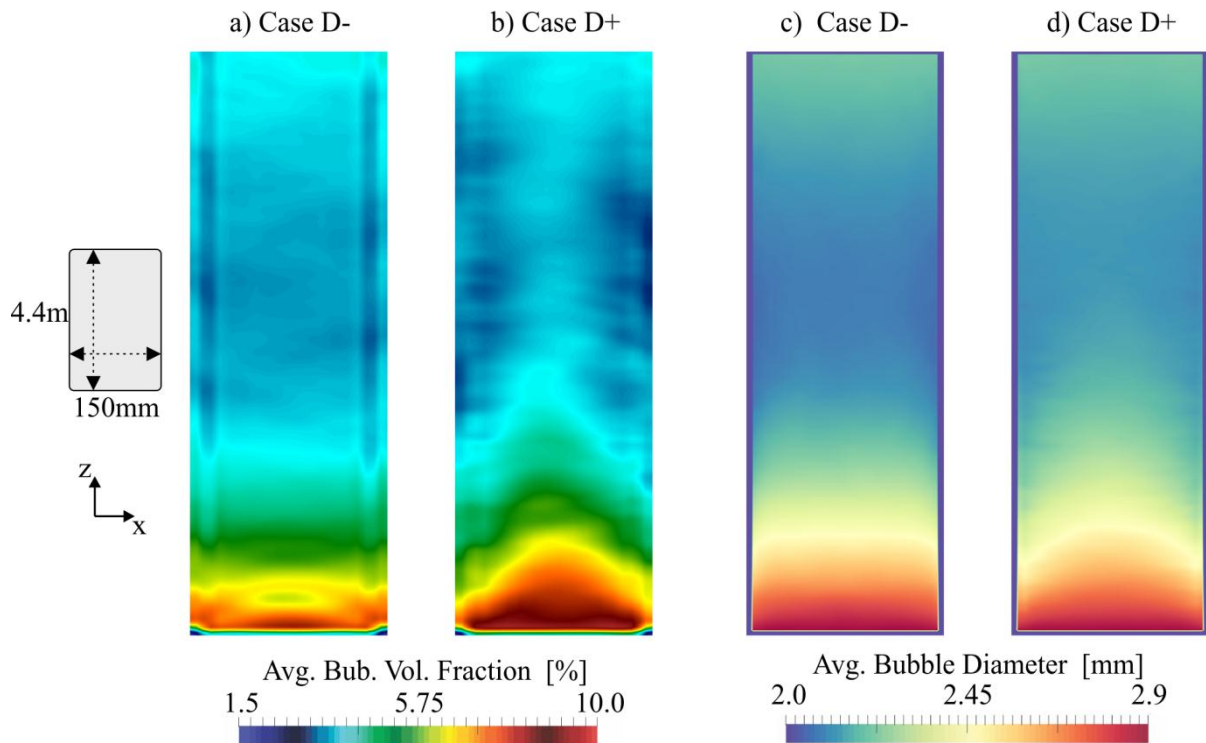


Figure 5-13: Colour fields from Cases D- (no osc.) and D+ (with osc.) in terms of bubble: a and b) volume fraction; c and d) diameter.  $j_g = 0.0275$  m/s.  $j_L = 0.0472$  m/s.

Nevertheless, in the third chapter of this work, bubble columns with initial water levels only up to 700mm were evaluated. As seen in the Chapter 3, the bubbles were at 700 mm still dispersing in the domain, and the flow had still influence from the injection and the free surface at the top. In the present study case, on the other hand, the column extends its height for 4.4m, which is a substantial difference. The resulting average liquid velocities from Cases D- and D+ in vertical and tangential directions are shown in the Figure 5-14. Here, the dashed white line in the Figure 5-14a and b represent a cross-section at the height of 700 mm, equivalent to the bubble column presented in the section 3.5. Note that when bubble dynamics is considered (Case D+) a preferential core flow is maintained along the entire column, differently than the Case D- where an almost uniform profile is found. The reason for that is the occurring of a swirl due to the water inlet around the aerator, as seen in the Figure 5-14d, which is sustained for a longer time only when the bubbles do not “stick” at the walls and are brought back to the core by the oscillation model. Although a weak zig-zag or spiral motion is observed in the Case D- (Figure 5-14c), no preferential direction from a swirl is established. Once the phases are coupled, the same phenomenon is reflected in the bubble velocities, as seen in the Figure 5-15, inasmuch as they are qualitatively identical.

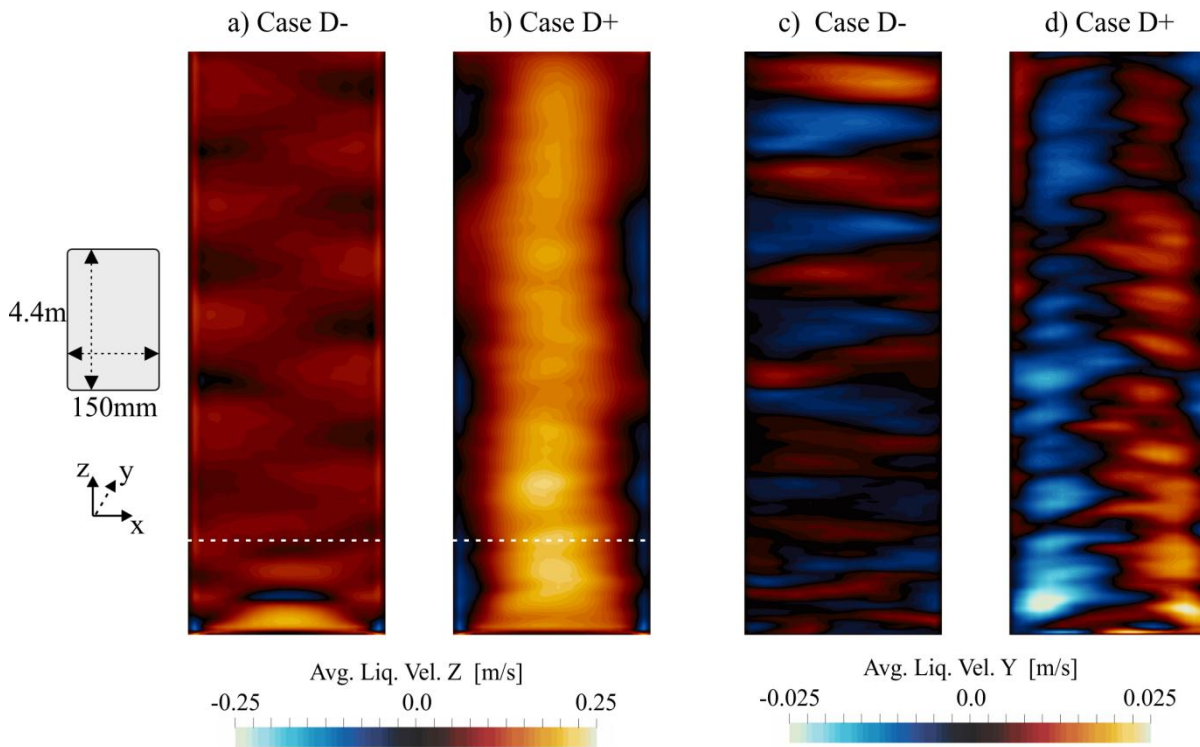


Figure 5-14: Colour fields from Cases D- (no osc.) and D+ (with osc.) in terms of:  
 a and b) liquid vertical velocity; c and d) liquid tangential velocity.  
 $j_g = 0.0275$  m/s.  $j_L = 0.0472$  m/s. Dashed white line: axial position at 700 mm.

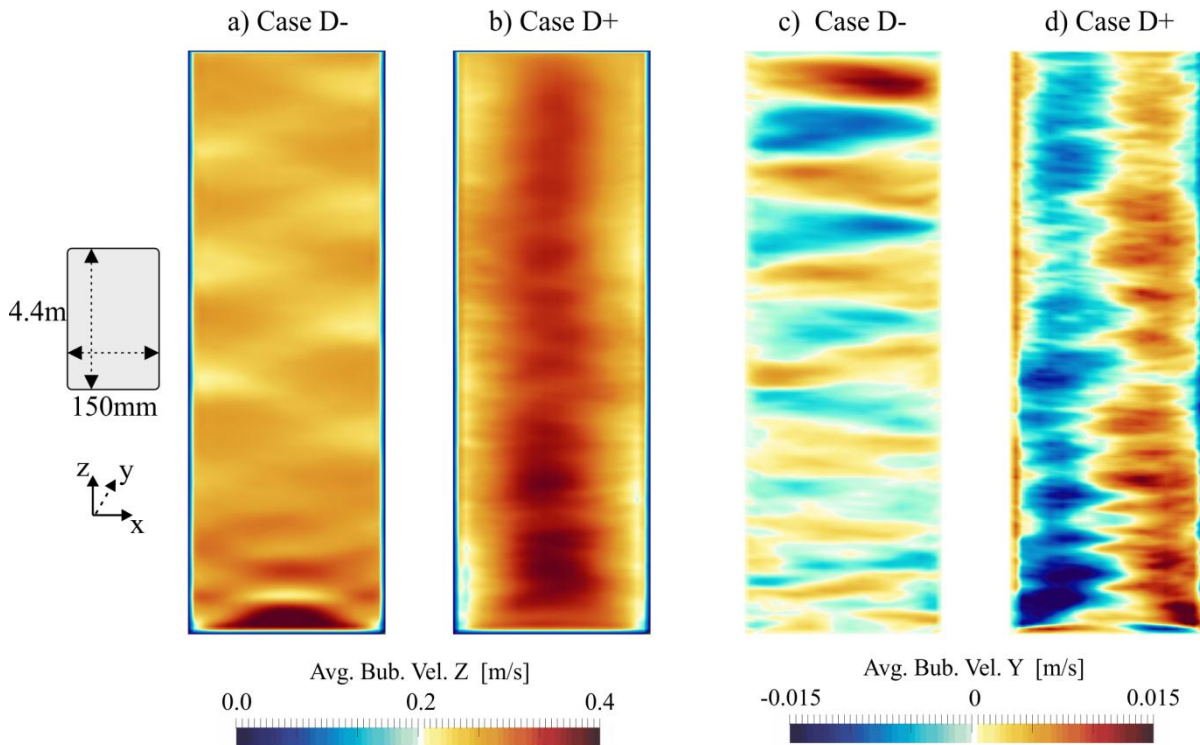


Figure 5-15: Colour fields from Cases D- (no osc.) and D+ (with osc.) in terms of:  
 a) and b) bubble vertical velocity; c) and d) bubble tangential velocity.  
 $j_g = 0.0275$  m/s.  $j_L = 0.0472$  m/s.

This last study case is one more example that shows the importance of modelling bubble oscillations on the frame of Euler/Lagrange approach. Since the final use of Computational Fluid Dynamics is pointed to industrial applications, all the phenomena should be properly included in the modelling. In the case of bubble columns, higher efficiencies and product selectivity are definitely the ambition from engineers. Before including reactions in the simulations, motion and mass transfer should be accurately represented, otherwise the validation process can lead to wrong conclusions.

### 5.3 Conclusions of the chapter

Finally, the CFD model proposed in the Chapter 2 was here extended for situations with mass transfer (Chapter 4) and two study cases were used as model validation.

In the first study case [48], a transient evaluation of bubble volume was performed. The experiments consist of isolated and clean CO<sub>2</sub> bubbles rising in water. Simulations were conducted considering different possibilities of phenomena involved, such as totally degassed water and pure CO<sub>2</sub>, commercial CO<sub>2</sub>, and back-diffusion of argon into the liquid. Furthermore, when the effects of trajectory oscillation were neglected in the calculations, slightly lower mass transfer rates were obtained. The inclusion of trajectory oscillation, bubble eccentricity and a dynamic Sherwood number [31] improved the results, indeed. However, the effect becomes only notable for larger bubbles, where shape and trajectory oscillations are actually present.

The second study case evaluated in this chapter [94], differently from many experimental works in the literature, consists of a relatively tall bubble column. Additionally, the liquid used in the experiments is tap water, operating with co-current flow with the gas. In this manner, the mass transfer model was adapted for contaminated bubbles. Nevertheless, the effect of oscillation amplitude is accounted for. While the discrepancy by considering or not bubble dynamics was in the first study case apparently small, a different scenario was revealed for bubble swarms, when a more complex interaction between the phases is expected.



# Conclusions and Outlook

In this doctoral thesis, a CFD model dedicated for bubble columns in the frame of Euler/Lagrange approach was successfully implemented in the platform OpenFOAM (v4.1). Despite the use of “point-mass” approximations, the model accounts for effects of bubble dynamics on motion and mass transfer. Numerical results obtained for four experimental study cases [11,54,48,94], which were used for model validation. Each study case supported a different aspect of evaluation, by varying bubble size (0.5~9 mm), gas superficial velocity (0.0028~0.0275 m/s), geometry (circular and rectangular) and temperature (14~25°C). Furthermore, the bubble column from the last study case operates with liquid co-current flow.

Although the main focus of this work was bubble dynamics, this is only one part among many other pieces that compose the whole model. As aforementioned, the standard OpenFOAM libraries and the code structure were very useful as a basis for the model implementation. However, there was no standard solver for bubbly flows in the frame of Euler/Lagrange approach. Due to this very fact, the slow and constant implementation process provided the opportunity to understand and perceive the effect of each development on the numerical results.

Aiming on capturing the trajectory oscillations of bubbles, a set of relevant forces acting on bubbles were established in the simulations, such as buoyancy/gravity, drag, added mass, Basset, transversal lift, fluid inertia and the fictitious wall force. Even though, since the resistance coefficients for such forces are from stationary behaviour, path oscillations cannot be achieved with the *parcel-in-cell* (PIC) characteristic of the Euler/Lagrange approach, by not resolving the liquid flow at the bubble level. Modelling the contribution of the SGS turbulence (TDM) in the velocity seen by the bubbles and perturbation of these in the SGS turbulence (BIT), marginally improved the final results for the bubble phase. However, significant changes were observed in the liquid phase, once the enhancement of turbulent viscosity is performed. It may be relevant to comment here, that in the BIT model implemented, only production of SGS turbulence can be promoted by the bubble motion, but no dissipation. Such possibility was not considered in this work, but remains as suggestion for future works.

After all, only with the estimation of bubble eccentricity and modification of motion angle (bubble dynamics model) was possible to achieve reasonable path oscillations, such as those observed experimentally. The prediction of these properties through a single-step Langevin equation affords a stochastic variation yet correlated in time. Although parameters

from empiric precedence with regard to oscillation frequencies and amplitudes are necessary, the numeric calculation can be handled in a simple way. For example, only the actual value of eccentricity and motion angle need to be stored for each individual parcel, differently than the Basset force, which requires the information of  $n$  previous time-steps.

The consideration of bubble dynamics improved the numerical results with regard to horizontal oscillations, indeed. In the lateral direction, the major contribution comes from motion deviation imposed by the model. The variation of bubble eccentricity alone could not yield the results seen here. However, its main effect comes through the calculation of drag, added mass and lift coefficients, combined with the trajectory oscillation.

In this framework, the forces competition presented in the section 3.3 revealed that added mass and Basset forces are much more relevant than observed without bubble dynamics. This may be one factor why the Basset force is often neglected in simulations, although large attention is given to the lift force, even presenting lower magnitudes than Basset. Besides, the enhancement of added mass and the history force is more remarkable for bubble sizes in the transition of rectilinear to oscillating behaviour, where higher frequencies are expected. For larger bubbles this effect is reduced, when compared to the buoyancy increment.

Moreover, the impact of the Basset force in the average bubble velocities is apparently insignificant. The RMS values of velocity fluctuations, on the other hand, were clearly affected. Once this force acts against the change of motion, bubble fluctuations imposed by the oscillation model were reduced. Following our intuition, weaker velocity fluctuations would yield less lateral dispersion. Surprisingly, the average contribution of the Basset force in the radial direction revealed to be towards the wall, resulting in a higher lateral dispersion of bubbles.

This very behaviour was also found in a constraint case, in which droplets are let from a point source in a turbulent pipe flow. Here, three scenarios were evaluated, where the droplets could be buoyant, inert or heavier than the water. In all the cases, the history force enhanced the lateral displacement and reduced the velocity fluctuations. Nevertheless, the major effect of the Basset force on the lateral dispersion is noticed close to the droplet injection, and loses influence at longer times. However, the initial circumstances are reflected during the whole droplet trajectory.

From a merely numerical point of view, the geometry of bubble columns is usually simple, inasmuch as one cylinder or one box is sufficient to represent the domain. On the other hand, the multiphase peculiarity in such apparatus can difficult the calculations in the

frame of LES-Euler/Lagrange approach. Contradictory to the use of LES, since small grid sizes are required to resolve all the large turbulent scales, the bubble diameter should be in rigor much smaller than the mesh cells. This issue is exposed in the section 3.5, where a thin column is combined with a bubble size distribution up to 9 mm. Here, an attempt of smoothing the volume fraction field in a finer grid by distributing the volume of bubbles by the neighbour cells could avoid numerical divergence and improve the results, when compared to results with a coarse mesh.

In this same case, the hybrid solution by resolving the free surface and the continuous gas phase above the water level was also prejudiced. The discrete and large bubbles ( $d_B > 6\text{mm}$ ) emerging at the interface promoted the entrainment of the continuous gas into the liquid excessively, inasmuch as the simple interface compression method was not sufficient anymore to separate the phases properly. Accepting this as limitation, a satisfactory solution for this case was obtained by simply deactivating the VoF aspect from the model. Nevertheless, influence from this fixed boundary can be present. This problem was not a point of interest of the present work, but the implementation of a more sophisticated VoF method, e.g., with surface reconstruction, remains as suggestion for future works.

In the Chapter 4, the hydrodynamic model was further developed by including mass transfer. Here, the model complexity does not only grow by having additional equations to be solved, but also by having more details to pay attention for.

Even for the case of a single bubble, as exposed in the section 5, the properties which were assumed in the hydrodynamic situation constant, such as diameter, density and mean eccentricity, are now changing at each Lagrangian time-step. In this manner, the parametric sensibility of the numerical solution is much higher. Additionally, irrespective of mass transfer correlations assumed in the model, the proper input of thermodynamic properties is essential for the reliability of the results. For example, it is common assumed in the literature that the pressure changes due to the hydrostatic head in laboratory columns are negligible and, thus, bubble is presumed incompressible. Such affirmation cannot be true. Otherwise, the calculation of the initial mass of the species inside the bubble at the column bottom will be underestimated. Subsequently, the resulting decay of mass along the rise will produce a faster dissolution of the bubble than actually expected. Furthermore, a full connection between experiments and simulations is fundamental, inasmuch as the information about the pressure and temperature when the experiments were performed should be always available and precise. For example, only a difference of  $5^\circ\text{C}$  can change the solubility of  $\text{CO}_2$  in the water around 10%.

In the study case of single bubbles, simulations were conducted considering up to three chemical species involved, in which  $\text{CO}_2$  and  $\text{N}_2$  are dissolving into the water and Ar is being diffused from the liquid to the bubble. Once three bubble initial sizes were evaluated (1.9~3.0mm), the effect of oscillation amplitude on the mass transfer rate could be discerned between the bubble sizes, in which a faster decay of volume is related with larger values of eccentricity. The enhancement of mass transfer through the consideration of a dynamic Sherwood number improved the results, indeed. Nevertheless, just evaluating one single bubble, the discrepancy between considering bubble oscillation or not is apparently small. However, it is expected than in a bubble swarm the effect is more notable.

In the last study case evaluated in this work [94], the affirmation above was confirmed. Bubbles with initial mean diameters around 2.9mm were injected in co-current flow with tap water in a relatively tall bubble column (4.4m). One interesting part from that was that a pseudo-steady state is observed, where the equilibrium between bubble and liquid phases is reached at the half of the column height. Due to the hydrostatic head effects, a “back-diffusion” from the same chemical specie starts to occur after the equilibrium. Furthermore, since tap water was used in the experiments, a proper correlation for the Sherwood number that represents the mass transfer on contaminated bubbles was required. Even though, the effect of bubble oscillation was considered and the difference was substantial.

After all, the application of “point-mass” approximations for modelling the flow and mass transfer phenomenon was successfully performed, inasmuch as the numerical results are in well agreement with experimental data. Within the purposes of this work, the range of bubble size, volume fraction, flow conditions and geometries evaluated here the proposed model is assumed validated. Although the objective of highlighting the importance of modelling bubbles dynamics in the frame of Euler/Lagrange approach was here succeeded, a lot of effort still needs to be done in the future, in order to be able of simulating bubble columns with all the phenomena involved. In this thesis, many aspects have been neglected or avoided, e.g., bubble collisions, coalescence/break-up, chemical reactions, enhancement of mass transfer due to chemical reactions, possible presence of solid particles (three-phase flow). All of these phenomena have been constantly studied in the literature, and remain also as suggestion for further development of the present model.

# Nomenclature

$\Delta r$	= spatial separation [m]
$\Delta t$	= time step [s]
$\Delta x$	= Eulerian grid size [m]
$A, B$	= angular coefficients [-]
$A_e$	= superficial area of ellipsoid [m <sup>2</sup> ]
$a, b$	= linear regression parameters [-]
$a, c$	= bubble major and minor axis, respectively [-]
$C$	= coefficient, constant [-]
$Ca$	= Capillary number [-]
$D_{ij}$	= Diffusivity constant of the specie $i$ in the specie $j$ [m <sup>2</sup> s <sup>-1</sup> ]
$d$	= diameter [m]
$E$	= bubble axis ratio ( $0 < E \leq 1$ ) [-]
$Eo$	= Eötvös number [-]
$f$	= derivative of slip velocity in time [m s <sup>-2</sup> ]
$g$	= gravitational acceleration vector [m s <sup>-2</sup> ]
$H$	= dimensionless Henry's constant [-]
$I$	= identity matrix [-], Integral constant [-]
$K$	= Basset integration kernel [s <sup>-1</sup> ]
$k$	= unit vector parallel to the wall [-]
$k$	= mass transfer coefficient [m s <sup>-1</sup> ]
$k$	= turbulent kinetic energy [m <sup>2</sup> s <sup>-2</sup> ]
$L_E$	= length scale of SGS turbulence [m]
$M$	= Morton number [-]
$m$	= mass [kg]
$N$	= number of real bubbles in the parcel [-]
$n$	= unit normal vector to the wall [-]
$Pe$	= Peclet number [-]
$p$	= pressure of continuous phase [kg m <sup>-1</sup> s <sup>-2</sup> ], fitting parameter [-]
$Q_g$	= volumetric gas flow rate [L h <sup>-1</sup> ]
$R$	= universal constant of gases [m <sup>3</sup> Pa kmol <sup>-1</sup> K <sup>-1</sup> ]
$Re$	= Reynolds number [-]
$R_p, R_\chi, R_\delta$	= correlation functions [-]

$Sc$	= Schmidt number [-]
$Sh$	= Sherwood number [-]
$Sl$	= Strouhal number [-]
$Sr$	= Shear [ $s^{-1}$ ]
$\overline{S_{i,j}}$	= symmetric deviatoric part of strain tensor [ $s^{-1}$ ]
$\overline{S_{u,p}}$	= momentum source terms [ $kg\ m^{-2}\ s^{-2}$ ]
$S'_{Y,l,p}$	= chemical specie source terms [ $kg\ m^{-3}\ s^{-1}$ ]
$S_{k,p}$	= turbulent kinetic energy source terms [ $kg\ m^{-1}\ s^{-3}$ ]
$St^*$	= modified Stokes number [-]
$T$	= temperature [K]
$T_L$	= time scale of SGS turbulence [s]
$t$	= time [s]
$\mathbf{u}$	= velocity vector [ $m\ s^{-1}$ ]
$\acute{u}$	= fluctuating liquid velocity seen by the bubble [ $m\ s^{-1}$ ]
$V$	= volume [ $m^3$ ]
$W$	= molecular weight [ $kg\ kmol^{-1}$ ]
$We$	= Weber number [-]
$\mathbf{x}$	= position [m]
$x$	= distance from the wall [m]
$Y$	= mass fraction [-]
$\acute{Y}$	= fluctuating SGS mass fraction [-]
$\alpha$	= volume fraction [-], initial motion angle [degrees]
$\beta$	= bubble orientation angle [degrees]
$\gamma$	= final motion angle [degrees]
$\Delta$	= LES delta [m]
$\delta$	= motion angle deviation [degrees]
$\delta_{ij}$	= Kronecker-delta [-]
$\epsilon$	= coefficient of restitution [-], dissipation rate of the turbulent kinetic energy [ $m^2\ s^{-3}$ ]
$\mu$	= absolute viscosity [ $kg\ m^{-1}\ s^{-1}$ ]
$\xi$	= Gaussian random number [-]
$\rho$	= density [ $kg\ m^3$ ]
$\sigma$	= surface tension, [ $kg\ s^{-2}$ ]
$\sigma_c$	= rms value of liquid velocity fluctuation [ $m\ s^{-1}$ ]

$\sigma_\chi$	= rms value of bubble eccentricity [-]
$\sigma_\gamma$	= rms value of bubble motion angle [degrees]
$\boldsymbol{\tau}_c$	= stress tensor [ $\text{kg m}^{-1} \text{s}^{-2}$ ]
$\tau_B$	= drag response time [s]
$\tau_{\text{osc}}$	= bubble oscillation period [s]
$\tau$	= Basset integration time [s]
$\chi$	= eccentricity ( $\chi \geq 1$ ) [-]

### <Subscripts>

AM	= added mass
B	= bubble, discrete bubble phase, Basset
BW	= wall
CV	= control volume
c	= continuous phase, critical
D	= drag
E	= Eulerian
<i>eff</i>	= effective
g	= gas phase
h	= major axis
<i>i</i>	= component in the <i>i</i> direction, <i>i</i> -th chemical specie
<i>j</i>	= component in the <i>j</i> direction, <i>j</i> -th chemical specie
k	= k-th parcel
L	= Lagrangian, continuous liquid phase, lift
osc	= oscillation
<i>pa</i>	= parallel to the wall
<i>pe</i>	= perpendicular to the wall
S	= Smagorinsky
SGS	= sub-grid-scale
t	= turbulent
<i>t,p</i>	= turbulent contribution by the bubbles
$\epsilon$	= dissipation
$\infty$	= bulk

<Superscripts>

$n$  = number of time step

$sat$  = saturation

$T$  = transposed

<Modifiers>

— = mean value, averaged value



# References

- [1] C. T. Crowe, J. D. Schwarzkopf, M. Sommerfeld, and Y. Tsuji, *Multiphase Flows with Droplets and Particles*, 2nd ed. Boca Raton, U.S.A.: CRC Press, 2012.
- [2] A. Lapin and A. Lübbert, "Numerical Simulation of the dynamics of two-phase gas-liquid flows in bubble columns," *Chem. Eng. Science*, vol. 49, pp. 3661-3674, 1994.
- [3] S. Lain, D. Bröder, M. Sommerfeld, and M. F. Göz, "Modelling hydrodynamics and turbulence in a bubble column using the Euler-Lagrange procedure.," *International Journal of Multiphase Flows*, vol. 28, pp. 1381-1407, 2002.
- [4] N. G. Deen, T. Solberg, and B. H. Hjertager, "Large Eddy Simulation of the Gas-Liquid Flow in a Square Cross-Sectioned Bubble Column," *Chemical Engineering Science*, vol. 56, pp. 6341-6349, 2001.
- [5] D. Darmana, N. G. Deen, and J. A. M. Kuipers, "Detailed modeling of hydrodynamics, mass transfer and chemical reactions in a bubble column using a discrete bubble model," *Chem. Eng. Science*, vol. 60, pp. 3383-3404, 2005.
- [6] A. Sokolichin and G. Eigenberger, "Gas-Liquid Flow in Bubble Columns and Loop Reactors: Part I. Detailed Modelling and Numerical Simulation," *Chemical Engineering Science*, vol. 49, pp. 5735-5746, 1994.
- [7] R. F. Mudde and O. Simonin, "Two- and Three-Dimensional Simulations of a Bubble Plume Using a Two-Fluid Model," *Chemical Engineering Science*, vol. 54, pp. 5061-5069, 1999.
- [8] D. Lucas, E. Krepper, and H.-M. Prasser, "Use models for lift, wall and turbulent dispersion forces acting on bubbles for poly-disperse flows," *Chemical Engineering Science*, vol. 62, pp. 4146-4157, 2007.
- [9] R. Rzehak et al., "Baseline Model for the Simulation of Bubbly Flows," *Chemical Engineering Technology*, vol. 38, no. 11, pp. 1972-1978, 2015.
- [10] D. Jain, J. A. M. Kuipers, and N. G. Deen, "Numerical study of coalescence and breakup in a bubble column using a hybrid volume of fluid and discrete bubble model approach," *Chem. Eng. Science*, vol. 119, pp. 134-146, 2014.
- [11] M. Sommerfeld, E. Bourloutski, and D. Bröder, "Euler/Lagrange Calculations of Bubbly Flows with Consideration of Bubble Coalescence," *The Canadian Journal of Chemical Engineering*, vol. 81, pp. 508-518, 2003.
- [12] S. Radl and J. G. Khinast, "Multiphase Flow and Mixing in Dilute Bubble Swarms," vol. 56, pp. 2421-2445, 2010.
- [13] M. C. Gruber, S. Radl, and J. G. Khinast, "Rigorous modelling of CO<sub>2</sub> absorption and chemiapsorbtion: The influence of bubble coalescence and breakage," *Chem. Eng. Science*, vol. 137, pp. 188-204, 2015.
- [14] M. T. Dhotre, N. G. Deen, B. Niceno, Z. Khan, and J. B. Joshi, "Large Eddy Simulations for Dispersed Bubbly Flows: A Review," *Int. J. Chem. Eng.*, 2013.
- [15] J. Smagorinsky, "General circulation experiments with the primitive equations, 1. The

basic experiment," *Monthly Weather Review*, vol. 91, pp. 99-164, 1963.

- [16] Y. Sato and K. Sekoguchi, "Liquid velocity distribution in two-phase bubble flow," *International Journal of Multiphase Flow*, vol. 2, no. 1, pp. 79–95, 1975.
- [17] Y. Sato, M. Sadatomi, and K. Sekoguchi, "Momentum and heat transfer in two-phase bubble flow-I. Theory," *International Journal of Multiphase Flow*, vol. 7, no. 2, pp. 167–177, 1981.
- [18] B. Niceno, M. T. Dhotre, and N. G. Deen, "One-equation sub-grid scale (SGS) modelling for Euler-Euler large eddy simulation (EELES) of dispersed bubbly flow," *Chemical Engineering Science*, vol. 63, no. 15, pp. 3923–3931, 2008.
- [19] J. Lipowsky and M. Sommerfeld, "LES-simulation of the formation of particles strands in swirling flows using an unsteady Euler-Lagrange approach," in *Proceedings of the 6th International Conference on Multiphase Flow, ICMF2007*, Leipzig, Germany, 2007.
- [20] M. Sommerfeld, B. van Wachem, and R. Oliemans, *Best Practice Guidelines for Computational Fluid Dynamics of Dispersed Multiphase Flows*. Brussels, 2008.
- [21] M. R. Maxey and J. J. Riley, "Equation of motion for a small rigid sphere in a non-uniform flow," *Phys. Fluids*, vol. 26, pp. 883-889, 1983.
- [22] M. Ishii and N. Zuber, "Drag coefficient and relative velocity in bubbly, droplet or particulate flows," vol. 25, no. 5, pp. 843-855, 1979.
- [23] Renwei Mei, James F. Klausner, and Christopher J. Lawrence, "A note on the history force on a spherical bubble at finite Reynolds number," *Phys. Fluids*, vol. 6, no. 1, pp. 418-420, January 1994.
- [24] A. Tomiyama, I. Kataoka, I. Zun, and T. Sakaguchi, "Drag coefficients of single air bubbles under normal and microgravity conditions," in *JSME Int. J. Ser. B 41*, 1998, pp. 472–479.
- [25] X. Yan et al., "Drag Coefficient Prediction of a Single Bubble Rising in Liquids," *Ind. Eng. Chem. Res.*, vol. 57, pp. 5385-5393, 2018.
- [26] D. W. Moore, "The velocity rise of distorted gas bubbles in a liquid of small viscosity," *J. Fluid Mech.*, vol. 23, pp. 749-766, 1965.
- [27] Marie Rastello, Jean-Louis Marié, and Michel Lance, "Drag and lift forces on clean spherical and ellipsoidal bubbles in a solid-body rotating flow," *Journal of Fluid Mechanics*, vol. 682, pp. 434-459, 2011.
- [28] S. Aoyama, K. Hayashi, S. Hosokawa, and A. Tomiyama, "Shapes of ellipsoidal bubbles in infinite stagnant liquids," *International Journal of Multiphase Flow*, vol. 79, pp. 23-30, 2016.
- [29] H. Lamb, *Hydrodynamics*. New York: Cambridge University Press, 1932.
- [30] M. Simcik, M. C. Ruzicka, and J. Drahoš, "Computing the added mass of dispersed particles," *Chem. Eng. Science*, vol. 63, pp. 4580-4595, 2008.
- [31] A. Tomiyama, H. Tamai, I. Zun, and S. Hosokawa, "Transverse migration of single bubbles in simple shear flows," *Chem. Eng. Science*, vol. 57, pp. 1849-1858, 2002.
- [32] S. Aoyama, Z. Iztok, K. Hayashi, S. Hosokawa, and A. Tomiyama, "Lift force acting on single bubbles in linear shear flow," in *9th International Conference on Multiphase*

*Flow*, Firenze, Italy, 2016, 22nd-27th May.

- [33] S. Aoyama, K. Hayashi, S. Hosokawa, D. Lucas, and A. Tomiyama, "Lift force acting on single bubbles in linear shear flows," *International Journal of Multiphase Flow*, vol. 96, pp. 113-122, 2017.
- [34] D. Legendre and J. Magnaudet, "The lift force on a spherical bubble in a viscous linear shear flow," *J. Fluid. Mech.*, vol. 368, pp. 81-126, 1998.
- [35] T. Ziegenhein, A. Tomiyama, and D. Lucas, "A new measuring concept to determine the lift force for distorted bubble in low Morton number system: Results for air/water," *International Journal of Multiphase Flow*, vol. 108, pp. 11-24, 2018.
- [36] Fumio Takemura and Jacques Magnaudet, "The transverse force on clean and contaminated bubbles rising near a vertical wall at moderate Reynolds number," *J. Fluid Mech.*, vol. 495, pp. 235-253, 2003.
- [37] S. P. Antal, R. T. Lahey Jr, and J. E. Flaherty, "Analysis of Phase Distribution in Fully Developed Laminar Bubbly Two-phase Flow," *Int. J. Multiphase Flow*, vol. 17-5, pp. 635-652, 1991.
- [38] A. Tomiyama, A. Sou, I. Žun, N. Kanami, and T. Sakaguchi, "Effects of Eötvös Number and Dimensionless Liquid Volumetric Flux on Lateral Motion of a Bubble in a Laminar Duct Flow," *Advances in Multiphase Flow*, pp. 3-15, 1995.
- [39] S. Hosokawa, A. Tomiyama, S. Misaki, and T. Hamada, "Lateral Migration of Single Bubbles Due to the Presence of Wall," in *Proc. ASME Joint U.S.-European Fluids Engineering Division Conference, FEDSM2002*, Montreal, Canada, 2002.
- [40] Hyeonju Jeong and Hyungmin Park, "Near-wall rising behaviour of a deformable bubble at high Reynolds number," *Journal of Fluid Mechanics*, vol. 771, 2015.
- [41] E. E. Michaelides, "A novel way of computing the Basset term in unsteady multiphase flow computations," *Physics of Fluids*, vol. 4, no. 7, pp. 1579-1582, 1992.
- [42] M. A. T. van Hinsberg, J. H. M. ten Thije Boonkkamp, and H. J. H. Clercx, "An efficient, second order method for the approximation of the Basset history force," *Journal of Computational Physics*, vol. 230, pp. 1465-1478, 2011.
- [43] Efstathios Michaelides and Adam Roig, "A Reinterpretation of the Odar and Hamilton Data on the Unsteady Equation of Motion of Particles," *AIChE Journal*, vol. 57, pp. 2997-3002, 2011.
- [44] F. Odar and W. S. Hamilton, "Forces on a sphere accelerating in a viscous fluid," *J. Fluid. Mech.*, vol. 18, pp. 302-314, 1964.
- [45] Knud Lunde and Richard J. Perkins, "Shape Oscillations of Rising Bubbles," *Applied Scientific Research*, vol. 58, pp. 387-408, 1998.
- [46] K. Ellingsen and F. Risso, "On the rise of an ellipsoidal bubble in water: Oscillatory paths and liquid-induced velocity," *J. Fluid Mech.*, vol. 440, pp. 235-268, 2001.
- [47] M. Wu and M. Gharib, "Experimental studies on the shape and path of small air bubbles rising in clean water," *Physics of Fluids*, vol. 14, pp. L49-L52, 2002.
- [48] D. Merker, L. Böhm, M. Oßberger, P. Klüfers, and M. Kraume, "Mass Transfer in Reactive Bubbly Flows – A Single-Bubble Study," *Chemical Engineering Technology*,

vol. 40, pp. 1391-1399, 2017.

- [49] T. Reichardt and M. Sommerfeld, "Stereoskopische Aufnahmen zur Analyse der Blasenoszillation," *Chemie Ingenieur Technik*, pp. 1327-1328, October 2008.
- [50] T. Reichardt and M. Sommerfeld, "Stereoscopic imaging for analyzing bubble oscillation in turbulence," in *14th International Symposium Application of Laser Techniques to Fluid Mechanics*, Lisbon, 2008.
- [51] T. Reichardt, *Multiscale Euler/Lagrange approach to simulate finite-sized solid particles and bubbles as well as numerical and experimental studies to improve the modeling of complex bubble motion*. Magdeburg, 2017.
- [52] M. Sommerfeld, M. Muniz, and T. Reichardt, "On the Importance of Modelling Bubble Dynamics for Point-mass Numerical Calculations of Bubble Columns," *Journal of Chemical Engineering of Japan*, 2018.
- [53] E. Leon-Becerril, A. Cockx, and A. Line, "Effect of bubble deformation on stability and mixing in bubble columns," *Chemical Engineering Science*, vol. 57, pp. 3283-3297, 2002.
- [54] M. H. bin Mohd Akbar, K. Hayashi, S. Hosokawa, and A. Tomiyama, "Bubble Tracking Simulation of Bubble-Induced Pseudo Turbulence," *Multiphase Science and Technology*, vol. 24, pp. 197-222, 2012.
- [55] E. Bourloutski and M. Sommerfeld, "Modelling of Bubble Tumbling Motion in the Frame of the Euler/Lagrange Approach," in *Proc. of the 6th Japanese/German Symposium on Bubble Columns*, Nara, Japan, 2003.
- [56] M. Sommerfeld and D. Bröder, "Analysis of hydrodynamics and micro-structure in a bubble column by planar shadow image velocimetry," *Industrial & Engineering Chemistry Research*, vol. 48, pp. 330-340, 2009.
- [57] H. K. Versteeg and W. Malalasekera, *An introduction to Computational Fluid Dynamics*, 2nd ed. England: Pearson Education Limited, 2007.
- [58] E. Loth, "Quasi-steady shape and drag of deformable bubbles and drops," *Int. J. Multiphase Flow*, vol. 34, no. 6, pp. 523-546, 2008.
- [59] W. Dijkhuizen, M. van Sint Annaland, and J.A.M. Kuipers, "Numerical and experimental investigation of the lift force on single bubbles," *Chemical Engineering Science*, vol. 65, pp. 1274-1287, 2010.
- [60] R. Zenit and D. Legendre, "The coefficient of restitution for air bubbles colliding against solid walls in viscous liquids," *Physics of Fluids*, vol. 21, 2009.
- [61] T. von Karman and L. Horwarth, "On the statistical theory of isotropic turbulence," *Proc. Royal Society London*, pp. 192-215, 1938.
- [62] D. K. Lilly, "The representation of small scale turbulence in numerical simulation experiments," *Proceedings of the IBM Scientific Computing Symposium on Environmental Sciences*, 1967.
- [63] J. W. Deardorff, "Stratocumulus-capped mixed layer derived from a three dimensional model," *Boundary-Layer Meteorology*, vol. 18, pp. 495 – 527, 1980.
- [64] M. Sommerfeld, *Numerical Methods for Dispersed Multiphase Flows*. In: Bodnár T.,

Galdi G., Nečasová Š. (eds) *Particles in Flows. Advances in Mathematical Fluid Mechanics*. Birkhäuser, Cham., 2017.

- [65] Joel H. Ferziger and Milovan Perić, *Numerische Strömungsmechanik*. Heidelberg, Berlin: Springer, 2008.
- [66] M. Milleli, B. Smith, and D. Lakehal, "Large Eddy Simulation of Turbulent Shear Flows Laden with Bubbles," in *Direct and Large-Eddy Simulation IV, ERCOFTAC Series*, vol. 8, 2001, pp. 461-470.
- [67] R. M. Wellek, A. K. Agrawal, and A. H. P. Skelland, "Shape of liquid drops moving in liquid media," *AIChE Journal*, vol. 12, no. 5, pp. 854-862, 1966.
- [68] T. Ziegenhein and D. Lucas, "Observations on bubble shapes in bubble columns under different flow conditions," *Experimental Thermal and Fluid Science*, vol. 85, pp. 248–256, 2017.
- [69] R. V. Calabrese and S. Middleman, "The Dispersion of a Discrete Particle in a Turbulent Fluid Field," *AIChE Journal*, vol. 25, no. 6, pp. 1025-1035, November 1979.
- [70] M. Sommerfeld, *Modellierung und numerische Berechnung von partikelbeladenen turbulenten Strömungen mit Hilfe des Euler/Lagrange-Verfahrens*. Aachen, Germany: Shaker Verlag, 1996.
- [71] J. Laufer, "The structure of turbulence in fully developed pipe flow.," National Advisory Committee for Aeronautics, Report 1174, 1952.
- [72] H. Schlichting, *Grenzschicht-Theorie*. Karlsruhe, Germany: Verlag G. Braun, 1982.
- [73] G. I. Taylor, "Diffusion by Continuous Movements," *Proc. London Math. Soc.*, vol. 20, no. 2, p. 196, 1921.
- [74] J. Boussinesq, "Calcul du pouvoir refroidissant des fluides," *J. Math.*, vol. 1, pp. 285–332, 1905.
- [75] F. J. Montes, M. A. Galan, and R. L. Cerro, "Mass transfer from oscillating bubbles in bioreactors," *Chemical Engineering Science*, vol. 54, pp. 3127-3136, 1999.
- [76] M. Martín, F. J. Montes, and M. A. Galán, "Approximate theoretical solution for the Sherwood number of oscillating bubbles at different Reynolds numbers," *Chemical Engineering and Processing*, vol. 49, pp. 245-254, 2010.
- [77] S. Hosoda, S. Abe, S. Hosokawa, and A. Tomiyama, "Mass transfer from a bubble in a vertical pipe," *International Journal of Heat and Mass Transfer*, vol. 69, pp. 215-222, 2014.
- [78] S. Hosoda, G. Tryggvason, S. Hosokawa, and A. Tomiyama, "Dissolution of Single Carbon Dioxide Bubbles in a Vertical Pipe," *Journal of Chemical Engineering of Japan*, vol. 48, no. 6, pp. 418-426, 2015.
- [79] J. Aoki, K. Hayashi, S. Hosokawa, and A. Tomiyama, "Effects of Surfactants on Mass Transfer from Single Carbon Dioxide Bubbles in Vertical Pipes," *Chem. Eng. Technol.*, vol. 38, no. 11, pp. 1955–1964, 2015.
- [80] W. J. Nock, S. Heaven, and C. J. Banks, "Mass transfer and gas-liquid interface properties of single CO<sub>2</sub> bubbles rising in tap water," *Chem. Eng. Science*, vol. 140, pp. 171-178, 2016.

- [81] P. Kováts, D. Thévenin, and K. Zähringer, "Investigation of Mass Transfer and Hydrodynamics in a Model Bubble Column," *Chemical Engineering Technology*, vol. 40, pp. 1434–1444, 2017.
- [82] P. Kováts, D. Thévenin, and K. Zähringer, "Characterizing fluid dynamics in a bubble column aimed for the determination of reactive mass transfer," *Heat Mass Transfer*, vol. 54, pp. 453-461, 2018.
- [83] R. Kipping, H. Kryk, E. Schleicher, M. Gustke, and U. Hampel, "Application of a Wire-Mesh Sensor for the Study of Chemical Species Conversion in a Bubble Column," *Chemical & Engineering Technology*, vol. 40, pp. 1425-1433, 2017.
- [84] D. Darmana, R. L.B. Henket, N. G. Deen, and J. A. M. Kuipers, "Detailed modelling of hydrodynamics, mass transfer and chemical reactions in a bubble column using a discrete bubble model: Chemisorption of CO<sub>2</sub> into NaOH solution, numerical and experimental study," *Chem. Eng. Sci.*, vol. 62, no. 9, pp. 2556-2575, 2007.
- [85] D. Zhang, N. G. Deen, and J. A. M. Kuipers, "Numerical Simulation of the Dynamic Flow Behavior in a Bubble Column: A Study of Closures for Turbulence and Interface Forces," *Chemical Engineering Science*, vol. 61, pp. 7593–7608, 2006.
- [86] M Krauß and R. Rzehak, "Reactive absorption of CO<sub>2</sub> in NaOH: Detailed study of enhancement factor models," *Chem. Eng. Sci.*, vol. 166, pp. 193-209, 2017.
- [87] J. A. Tsamopoulos and R. A. Brown, "Nonlinear oscillation of inviscid drops and bubbles," *Journal of Fluid Mechanics*, vol. 27, pp. 519-537, 1983.
- [88] R. B. Bird, W. E. Stewart, and E. N. Lightfoot, *Transport Phenomena*, 2nd ed. New York: J. Wiley, 2007.
- [89] H. Brauer, "Particle/fluid transport processes," *Progress Chemical Engineering*, vol. 19, pp. 81-111, 1981.
- [90] A. C. Lochiel and P. H. Calderbank, "Mass transfer in the continuous phase around axisymmetric bodies of revolution," *Chemical Engineering Science*, vol. 19, pp. 471-484, 1964.
- [91] R. Sander, "Compilation of Henry's law constants (version 4.0) for water as solvent," *Atmospheric Chemistry and Physics*, vol. 15, pp. 4399-4981, 2015.
- [92] E. L. Cussler, *Diffusion: Mass Transfer in Fluid Systems*, 2nd ed. New York: Cambridge University Press, 2007.
- [93] G. F. Versteeg and W. P. M. van Swaaij, "Solubility and diffusivity of acid gases (carbon dioxide, nitrous dioxide) in aqueous alkanolamine solutions," *Journal of Chemical Engineering Data*, vol. 33, no. 1, pp. 29-34, 1988.
- [94] W. -D. Deckwer, I. Adler, and A. Zaidi, "A comprehensive study on co<sub>2</sub>-interphase mass transfer in vertical cocurrent and countercurrent gas-liquid flow," *The Canadian Journal of Chemical Engineering*, vol. 56, no. 1, pp. 43-55, 1978.
- [95] N. Frössling, "Gerlands Beiträge zur Geophysik," vol. 52, pp. 170–216, 1938.
- [96] R. Rzehak and E. Krepper, "Euler-Euler simulation of mass-transfer in bubbly flows," *Chemical Engineering Science*, vol. 155, pp. 459–468, 2016.







# List of presentations and publications

The following list consists of all presentations and publications made during the doctoral period. Regarding the presentations, the underlining marks the author who presented the work.

MUNIZ, M.; SOMMERFELD, M.. *Modelling of bubble dynamics in the frame of Euler/Lagrange calculations of bubble columns*. ProcessNET Jahrestreffen, Bingen – Germany, 29.02 – 02.03.2016, (Abstract - oral presentation), 2016.

MUNIZ, M.; SOMMERFELD, M.. *Modelling of bubble dynamics and Euler/Lagrange predictions of bubble columns*. ICMF 2016 – International Conference on Multiphase Flow, Florence – Italy, 22.05 – 27.05.2016, (Abstract - oral presentation), 2016.

MUNIZ, M.; SOMMERFELD, M.. *Importance of modelling bubble dynamics for calculations of bubble columns: LES combined with Lagrangian tracking*. Enabling Process Innovation through Computation in Chemical, Oil/Gas, Petroleum & Bio-Process Industries, BIRS University-Industry Workshop, Banff, Alberta, Canada, 7. – 12. August, 2016, (invited lecture), 2016.

MUNIZ, M.; SOMMERFELD, M. . *On the Bubble Dynamics in the Frame of Euler/Lagrange Predictions of Bubble Columns*. ProcessNET Jahrestreffen, Dresden – Germany, 14.03 – 17.03.2017, (Abstract - oral presentation), 2017.

SOMMERFELD, M.; MUNIZ, M.. *On the Importance of Modelling Bubble Dynamics for Numerical Calculations of Bubble Columns*. 3rd International Symposium on Multiscale Multiphase Process Engineering (MMPE), Toyama – Japan, 08.05 – 11.05.2018. (Abstract - Keynote Lecture) 2017.

MUNIZ, M.; SOMMERFELD, M.. *Effects Of Bubble Dynamics And Force Formulations On Bubble Column Predictions With The Euler/Lagrange Approach*. Desenzano del Garda – Italy, 13.09 – 15.09.2017. 14th International Conference On Multiphase Flow In Industrial Plant, (Conference Paper – oral presentation) 2017.

MUNIZ, M.; SOMMERFELD, M.. *Modelling Of Elementary Processes By Euler/Lagrange Simulations Of Bubble Columns*. Annual Meeting 2017 DFG SPP-1740 – Reaktive Blasenströmungen, Darmstadt – Germany, 27.09 – 28.09.2017., (Oral presentation) 2017.

MUNIZ, M.; TABORDA, M. A.; SOMMERFELD, M.. *Euler/Lagrange predictions of rising bubbles considering mass transfer*. ProcessNET Jahrestreffen, Bremen – Germany, 06.03 – 09.03.2018, (Abstract - oral presentation), 2018.

MUNIZ, M.; TABORDA, M. A.; SOMMERFELD, M.. *Mass transfer modeling of bubble swarms with Euler/Lagrange approach*. Annual Meeting 2018 DFG SPP-1740 – Reaktive Blasenströmungen, Hamburg-Harburg – Germany, 20.06 – 22.06.2018., (Oral presentation) 2018.

MUNIZ, M.; TABORDA, M. A.; SOMMERFELD, M.. *LES-Euler/Lagrange Modelling of Bubbly Flows Considering Effects of Bubble Dynamics on Mass Transfer*. International Symposium - Power and Chemical Engineering, Sofia – Bulgaria, 29.06 – 02.07.2018. (Abstract - Oral presentation) 2018.

SOMMERFELD, M.; MUNIZ, M.; SCHMALFUß, S.. *The Importance of Fluid Forces Acting on Particle and Bubbles for the Performance of Multiphase Processes*. International Symposium - Power and Chemical Engineering, Sofia – Bulgaria, 29.06 – 02.07.2018. (Plenary Lecture) 2018.

SOMMERFELD, M.; MUNIZ, M.; REICHARDT, T.. *On the Importance of Modelling Bubble Dynamics for Point-mass Numerical Calculations of Bubble Columns*. Journal Of Chemical Engineering Of Japan, v. 51, p. 301-317, 2018. [dx.doi.org/10.1252/jcej.17we277](https://doi.org/10.1252/jcej.17we277) (Conference paper).

TABORDA, M. A.; MUNIZ, M.; SOMMERFELD, M.. *Reactive LES-Euler/Lagrange modelling of bubble columns considering effects of bubble dynamics*. ProcessNET Jahrestreffen, Frankfurt – Germany, 18.03 – 20.03.2019, (Abstract - oral presentation), 2019.